UNIVERSITY OF OKLAHOMA

GRADUATE COLLEGE

MULTISCALE CHARACTERIZATION OF URBAN AIR QUALITY FROM OBSERVATIONS AND INTEGRATED DATASETS

A THESIS

SUBMITTED TO THE GRADUATE FACULTY

in partial fulfillment of the requirements for the

Degree of

MASTER OF SCIENCE

By JESSICA LEFFEL

Norman, Oklahoma

2026

Downloaded from SHAREOK. Persistent Handle URL: https://hdl.handle.net/11244/342789

MULTISCALE CHARACTERIZATION OF URBAN AIR QUALITY FROM OBSERVATIONS AND INTEGRATED DATASETS

A THESIS APPROVED FOR THE

SCHOOL OF METEOROLOGY

BY THE COMMITTEE CONSISTING OF

Dr. Chenghao Wang, Chair

Dr. Xiao-Ming Hu

Dr. Marcela Loría-Salazar

©Copyright by JESSICA LEFFEL 2026

All Rights Reserved.

Acknowledgements

To begin, I would like to extend my deepest gratitude to my advisor, Dr. Chenghao Wang, for his constant support, guidance, and mentorship throughout the past two years. From data processing and analysis to manuscript writing and conference presentations, he has helped me grow as a researcher and I feel incredibly fortunate to have such a dedicated advisor. Our weekly meetings have been invaluable, and he always makes time to answer my questions and work through challenges no matter how busy his schedule is. Beyond the day-to-day research, Dr. Wang has opened many doors for me, including the opportunity to present chapter 2 of this thesis at a research conference and connecting me with collaborators that made chapter 3 possible. I also want to thank my committee members, Dr. Xiao-Ming Hu and Dr. Marcela Loría-Salazar, for generously agreeing to support this thesis and offering their time and expertise. I am grateful to have their feedback and perspectives to strengthen this thesis.

Chapter 3 would not have been possible without the support from the Peru air quality project and the help of several people. Dr. Hu's expertise was especially valuable for the WRF-Chem simulations and mobile methane measurements. In addition, Sandra Olinda Pfoccoalata Montañez and Andrea María Fernanda Salas Yaulli, visiting students from the Universidad Nacional de San Agustín de Arequipa, assisted with collecting methane measurements around the Oklahoma City landfill site and I appreciated their help and good company in the field. I also want to thank Tia Scarpelli and Joseph Heckler at Carbon Mapper for coordinating the Tanager-1 overpass of the landfill site and generously sharing their data with us. Their willingness to collaborate made the satellite component of this work possible.

I am deeply grateful to the faculty and staff of the School of Meteorology for creating such a supportive environment to learn and grow in. The quality of the curriculum and the dedication of the professors here have shaped the way I think about atmospheric science, and I feel well prepared to continue working at the PhD level because of the foundation the master's program gave me. I am also especially thankful to Danika Hines-Barnett, for her consistent guidance and for always being approachable and willing to answer any questions.

Finally, I want to thank my family and friends. To my parents in particular, thank you for always encouraging me and supporting my decision to go to graduate school. To my friends near and far, thank you for keeping me grounded and reminding me to enjoy the journey. Your support has meant more than I can put into words.

This work was supported by the National Aeronautics and Space Administration (NASA) under grant Nos. 80NSSC24K1056 (Early Career Investigator Program in Earth Science) and 80NSSC24K0357, the U.S. National Science Foundation (NSF) under grant No. OIA-2327435, grant No. 20163646499 from the Universidad Nacional de San Agustín de Arequipa (UNSA) of Peru through the Global Change and Human Health Institute, and the National Oceanic and Atmospheric Administration (NOAA) under grant No. NA21OAR4590361.

Table of Contents

Acknowledgments **iv**

Table of Contents **vi**

List of Figures **viii**

Abstract **xiii**

1. Introduction 1

1.1 Urban compound heat and $PM_{2.5}$ pollution..... 1

1.2 Urban methane emissions: observations, processes, and modeling challenges. 6

1.3 Thesis scope and structure 9

2. Data-driven analysis of urban compound heat and $PM_{2.5}$ pollution episodes..... 11

2.1 Methodology 11

2.2 Characteristics of heat waves based on minimum air temperatures 19

2.3 Characteristics of $PM_{2.5}$ pollution episodes 22

2.4 Characteristics of compound heat and $PM_{2.5}$ pollution episodes..... 26

2.5 Comparison and attribution of single and compound extremes..... 30

2.6 Post-2016 reversal in $PM_{2.5}$ and its impact on compound events..... 33

2.7 Limitations and uncertainties..... 36

3. Integrated observational and modeling analysis of urban methane emissions: A landfill case study 38

3.1 Methodology 38

3.2 Mobile measurements of methane plumes..... 46

3.3 Satellite observations of methane emissions..... 53

3.4 Simulated methane enhancements 55

3.5 Integrating observations and simulations for methane emission estimation 59

4. Conclusions 62

4.1 Key findings on urban compound heat and $PM_{2.5}$ pollution episodes 62

4.2 Key findings on urban methane emissions and observational constraints 63

4.3 Implications and future work 64

References **67**

Appendix **91**

List of Figures

2.1 Overview of the methodological workflow for detecting and analyzing heat waves, $PM_{2.5}$ pollution episodes, and compound events. 12

2.2 Comparison of warm-season (a and c) daily minimum temperature time series and (b and d) probability density functions from the ISU data in 2003–2020, Daymet data in 2003–2020, Daymet data in 1981–2002, and bias corrected (BC-ed) Daymet data in 1981–2002 for (a and b) Salt Lake City, UT, and (c and d) Auburn, AL. For clarity, the time series are smoothed based on 10-day running means, with shaded areas representing the corresponding ±1 standard deviation. 15

2.3 Frequency and duration of heat waves based on minimum temperatures in urban and surrounding rural areas: (a) frequency in urban areas, (b) frequency in rural areas, (c) relative difference in frequency between urban and rural areas (urban minus rural), (d) duration in urban areas, (e) duration in rural areas, and (f) relative difference in duration between urban and rural areas (urban minus rural). Filled circles represent individual urban and rural areas, with circle sizes scaled to urban population. White circles in (c) and (f) indicate no urban–rural differences..... 20

2.4 Cumulative intensity of heat waves based on minimum temperatures and warm-season mean minimum temperature in urban and surrounding rural areas: (a) cumulative heat intensity in urban areas, (b) cumulative heat intensity in rural areas, (c) relative difference in cumulative heat intensity between urban and rural areas (urban minus rural), (d) warm-season mean minimum temperature in urban areas, (e) warm-season mean minimum temperature in rural areas, and (f) difference in warm-season mean minimum

temperature between urban and rural areas (urban minus rural). Filled circles represent individual urban and rural areas, with circle sizes scaled to urban population..... 22
2.5 Frequency and duration of $PM_{2.5}$ pollution episodes in urban and surrounding rural areas: (a) frequency in urban areas, (b) frequency in rural areas, (c) relative difference in frequency between urban and rural areas (urban minus rural), (d) duration in urban areas, (e) duration in rural areas, and (f) relative difference in duration between urban and rural areas (urban minus rural). Filled circles represent individual urban and rural areas, with circle sizes scaled to urban population. White circles in (c) and (f) indicate no urban–rural differences. 23
2.6 Cumulative intensity of $PM_{2.5}$ pollution episodes and warm-season mean $PM_{2.5}$ concentration in urban and surrounding rural areas: (a) cumulative $PM_{2.5}$ pollution intensity in urban areas, (b) cumulative $PM_{2.5}$ pollution intensity in rural areas, (c) relative difference in cumulative $PM_{2.5}$ pollution intensity between urban and rural areas (urban minus rural), (d) warm-season mean $PM_{2.5}$ concentration in urban areas, (e) warm-season mean $PM_{2.5}$ concentration in rural areas, and (f) difference in warm-season mean $PM_{2.5}$ concentration between urban and rural areas (urban minus rural). Filled circles represent individual urban and rural areas, with circle sizes scaled to urban population 25
2.7 Frequency and duration of compound heat and $PM_{2.5}$ pollution episodes in urban and surrounding rural areas: (a) frequency in urban areas, (b) frequency in rural areas, (c) relative difference in frequency between urban and rural areas (urban minus rural), (d) duration in urban areas, (e) duration in rural areas, and (f) relative difference in duration between urban and rural areas (urban minus rural). Filled circles represent individual

urban and rural areas, with circle sizes scaled to urban population. White circles in (c) and (f) indicate no urban–rural differences..... 27

2.8 Cumulative intensity of compound heat and $PM_{2.5}$ pollution episodes in urban and surrounding rural areas: (a) cumulative heat intensity in urban areas, (b) cumulative heat intensity in rural areas, (c) relative difference in cumulative heat intensity between urban and rural areas (urban minus rural), (d) cumulative $PM_{2.5}$ pollution intensity in urban area, (e) cumulative $PM_{2.5}$ pollution intensity in rural area, and (f) relative difference in cumulative $PM_{2.5}$ pollution intensity between urban and rural areas (urban minus rural). Filled circles represent individual urban and rural areas, with circle sizes scaled to urban population 28

2.9 Annual frequency of (a) $PM_{2.5}$ pollution episodes and (b) compound events, measured as the number of event days in urban areas across the CONUS, eastern U.S. (Northeast, Upper Midwest, Ohio Valley, and Southeast), and western U.S. (Southwest, Northwest, and West). Each box shows the interquartile range (IQR), with the horizontal line indicating the median, whiskers extending to 1.5 × IQR, and points beyond the whiskers representing outliers. The inset in (b) shows the climate regions used to define the eastern and western U.S. (blue and red, respectively). 35

3.1 Satellite view of Republic Services Southeast Landfill in Oklahoma City. ... 39

3.2 Mobile measurement route around Republic Services Southeast Landfill in Oklahoma City, including (a) larger perimeter and (b) the transect along Interstate 240..... 41

3.3 Flowchart of mobile CH_4 measurement data post-processing steps and multi-source emission rate comparison for the Oklahoma City landfill..... 41

3.4 WRF-Chem nested domain configuration for Oklahoma City landfill site simulations: (a) outer domains D01 (green) and D02 (yellow), and (b) inner domains D03 (red) and D04 (blue). 44

3.5 Mobile CH_4 concentrations (ppm) recorded along the Interstate 240 transect south of the Oklahoma City landfill site during early morning measurement intervals on December 13th, 2025, including: a) 04:15, b) 04:45, c) 05:15, d) 06:45, e) 07:15, f) 07:45, g) 08:15, and h) 08:45 (CST). 46

3.6 Mobile CH_4 concentrations (ppm) recorded along the Interstate 240 transect south of the Oklahoma City landfill site during late morning to afternoon measurement intervals on December 13th, 2025, including: (a) 09:15, (b) 09:45, (c) 10:15, (d) 12:45, (e) 13:15, (f) 13:45, (g) 14:15, and (h) 14:45 (CST). 48

3.7 Time series of near-surface CH_4 concentrations (ppb) from mobile measurements around the Oklahoma City landfill site on December 13th, 2025, derived from LI-COR 7810 and GPS data in local time (CST)..... 49

3.8 Distribution of (b) mobile CH_4 concentrations (ppb) and (a) WRF-Chem simulated mean surface winds (where half-barb = 2.5 m s^{-1}, full = 5 m s^{-1}, flag = 25 m s^{-1}) at the Oklahoma City landfill site during active 30-minute measurement intervals on December 13th, 2025 51

3.9 Probability density distribution of near-surface CH_4 concentrations (ppb) from mobile measurements on December 13th, 2025, at the Oklahoma City landfill site..... 52

3.10 Tanager-1 satellite-retrieved column CH_4 enhancement (ppm·m) over the Oklahoma City landfill site during the Carbon Mapper overpass at 18:10:12 UTC on December 13th,

2025. This includes the visualization plume (blue-purple shading) and Integrated Mass Enhancement plume mask (yellow-purple shading)..... 54

3.11 WRF-Chem simulated (a) surface temperature (°C), (b) surface wind speed and direction (m s^{-1}), and (c) CH_4 enhancement (ppmv) at 19:00 UTC around the Oklahoma City landfill site on December 13th, 2025..... 55

3.12 Observed vs simulated CH_4 enhancement (ppb) at 19:00 UTC around the Oklahoma City landfill site on December 13th, 2025..... 56

3.13 Observation to simulation scaling of WRF-Chem near-surface CH_4 concentration (ppmv) with surface wind vectors at 19:00 UTC around the Oklahoma City landfill site on December 13th, 2025..... 58

3.14 Spatial distribution of CH_4 enhancements around the Oklahoma City landfill site on December 13th, 2025, as captured by (a) LI-COR 7810 mobile measurements from 19:04–19:06 UTC, (b) Tanager-1 satellite overpass at 18:10:12 UTC, and (c) WRF-Chem model simulation at 19:00:00 UTC..... 59

Abstract

Urban air quality is shaped by processes operating across multiple spatial scales, from regional interactions that govern population exposure to local emission sources within cities. This thesis investigates these multiscale dynamics through two complementary analyses that together highlight the need for integrated, high-resolution approaches. The first study examines compound heat wave and $PM_{2.5}$ pollution events across urban and surrounding rural areas in the contiguous United States over a 23-year period (2000–2022) using reconstructed high-resolution datasets. Results show that urban areas systematically experience more frequent, prolonged, and intense events than their rural surroundings, with approximately 98% of cities exhibiting stronger co-occurrence. Spatial patterns of compound events closely resembled those of $PM_{2.5}$ pollution episodes, suggesting that air pollution plays a dominant role in driving compound extremes, while recent increases in the western U.S. are linked to wildfire emissions. The second study focuses on within-city methane (CH_4) emissions, using a major landfill site in Oklahoma City as a case study to integrate mobile measurements, satellite observations, and WRF-Chem simulations. Near-surface CH_4 concentrations showed a strong morning-to-afternoon variability driven by boundary layer evolution, with early-morning peaks exceeding 30,000 ppb that declined substantially by the afternoon hours. WRF-Chem demonstrated the spatial structure of the CH_4 plume well, and the ratio of observed to simulated enhancements was used to inversely estimate the landfill emission rate, yielding a mobile-derived estimate consistent with the satellite observation to within roughly 7% (996.92 and 928.07 kg CH_4 hr^{-1} respectively). These results demonstrate that urban air quality cannot be fully understood without resolving both regional-scale environmental stressors and fine-scale emission and transport processes. This work underscores the importance of integrating ground-based measurements, satellite

observations, and process-based modeling to achieve a consistent, multiscale characterization of urban air quality, with implications for improving emission quantification and informing mitigation strategies in cities.

Chapter 1

Introduction

Air quality is a fundamental determinant of environmental and public health conditions globally. Degraded air quality, driven by both conventional air pollutants and greenhouse gases, poses serious risks to ecosystems, human health, and climate stability (Erickson, 2017; Filonchyk et al., 2024; West et al., 2013). Among the most consequential are fine particulate matter ($PM_{2.5}$) and methane (CH_4), which operate across different spatial and temporal scales. Prolonged exposure to poor air quality is associated with a wide range of adverse outcomes, including respiratory and cardiovascular disease, premature mortality, and reduced ecosystem and agricultural productivity (Duan et al., 2017; Fang et al., 2013; West et al., 2006). Although conventional air pollutants and greenhouse gases are often treated separately under policy frameworks and regulations, they are influenced by common emission sources, meteorological conditions, and physical and chemical interactions that can amplify their combined impacts (Mar et al., 2022; West et al., 2013). Understanding air quality, particularly in urban environments, therefore requires an integrated, multiscale perspective that accounts for both regional pollution dynamics and localized emission processes under a changing climate (Fang et al., 2013; Filonchyk et al., 2024).

1.1 Urban compound heat and $PM_{2.5}$ pollution

Urbanization has profound impacts on local climate and air quality, often exacerbating warm-season heat stress and air pollution in cities. The expansion and intensification of impervious surfaces, reduced vegetation, and increased anthropogenic heat emissions amplify the

urban heat island (UHI) effect, with elevated urban temperatures and reduced nocturnal cooling compared to rural surroundings (Oke et al., 2017; Phelan et al., 2015). Meanwhile, urbanization drives the emissions of air pollutants from various anthropogenic activities such as energy production, transportation, household combustion, and solid waste disposal, leading to deteriorated air quality and elevated greenhouse gas concentrations (He et al., 2002; Sicard et al., 2023). These environmental stressors not only strain urban ecosystems but also negatively impact urban populations, particularly during extreme weather events (Analitis et al., 2014; J. Liu et al., 2022). Understanding the characteristics of these risk factors is a critical step toward achieving the United Nations Sustainable Development Goals for sustainable cities, climate action, and improved public health conditions (United Nations, 2015).

Previous studies have suggested that heat waves can modify urban heat stress. Specifically, the intensity of the canopy UHI effect, defined as the difference between urban and rural near-surface air temperature, often amplifies during heat waves, as evidenced by observational and modeling studies (Chen et al., 2023; Cheval et al., 2024; Jiang et al., 2019; Ramamurthy & Bou-Zeid, 2017). However, this synergistic effect varies across diurnal and seasonal cycles and depends on background geographical controls. For example, the increase in daytime UHI intensity can be higher in temperate climate zones than in dry climates, largely attributable to contrasts in water availability (L. Zhao et al., 2018). In addition, the exacerbated heat stress during heat waves has profound impacts on public health, contributing to increased heat-related mortality and morbidity (Anderson & Bell, 2011; Simpson et al., 2024; Tan et al., 2010). Prolonged exposure can lead to various heat-related illnesses, including heat stroke, heat exhaustion, and cardiovascular and respiratory conditions (Kovats & Hajat, 2008). This is especially an issue for populations that are vulnerable to extreme heat, such as children, older

people, and individuals with pre-existing medical conditions (Ebi et al., 2021). Furthermore, observational records have suggested rising trends in the frequency, duration, and intensity of heat waves in recent decades (Habeeb et al., 2015; Meehl & Tebaldi, 2004; Perkins et al., 2012). With ongoing climate change and rapid urbanization, these trends are projected to continue (Guerreiro et al., 2018; Perkins-Kirkpatrick & Gibson, 2017; L. Zhao et al., 2018). This suggests that heat waves and the UHI effect will remain a major concern for most urban areas in the future.

Fine particulate matter ($PM_{2.5}$) is defined as small particles that are less than 2.5 micrometers in diameter, and is one of the six criteria air pollutants regulated under the U.S. Clean Air Act (U.S. EPA, 2024b). It originates from a combination of primary sources (e.g., fossil fuel combustion, vehicle emissions, wildfires, and windblown mineral dust) and secondary formation through atmospheric chemical reactions (Chow et al., 2006; X.-M. Hu et al., 2008; Liang et al., 2016; McDuffie et al., 2021). The small size of $PM_{2.5}$ allows it to penetrate deep into the respiratory system and enter the bloodstream (Feng et al., 2016; Ma et al., 2024). Exposure to $PM_{2.5}$ is associated with a wide range of adverse health outcomes, such as respiratory infections, cardiovascular diseases, premature deaths, and other chronic conditions (Bell et al., 2007; Han et al., 2024). In 2017 alone, 3.8 million deaths globally were attributed to annual $PM_{2.5}$ exposure, and ischemic heart disease and stroke were identified as leading causes (McDuffie et al., 2021). The impact of urban areas on $PM_{2.5}$ concentrations varies regionally. For example, a recent global long-term study found strong correlations between urbanization and $PM_{2.5}$ concentrations in India and sub-Saharan Africa, but decoupled relationships in Europe and the U.S. where emissions have been successfully reduced by regulatory efforts (Lim et al., 2020). However,

frequent $PM_{2.5}$ exceedance events continue to occur, even in countries with stringent regulations (Colmer et al., 2020; Xie et al., 2020).

The simultaneous occurrence of heat waves and high air pollution levels that exceed air quality standards is commonly referred to as compound events or episodes (Zscheischler et al., 2020). These events are influenced by the potential interactions between heat and air quality, with each exacerbating the other (Zscheischler et al., 2018). During heat waves, increased energy consumption, particularly from air conditioning use, drives higher emissions of $PM_{2.5}$ and its precursors from power generation and other sources (S. Liu et al., 2024). Meanwhile, elevated temperature during heat waves can enhance the formation of $PM_{2.5}$ precursors by accelerating photochemical reactions and increasing biogenic emissions (X.-M. Hu et al., 2024). In addition, stagnant atmospheric conditions often associated with heat waves favor the accumulation of $PM_{2.5}$, further deteriorating urban air quality (Park et al., 2023; L. Wang et al., 2022). These compound events usually intensify public health risks beyond those associated with either stressor alone (Deng et al., 2024; Feron et al., 2023; Ji et al., 2020). For instance, a five-year study in Jiangsu Province, China demonstrated synergistic interactions between $PM_{2.5}$ pollution and extreme heat which resulted in increased total and cause-specific mortalities, especially from respiratory diseases (L. Zhou et al., 2023). Similarly, another study focusing on older adults in New England, U.S. revealed that hot days can amplify the short-term effect of $PM_{2.5}$ pollution, leading to increasing respiratory and cardiac hospital admissions (Yitshak-Sade et al., 2018). Developing appropriate mitigation strategies in urban areas requires a comprehensive characterization of these compound events as a critical first step.

Despite growing research on heat waves, $PM_{2.5}$ pollution, and their combined effects, several key challenges persist in understanding the dynamics of compound heat and $PM_{2.5}$

pollution events. Regional- and global-scale studies based on observations and/or models often rely on spatial and/or temporal resolutions that are too coarse to distinguish the unique dynamics of urban and rural environments (Lim et al., 2020; Perkins-Kirkpatrick & Gibson, 2017; Smith et al., 2013; D. Yang et al., 2018). In comparison, long-term, high-resolution studies focusing on urban–rural contrasts typically use either point-scale station observations or remotely sensed data products. While station data directly reflect near-surface conditions, they fail to capture the spatially heterogeneous temperature and pollutant distributions within cities (e.g., X.-M. Hu & Xue, 2016; J. Yang & Bou-Zeid, 2019). Remotely sensed land surface temperature (LST) is widely used in urban climate research but differs fundamentally from near-surface air temperature, which is a more direct and relevant indicator of population heat exposure and building energy use (e.g., Naserikia et al., 2023). Similarly, remotely sensed aerosol optical depth (AOD) products are commonly used as proxies for $PM_{2.5}$ and other pollutants. However, AOD represents columnar aerosol loads rather than near-surface concentrations, which can introduce substantial uncertainties in estimating pollutant-specific dynamics (Guo et al., 2017; C. Wang et al., 2017). High-resolution modeling studies provide a promising alternative for resolving urban- and sub-urban-scale processes but are frequently limited to short time periods or single-city domains. This limits their ability to reveal the climatological patterns of compound events across multiple cities. To date, no research has systematically examined compound heat and air pollution (including $PM_{2.5}$) episodes across all urban areas in the contiguous U.S. (CONUS), leaving a critical gap in understanding their spatial and temporal variability and associated event characteristics.

1.2 Urban methane emissions: observations, processes, and modeling challenges

Methane (CH_4) is the second most abundant anthropogenic greenhouse gas in the atmosphere after carbon dioxide, and it is responsible for approximately 20% of the warming from long-lived greenhouse gases since pre-industrial times (Kirschke et al., 2013). According to the Sixth Assessment Report of the Intergovernmental Panel on Climate Change (IPCC), CH_4 had been assessed to have 27 times the global warming potential (GWP) of carbon dioxide over a 100-year time horizon (IPCC, 2023). Its atmospheric concentration has risen dramatically over the past two centuries, driven largely by the increase of anthropogenic emission sources (Karakurt et al., 2012; Kirschke et al., 2013; H. Zhao et al., 2019). These sources span across multiple sectors, including agriculture, fossil fuel extraction, and waste management (Heilig, 1994; Jackson et al., 2026; Karakurt et al., 2012; Saunois et al., 2025; Yusuf et al., 2012). Landfills in particular represent one of the largest anthropogenic CH_4 sources globally, as the anaerobic decomposition of organic waste in municipal solid waste (MSW) facilities continuously generates and emits CH_4 to the atmosphere (Themelis & Ulloa, 2007; Tong et al., 2025; Y. Wang et al., 2024). In the U.S., MSW landfills were the third-largest source (accounting for approximately 14.4%) of the total anthropogenic CH_4 emissions in 2022 (U.S. EPA, 2024a). Beyond its climate impacts, CH_4 also acts as a precursor to tropospheric ozone, linking greenhouse gas emissions directly to surface air quality degradation and associated health impacts (Mar et al., 2022; West et al., 2006). These combined climate and air quality consequences highlight the importance of accurately quantifying CH_4 emissions to inform mitigation strategies.

CH_4 emissions can be quantified using a range of observational approaches with varying spatial and temporal coverage. Ground-based and mobile in situ measurements provide high-

precision, near-surface CH_4 concentrations and can resolve emission hotspots and fine-scale variability near sources such as landfills (Kumar et al., 2024; Mønster et al., 2019; Mosher et al., 1999). These methods include techniques such as static flux chambers, eddy covariance tower measurements, and vehicle-based transect observations, and are increasingly used to measure landfill CH_4 concentrations and identify spatial variability (McBain et al., 2005; Mønster et al., 2019). Airborne observations, such as those from imaging spectrometers, cover larger areas and can estimate emissions for an entire site. Airborne measurement studies have revealed that landfill emissions can vary substantially depending on factors like cover type, gas collection systems, and operational practices (Cambaliza et al., 2017; Cusworth et al., 2024). At a broader scale, satellite observations (satellite remote sensing; such as the Greenhouse Gases Observing Satellite (GOSAT) and the Tropospheric Monitoring Instrument (TROPOMI)) provide continuous, long-term regional to global coverage of atmospheric CH_4 column retrievals and can detect large point sources (Jacob et al., 2016, 2022; Palmer et al., 2021; X. Wang et al., 2026). Additionally, the high-resolution airborne and satellite imaging spectrometers have revealed that current CH_4 inventory estimates frequently underestimate actual emissions at many sites (Cusworth et al., 2024; Scarpelli et al., 2024; Tong et al., 2025; Y. Wang et al., 2024; Whiting et al., 2026). These approaches highlight the importance of combining measurement strategies across different scales to better understand and characterize CH_4 emissions, especially in cities where multiple sources can co-locate.

CH_4 observations alone are often insufficient to attribute concentrations to specific emission sources or quantify their relative contributions, which is where process-based modeling becomes necessary. Atmospheric CH_4 can be simulated using global chemistry–climate and transport models (e.g., GEOS-Chem and Tracer Model 5 or TM5) to capture large-scale budgets

and intercontinental transport (Buchwitz et al., 2005; Patra et al., 2011), while regional to urban dynamics are represented with mesoscale models such as the Weather Research and Forecasting model coupled with Chemistry (WRF-Chem) and Community Multiscale Air Quality Modeling System (CMAQ) (Hong et al., 2017). The latter can also be integrated with Lagrangian particle dispersion models (e.g., STILT and HYSPLIT) to enable high-resolution source attribution and inverse estimation of emissions (L. Hu et al., 2025; Z. Zhou et al., 2026). In particular, WRF-Chem and its greenhouse gas configurations WRF-GHG have increasingly been used to simulate CH_4 concentrations, interpret ground-based and remotely sensed observations, and evaluate emission inventories (Callewaert et al., 2025; X.-M. Hu et al., 2025). WRF-GHG has also been used to track emissions from different source sectors and identify the dominant contributors to CH_4 variability across different regions and seasons (Callewaert et al., 2023; Mathew et al., 2026). However, the accuracy of these process-based models depends on the quality of input data, such as emission inventories and meteorological conditions. Any biases and uncertainties in these inputs can propagate into regional or seasonal errors in simulated CH_4, so the simulated results must be evaluated using observations (Callewaert et al., 2025).

Despite growing interest in measuring CH_4 emissions from the waste sector, significant gaps remain in accurately characterizing and attributing these emissions. Emission inventories based on bottom-up modeling approaches frequently underestimate actual landfill CH_4 emissions and enhancements, due to inconsistencies in emission accounting methods and limited representation of site-specific conditions (Saunois et al., 2020; Tong et al., 2025; Y. Wang et al., 2024). For example, a TROPOMI-based analysis of 70 U.S. landfills found that actual emissions were on median 77% higher than estimates from EPA's Greenhouse Gas Reporting Program (Nesser et al., 2024). While individual measurement studies have improved our understanding,

most rely on a single method, such as ground-based measurements, mobile surveys, or satellite observations, each with its own limitations in spatial coverage, timing, or sensitivity (Mønster et al., 2019). For example, mobile measurements can have difficulty detecting small CH_4 enhancements under changing weather conditions, while satellites cover large areas but cannot resolve fine-scale variations near individual sources (X.-M. Hu et al., 2025; Jacob et al., 2022). Studies that combine mobile and satellite observations with high-resolution modeling for landfill emissions remain rare, leaving uncertainty in how surface emissions relate to atmospheric measurements and how well models capture small-scale CH_4 patterns. Addressing this gap requires coordinated, multiscale approaches that link surface emissions to atmospheric concentrations.

1.3 Thesis scope and structure

This thesis examines urban air quality from two complementary perspectives that together illustrate the multiscale nature of the problem. Chapter 2 presents a 23-year analysis of compound heat and $PM_{2.5}$ pollution events across urban and rural areas in the CONUS, characterizing their frequency, duration, and intensity. This work has been published in Leffel et al. (2025). Chapter 3 focuses on within-city CH_4 emissions using a landfill site in Oklahoma City as a case study. It integrates concurrent mobile and satellite CH_4 observations and WRF-Chem simulations to inversely estimate landfill CH_4 emission rates and examine the influence of boundary layer processes on CH_4 variability. Chapter 4 summarizes the key findings and discusses their implications for improving the multiscale characterization of urban air quality. Together, these chapters demonstrate the importance of integrating observations and modeling

approaches across spatial scales to better understand urban air quality and inform mitigation strategies.

Chapter 2

Data-driven analysis of urban compound heat and $PM_{2.5}$ pollution episodes

This chapter provides a 23-year (2000–2022), comprehensive analysis of heat waves, $PM_{2.5}$ pollution episodes, and their co-occurrences across urban and corresponding rural areas in the CONUS. Leveraging reconstructed long-term, high-resolution datasets of daily air temperature and $PM_{2.5}$ concentrations, we investigate the frequency, duration, and cumulative intensity of these events, with a particular focus on the contrasts between urban and surrounding rural environments. Daily minimum near-surface air temperature is used to define heat waves, given its strong connections to nighttime heat stress, pollutant accumulation in a shallower nocturnal atmospheric boundary layer, and nighttime pollutant exposure induced by natural ventilation for homes without air conditioning. This study aims to advance understanding of these compound events at the city level, inform urban planning and public health strategies, and eventually guide future modeling efforts to explain their underlying mechanisms and assess mitigation efforts.

2.1 Methodology

2.1.1 Definition of urban and rural areas

The geographical boundaries of 481 CONUS urban areas in this study follow the definition of the U.S. Census Bureau (2022), each of which has a minimum population of 50,000. Following previous studies (Geng et al., 2023; Peng et al., 2012; C. Wang et al., 2025), a rural buffer zone with the same area as each urban area was established to facilitate urban–rural comparisons of event characteristics (Fig. 2.1). We then removed portions of the buffer zone that

overlap with other nearby urban areas to minimize potential urban influence within these rural areas. We further removed water bodies from all urban and rural areas to reduce their influence on air temperature and air pollutants (Clinton & Gong, 2013; Schwarz et al., 2011).

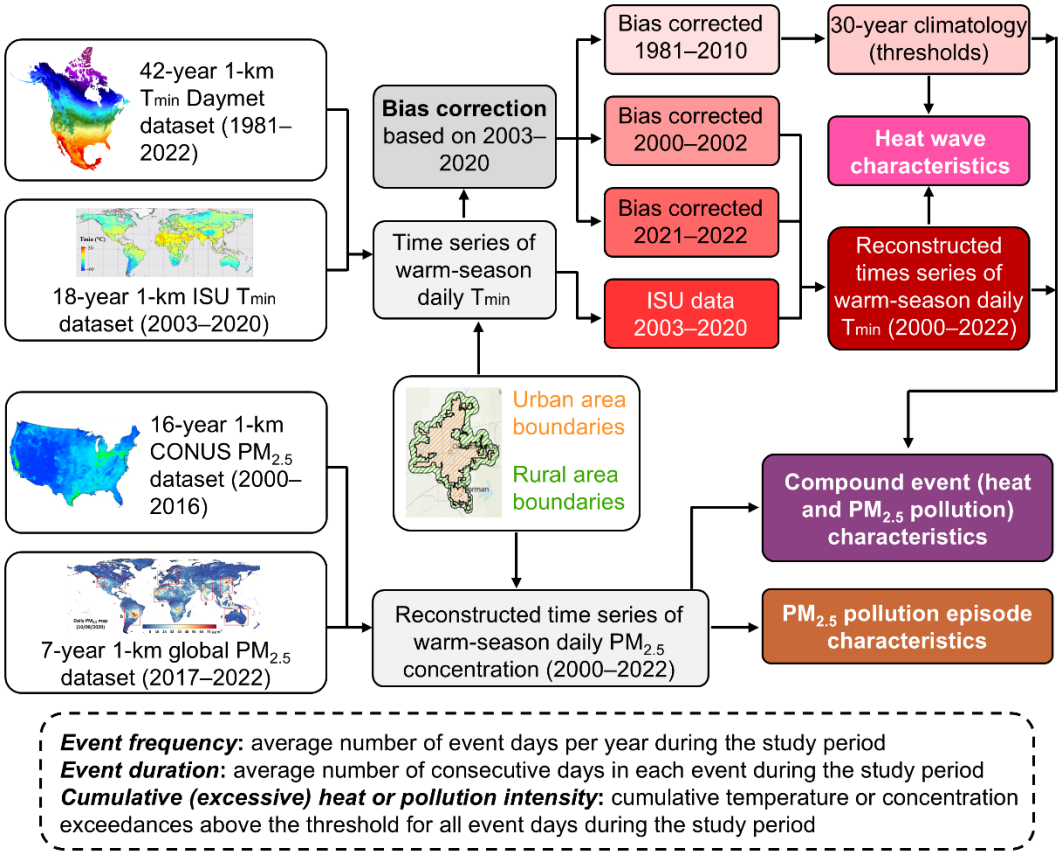


Figure 2.1. Overview of the methodological workflow for detecting and analyzing heat waves, $PM_{2.5}$ pollution episodes, and compound events.

2.1.2 Long-term high-resolution air temperature data

Investigating the long-term dynamics of heat waves in urban areas and their surrounding rural counterparts during warm seasons necessitates a reliable, high-resolution (both spatially and temporally) near-surface air temperature dataset. However, most existing long-term air temperature datasets either fail to adequately reproduce urban climate signals or cover periods

too short to establish the temperature thresholds required for identifying heat waves. To address this limitation, we reconstructed a long-term, high-resolution air temperature dataset based on two existing datasets (Fig. 2.1).

The first dataset is an 18-year (2003–2020), 1-km daily global air temperature dataset developed by Iowa State University (hereafter ISU dataset) (Zhang et al., 2022). The ISU dataset was generated using a combination of station-based daily maximum and minimum air temperature observations, remotely sensed land surface temperature data from Moderate Resolution Imaging Spectroradiometer (MODIS) products, and elevation data using the Spatially Varying Coefficient Models with Sign Preservation (SVCM-SP) algorithm. This dataset has been extensively evaluated against ground-based observations through a 10-fold cross-validation, showing a high degree of accuracy with mean absolute errors (MAEs) for daily maximum and minimum temperatures generally below 2°C across diverse environments. Specifically, the MAEs for daily maximum and minimum air temperatures over urban areas on average are 1.58°C and 1.41°C, respectively, which are substantially lower compared to those over other land cover types (Zhang et al., 2022). We extracted the time series of daily minimum temperature for each urban and rural area from 2003 to 2020.

We also used the Daymet version 4 dataset, a long-term (1980–present), 1-km daily surface weather dataset covering North America, Hawaii, and Puerto Rico (Thornton et al., 2021). The Daymet dataset provides daily maximum and minimum temperatures as well as precipitation spatially and temporally interpolated using daily weather station observations from the Global Historical Climate Network daily (GHCNd) database. It also provides secondary variables, including daylight average shortwave radiation, water vapor pressure, day length, and snow water equivalent for the snowpack, which were estimated based on geographical location,

time of year, and empirical relationships. The accuracy of Daymet has been improved through time-of-observation and high-elevation temperature sensor bias corrections. Cross-validation analyses suggest that the mean MAE for daily minimum temperature over a 40-year period (1980–2019) is 1.78°C for Daymet version 4 dataset, comparable to that for version 3 dataset (Thornton et al., 2021). In contrast, the mean MAE for daily maximum temperature during the same period is 1.52°C for version 4, marking a major improvement over the 1.75°C observed for version 3. Similarly, we extracted the time series of daily minimum temperatures averaged for each urban and rural area from 1981 to 2022. This 42-year period serves two purposes: filling the data gaps from 2000 to 2002 in the ISU dataset and establishing temperature thresholds for the 30-year (1981–2010) baseline period used in subsequent heat wave identification.

However, the Daymet dataset is known for its limited representation of urban climate signals, especially the UHI effect (X. Li et al., 2018; Thompson et al., 2025). This can lead to substantial biases when comparing heat wave characteristics between urban and rural areas. To address this, we leveraged a modified quantile delta mapping approach to bias-correct the Daymet dataset following previous studies (Cannon et al., 2015; C. Wang et al., 2023, 2025). Fig. 2.2 shows the bias-corrected warm-season daily minimum air temperature time series for two example urban areas, comparing the corrected data with the original ISU and Daymet datasets for both periods. For Auburn, the Daymet dataset tends to underestimate air temperature relative to the ISU dataset during 2003–2020. This underestimation is effectively mitigated in the bias-corrected data in 1981–2002, during which the corrected values are higher than original ones. In comparison, the bias correction effectively accounts for the Daymet overestimation in Salt Lake City during 2003–2020, adjusting the temperatures to lower values for 1981–2002. We then combined the bias-corrected Daymet data for 1981–2002 and 2021–2022 with the ISU data

for 2003–2020 to reconstruct a 42-year dataset of daily minimum air temperatures for subsequent heat wave identification. As previously mentioned, daily minimum temperature is used in this study to define heat waves due to the potential accumulation of pollutants under relatively stable atmospheric conditions at night.

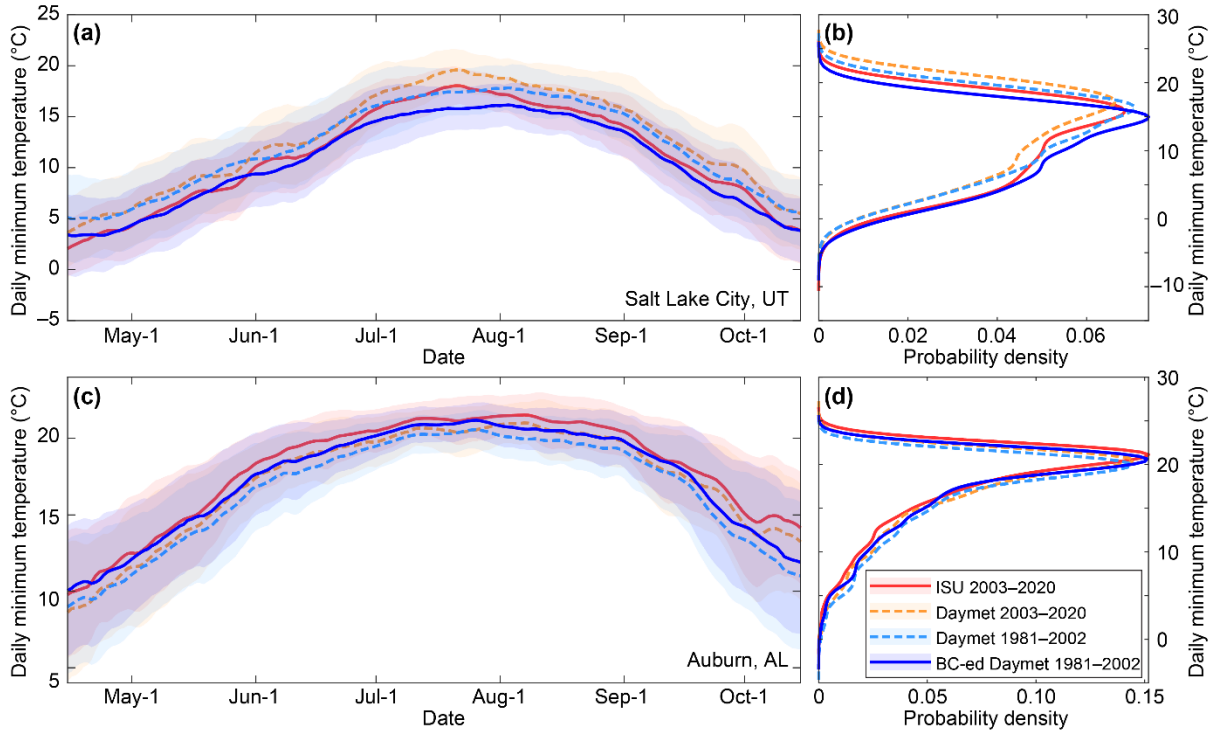


Figure 2.2. Comparison of warm-season (a and c) daily minimum temperature time series and (b and d) probability density functions from the ISU data in 2003–2020, Daymet data in 2003–2020, Daymet data in 1981–2002, and bias corrected (BC-ed) Daymet data in 1981–2002 for (a and b) Salt Lake City, UT, and (c and d) Auburn, AL. For clarity, the time series are smoothed based on 10-day running means, with shaded areas representing the corresponding ±1 standard deviation.

2.1.3 Long-term high-resolution $PM_{2.5}$ data

The long-term $PM_{2.5}$ data applied in this study were extracted from two datasets (Fig. 2.1). The first one is a 17-year (2000–2016), 1-km daily $PM_{2.5}$ dataset developed by Di et al. (2019). This dataset estimates daily mean $PM_{2.5}$ data across the CONUS using an ensemble model that integrates three machine learning algorithms, i.e., neural network, random forest, and gradient boosting. Predictor variables for this ensemble model include ground-based station monitoring data for $PM_{2.5}$, remotely sensed MODIS aerosol optical depth (AOD) data at 470 nm and 550 nm, MODIS surface reflectance, absorbing aerosol index (AAI) data from the Ozone Monitoring Instrument (OMI), aerosol-related variables from the Modern-Era Retrospective analysis for Research and Applications, Version 2 (MERRA-2), meteorological variables from the North American Regional Reanalysis (NARR) dataset, $PM_{2.5}$ predictions from global and regional chemical transport models, and various land use variables. The accuracy of this dataset has been evaluated against station monitoring data using a 10-fold cross-validation (Di et al., 2019): the overall daily and spatial R^2 values are 0.860 and 0.894, respectively, and the average root mean square error (RMSE) is 1.26 μg m^{-3} spatially.

The second dataset is a six-year (2017–2022), 1-km global daily $PM_{2.5}$ dataset developed by Wei et al. (2023). Daily estimates were made through a 4-Dimensional Space-Time Extra-Trees (4D-STET) model, which can better describe autocorrelations and differences in spatial distribution and temporal series of air pollution compared to traditional approaches. Main predictors of this model are satellite gap-filled AOD retrievals at 550 nm, hourly $PM_{2.5}$ simulations from the GEOS Composition Forecast (GEOS-CF) system, and global $PM_{2.5}$ precursors (ammonia, NO_x, SO_2, and volatile organic compounds) from the Copernicus Atmosphere Monitoring Service (CAMS) emission inventory. Auxiliary input data include ERA5-based meteorological data, 1-km population, monthly 500-m nighttime lights, monthly 1-

km normalized difference vegetation index, and surface elevation. The sample-based 10-fold cross-validation for daily retrievals suggests a robust overall accuracy, with an R^2 of 0.91 and an RMSE of 9.2 μg m^{-3}. North America shows one of the best performances among all continents, with an R^2 of 0.76 and an RMSE of 4.62 μg m^{-3}. We then extracted the time series of daily mean $PM_{2.5}$ concentrations averaged over each urban and rural area from both datasets and merged them into a continuous 23-year dataset.

2.1.4 Definitions and characteristics of events

Various definitions of heat waves have been proposed in the literature, with the temperature percentile-based thresholds being among the most commonly used criteria for their identification (Barriopedro et al., 2023; Perkins & Alexander, 2013). In this study, we define a heat wave as a period of three or more consecutive days during the warm season (May–September) when the daily minimum air temperature, averaged across the entire urban or rural area, exceeds the 90th percentile of the 30-year daily climatology (Anderson & Bell, 2011; C. Wang, Wang, & Li, 2020; C. Wang, Wang, & Sun, 2020). The 90th percentile for a given day was calculated based on all daily temperature data within a 15-day moving window centered on that day during 1981–2010 (X. Yang et al., 2024). For each urban–rural pair, we used the threshold derived from rural temperature records for both areas. For consistency, we selected the overlapping period from 2000 to 2022 between the reconstructed 42-year air temperature dataset and 23-year $PM_{2.5}$ dataset to analyze the characteristics of all events. Heat wave frequency is defined as the average number of heat wave days per year. Heat wave duration is defined as the average number of consecutive days in each heat wave over the entire study period. Cumulative (excessive) heat intensity is defined as the sum of temperature anomalies across all heat wave

days during the study period (Perkins-Kirkpatrick & Lewis, 2020). All three metrics were calculated using data from the reconstructed temperature dataset.

Standards for $PM_{2.5}$ pollution vary in different countries. In the U.S., the National Ambient Air Quality Standards established by the Environmental Protection Agency (U.S. EPA, 2024b) specify a 24-hour average $PM_{2.5}$ concentration of 35 μg m^{-3} for protecting both public health and welfare. In comparison, the World Health Organization (WHO, 2021) recommends a more stringent, evidence-informed standard aimed at reducing health risks: a 24-hour Air Quality Guideline (AQG) level of 15 μg m^{-3} for $PM_{2.5}$. This study adopts the WHO's AQG level, and a $PM_{2.5}$ pollution episode is defined as a period of one or more consecutive days with daily $PM_{2.5}$ concentration exceeding 15 μg m^{-3}. Similar to heat wave characteristics, the frequency of $PM_{2.5}$ pollution episodes is the average number of pollution days per year. The duration of $PM_{2.5}$ pollution episodes is defined as the average number of consecutive days in each pollution episode over the 17 years. Cumulative (excessive) $PM_{2.5}$ pollution intensity is defined as the sum of $PM_{2.5}$ concentration exceedances above the WHO's AQG level (15 μg m^{-3}) for all air pollution days during the study period.

A compound heat and $PM_{2.5}$ pollution episode is defined as a period of one or more consecutive days during which heat wave and $PM_{2.5}$ pollution conditions occur concurrently, i.e., daily $PM_{2.5}$ concentrations exceed 15 μg m^{-3} during a heat wave. The frequency of such compound extreme episodes is defined as the average number of days per year with concurrent heat and pollution conditions. The duration of compound events is the average number of consecutive days per event. Two cumulative intensity metrics are defined for compound events: cumulative heat intensity and cumulative $PM_{2.5}$ pollution intensity. Both intensity metrics are

based on the previously defined exceedance criteria but are limited to days during compound events.

2.2 Characteristics of heat waves based on minimum air temperatures

The vast majority of urban areas across the CONUS (98.8%) experienced more frequent heat waves, based on daily minimum air temperature, compared to their rural surroundings (Fig. 2.3a–c). On average, urban areas experienced 19.2 heat wave days annually, approximately 32% more than their rural counterparts (Table A1 in the Appendix). Regionally, urban areas in the Southwest and West recorded the highest heat wave frequencies among all nine climate regions (Note A1), similar to the frequency patterns reported for maximum temperature-based heat waves in a previous study (C. Wang et al., 2025). In particular, the Southwest had the highest frequency of 26.3 days per year. In contrast, the Upper Midwest showed the lowest frequency of urban heat waves, with only 9.8 days per year, suggesting substantial regional variability. Similar regional patterns were observed for rural areas, although with lower frequencies. The largest urban–rural differences, quantified as relative differences, occurred mainly in the West and Southwest, where annual urban heat wave days were nearly or even more than tripled compared to rural ones in cities such as Albuquerque, NM, Las Vegas, NV, and Phoenix, AZ.

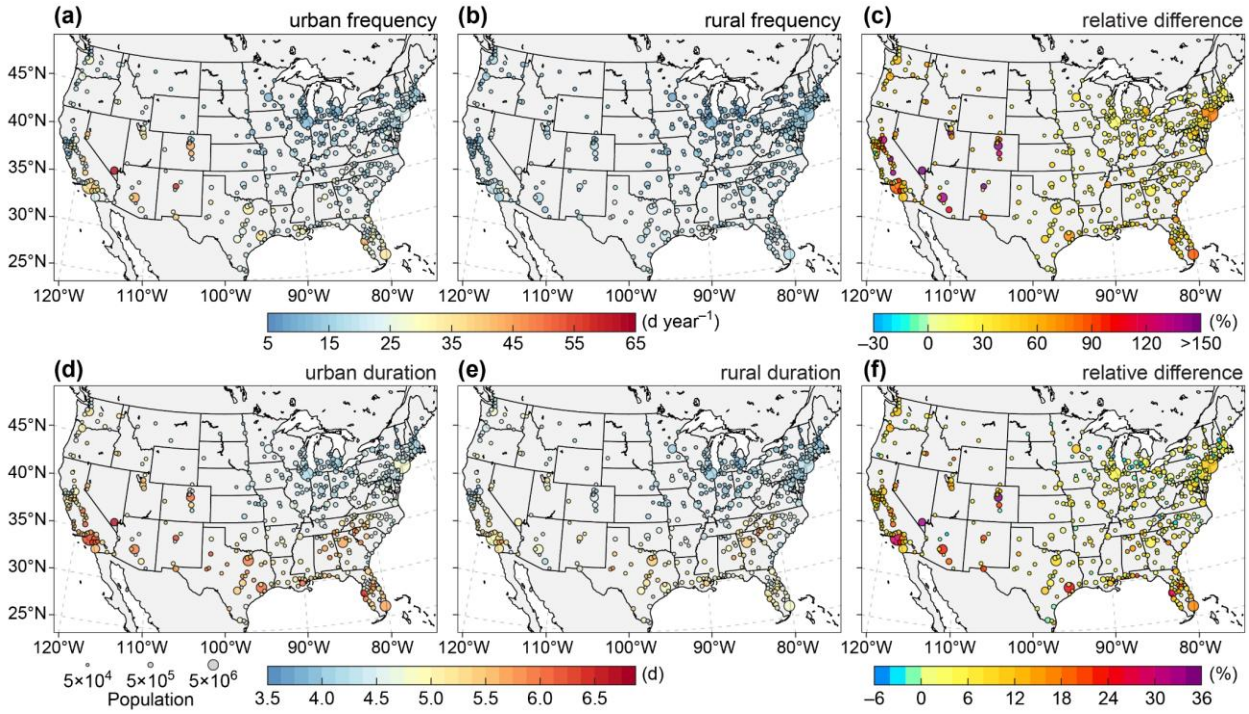


Figure 2.3. Frequency and duration of heat waves based on minimum temperatures in urban and surrounding rural areas: (a) frequency in urban areas, (b) frequency in rural areas, (c) relative difference in frequency between urban and rural areas (urban minus rural), (d) duration in urban areas, (e) duration in rural areas, and (f) relative difference in duration between urban and rural areas (urban minus rural). Filled circles represent individual urban and rural areas, with circle sizes scaled to urban population. White circles in (c) and (f) indicate no urban–rural differences.

The durations of minimum temperature-based heat waves were longer in 88.6% of CONUS urban areas compared to surrounding rural areas, although the average relative difference in duration was only 5.0% (Table A1). As shown in Fig. 2.3d, the longest heat wave durations were mainly found across urban areas in the West, Southwest, South, and Southeast climate regions. However, durations in the Northern Rockies and Plains, Upper Midwest, Ohio Valley, and Northeast were much shorter. Table A1 further highlights these regional disparities: urban areas in the South had the longest average heat wave durations at 5.1 days, while the

Upper Midwest had the shortest at 4.1 days. The greatest relative differences between urban and rural heat wave durations were observed in the West, Southwest, and Southeast, with relative differences exceeding 15%. In contrast, minimal differences (within ±3%) were mainly observed in the Northeast, Ohio Valley, Upper Midwest, Northern Rockies and Plains, and South. For some cities in the eastern U.S., urban heat wave durations were up to ~3.6% shorter than those in rural areas, representing the most notable cases of this pattern.

The cumulative heat intensity of minimum temperature-based heat waves was higher in 98.8% of urban areas compared to their rural counterparts (Fig. 2.4c), with an average urban–rural relative difference of 35.5%. This disparity is mainly attributed to the widespread nocturnal urban canopy layer heat island effect across the CONUS (Fig. 2.4d–f). Both urban and rural cumulative intensities peaked in the West (Fig. 2.4a and b), with substantially higher values observed in urban areas. As shown in Table A1, the greatest regional average urban cumulative heat intensity was recorded in the West at 1053.0°C, more than twice the lowest regional average in the Upper Midwest (404.9°C). While the highest rural cumulative heat intensity was also in the West at 670.5°C, the weakest cumulative intensity occurred in the rural Southeast (313.2°C). The largest relative differences between urban and rural cumulative heat intensities were found in the West, Southwest, and Southeast (Fig. 2.4c), with urban cumulative intensities were more than twice those of their rural surroundings in cities such as Albuquerque, NM, Las Vegas, NV, Phoenix, AZ, Denver, CO, and Miami, FL.

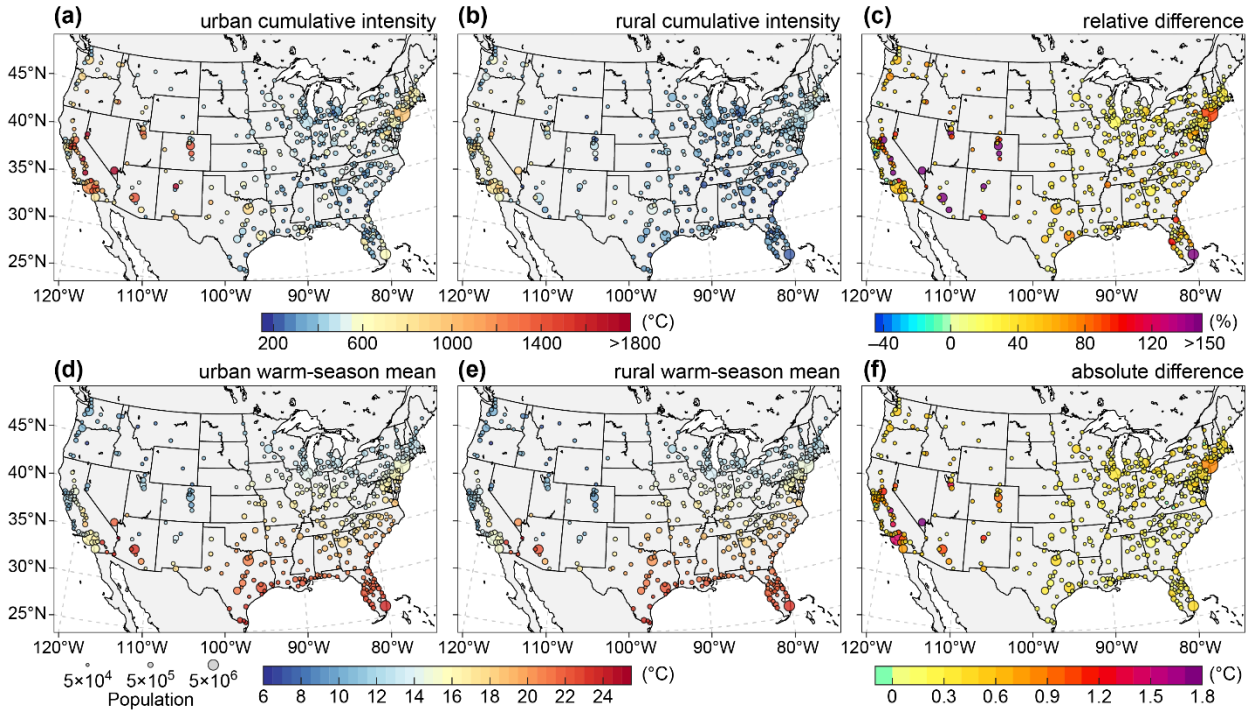


Figure 2.4. Cumulative intensity of heat waves based on minimum temperatures and warm-season mean minimum temperature in urban and surrounding rural areas: (a) cumulative heat intensity in urban areas, (b) cumulative heat intensity in rural areas, (c) relative difference in cumulative heat intensity between urban and rural areas (urban minus rural), (d) warm-season mean minimum temperature in urban areas, (e) warm-season mean minimum temperature in rural areas, and (f) difference in warm-season mean minimum temperature between urban and rural areas (urban minus rural). Filled circles represent individual urban and rural areas, with circle sizes scaled to urban population.

2.3 Characteristics of $PM_{2.5}$ pollution episodes

More frequent $PM_{2.5}$ pollution episodes were observed in 85.4% of urban areas compared to their surrounding rural areas (Fig. 2.5a–c). On average, urban areas experienced 23.7 days of excessive $PM_{2.5}$ pollution annually, while rural areas faced 22.7 days annually. Regionally, $PM_{2.5}$

pollution occurred most often in the Ohio Valley, Northeast, and upper Southeast across both urban and rural areas. In particular, urban areas in the Ohio Valley had the most frequent $PM_{2.5}$ pollution episodes, occurring 36.9 days per year. In contrast, cities in the Southwest had the fewest $PM_{2.5}$ pollution episodes, averaging only 5.5 days annually. The most substantial urban–rural relative differences in frequency occurred in Southern California, exceeding 70% (Fig. 2.5c). Across other climate regions, relative differences in general ranged between 0% and 30%, with slightly elevated values along coastal areas in the Northwest and Southeast. A few urban areas had lower pollution episode frequencies than rural surroundings, particularly in the Ohio Valley, Upper Midwest, Northeast, and upper Southeast.

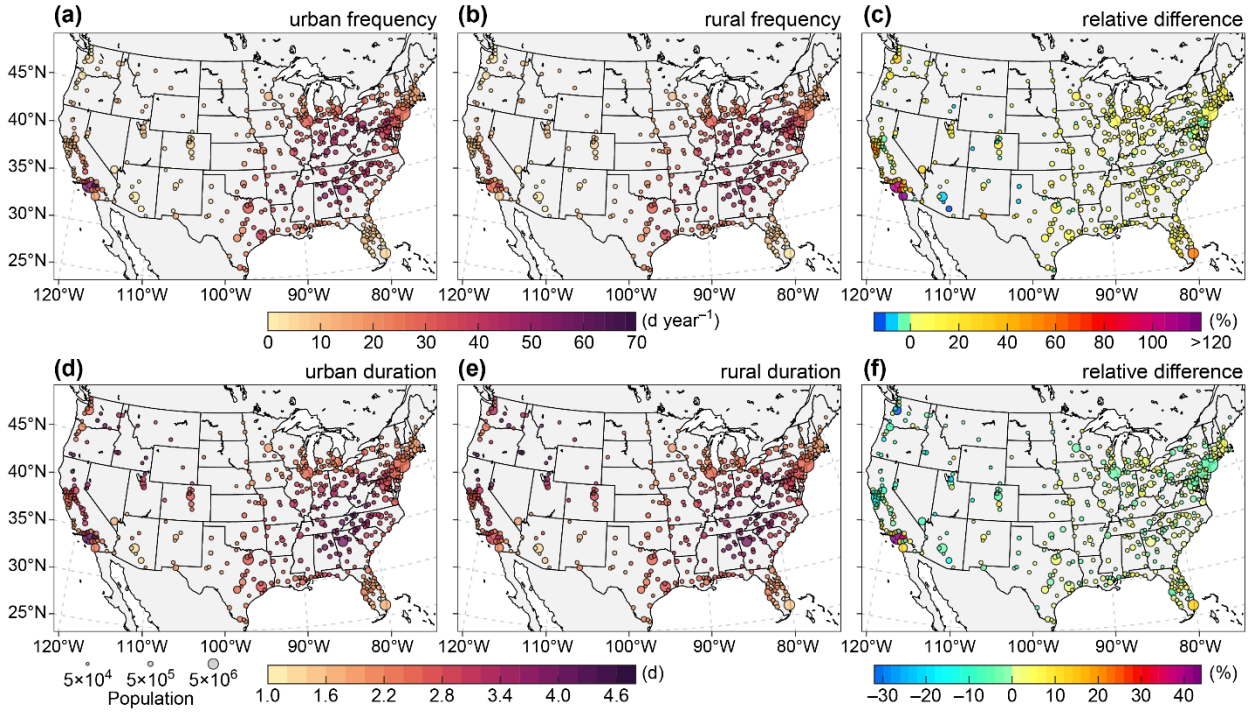


Figure 2.5. Frequency and duration of $PM_{2.5}$ pollution episodes in urban and surrounding rural areas: (a) frequency in urban areas, (b) frequency in rural areas, (c) relative difference in frequency between urban and rural areas (urban minus rural), (d) duration in urban areas, (e)

duration in rural areas, and (f) relative difference in duration between urban and rural areas (urban minus rural). Filled circles represent individual urban and rural areas, with circle sizes scaled to urban population. White circles in (c) and (f) indicate no urban–rural differences.

$PM_{2.5}$ pollution episodes lasted longer in 52.8% of CONUS urban areas compared to their rural counterparts. The spatial pattern of $PM_{2.5}$ pollution durations was similar to that of frequency in most climate regions, with the longest durations recorded in the Northwest, Ohio Valley, upper Southeast, and Southern California across both urban and rural areas (Fig. 2.5d and e). Urban areas in the Northwest experienced the longest episodes, averaging 3.1 days. Meanwhile, the shortest durations for $PM_{2.5}$ pollution episodes were found in the Upper Midwest at 2.2 days (Table A2 in the Appendix). Overall, urban–rural relative differences in $PM_{2.5}$ pollution duration were low across much of the CONUS, the majority of which fell within ±10%. The largest relative differences of over 30% were found in Southern California. Additionally, the share of urban areas with shorter episode durations than their rural surroundings was substantially higher than the share with lower episode frequency.

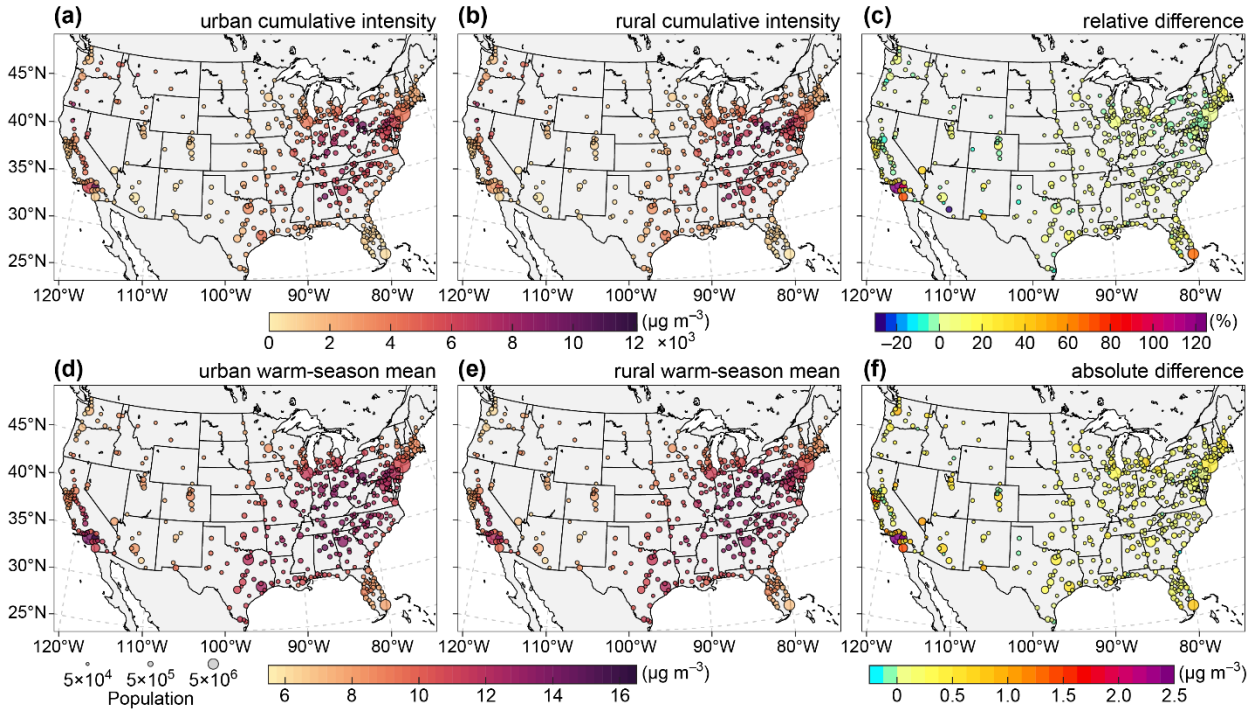


Figure 2.6. Cumulative intensity of $PM_{2.5}$ pollution episodes and warm-season mean $PM_{2.5}$ concentration in urban and surrounding rural areas: (a) cumulative $PM_{2.5}$ pollution intensity in urban areas, (b) cumulative $PM_{2.5}$ pollution intensity in rural areas, (c) relative difference in cumulative $PM_{2.5}$ pollution intensity between urban and rural areas (urban minus rural), (d) warm-season mean $PM_{2.5}$ concentration in urban areas, (e) warm-season mean $PM_{2.5}$ concentration in rural areas, and (f) difference in warm-season mean $PM_{2.5}$ concentration between urban and rural areas (urban minus rural). Filled circles represent individual urban and rural areas, with circle sizes scaled to urban population.

The cumulative pollution intensity of $PM_{2.5}$ pollution episodes was greater in 80.5% of urban areas compared to surrounding rural areas. The highest cumulative intensities were observed across the Ohio Valley, Northeast, and upper Southeast (Fig. 2.6a–c and Table A2). The patterns of urban and rural cumulative pollution intensities were generally comparable, except in Southern California, where urban values were notably higher. Regionally, Ohio Valley

had the highest cumulative intensities, averaging 5513.9 μg m^{-3} in urban areas, while the Southwest had the lowest urban mean of 745.4 μg m^{-3} (Table A2). The largest urban–rural relative difference in cumulative pollution intensity was observed in Southern California (> ~100%) (Fig. 2.6c). In addition, high relative differences were noted in cities such as Miami, FL, El Paso, TX, and Las Vegas, NV. In contrast, negative urban–rural relative differences (i.e., lower urban cumulative pollution intensity) were scattered mainly across the Northeast and South. Consistent with the spatial patterns of pollution episodes, warm-season mean $PM_{2.5}$ concentrations were highest in the Ohio Valley, upper Southeast, South, Northeast, and California. The greatest regional mean urban $PM_{2.5}$ concentration was in the Ohio Valley, reaching 12.2 μg m^{-3}, while the lowest was in the Northwest at 7.3 μg m^{-3} (Table A2). Absolute mean differences between urban and rural mean $PM_{2.5}$ concentrations were greatest in Southern California, ranging from 1.0 μg m^{-3} to 2.5 μg m^{-3} for some cities (Fig. 2.6f).

2.4 Characteristics of compound heat and $PM_{2.5}$ pollution episodes

Approximately 97.9% of urban areas experienced more frequent compound heat and $PM_{2.5}$ pollution events compared to their surrounding rural areas. These compound events occurred frequently in the Northeast, Ohio Valley, South, upper Southeast, and California (Fig. 2.7a–c). Regionally, the highest frequency for urban areas was in the Ohio Valley at approximately 4.5 days $year^{-1}$ (Table A3 in the Appendix). The highest rural mean frequency was also observed in this region, which was about 3.4 days $year^{-1}$. Compound events were least frequent in the Southwest, averaging only 1.5 days $year^{-1}$ in urban areas and 1.0 day $year^{-1}$ in rural areas. A comparison of urban and rural compound event frequencies reveals that the

greatest relative differences (over 150%) were located in the West, Southwest, and coastal areas of the Southeast (Fig. 2.7c).

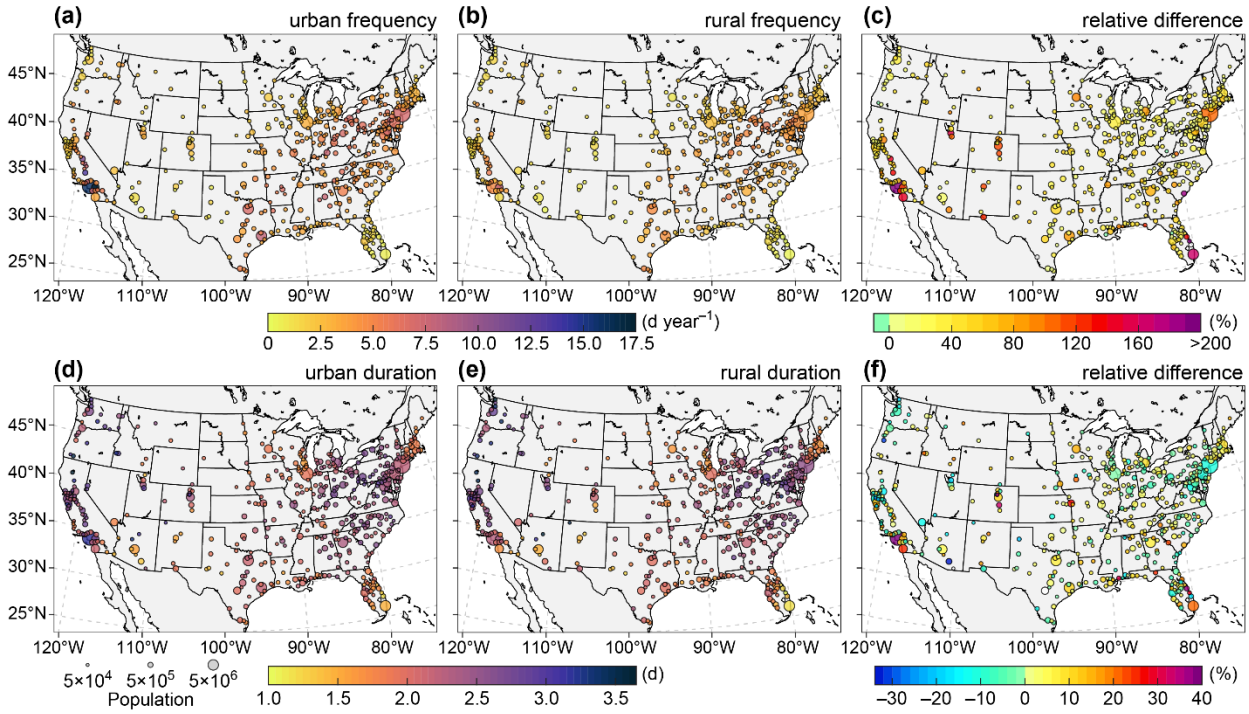


Figure 2.7. Frequency and duration of compound heat and $PM_{2.5}$ pollution episodes in urban and surrounding rural areas: (a) frequency in urban areas, (b) frequency in rural areas, (c) relative difference in frequency between urban and rural areas (urban minus rural), (d) duration in urban areas, (e) duration in rural areas, and (f) relative difference in duration between urban and rural areas (urban minus rural). Filled circles represent individual urban and rural areas, with circle sizes scaled to urban population. White circles in (c) and (f) indicate no urban–rural differences.

The durations of compound heat and $PM_{2.5}$ pollution events were longer in 58.8% of CONUS urban areas compared to their rural counterparts. As shown in Fig. 2.7d–f, these events were most prolonged in the Northeast, Ohio Valley, upper Southeast, Northwest, and West.

Among these regions, the longest durations were observed in the Northwest, where urban and rural areas averaged 2.6 and 2.7 days, respectively (Table A3). The South, however, had the shortest average duration of 2.0 days in urban areas. Urban areas with substantially lower compound event duration than their rural surroundings were scattered across all climate regions. Similarly, areas with the largest urban–rural relative differences in frequency (>100%) were dispersed across the continent, with notable examples in major cities such as Los Angeles, CA, Miami, FL, Salt Lake City, UT, Denver, CO, and Albuquerque, NM.

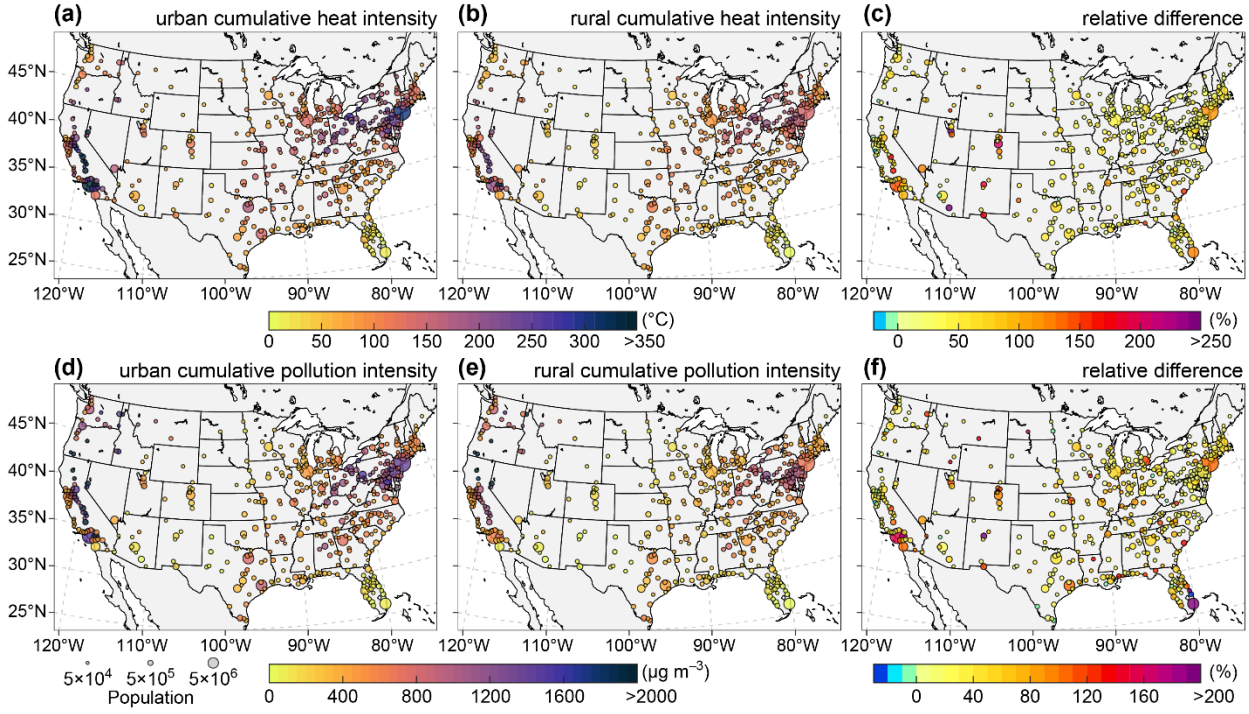


Figure 2.8. Cumulative intensity of compound heat and $PM_{2.5}$ pollution episodes in urban and surrounding rural areas: (a) cumulative heat intensity in urban areas, (b) cumulative heat intensity in rural areas, (c) relative difference in cumulative heat intensity between urban and rural areas (urban minus rural), (d) cumulative $PM_{2.5}$ pollution intensity in urban area, (e) cumulative $PM_{2.5}$ pollution intensity in rural area, and (f) relative difference in cumulative $PM_{2.5}$

pollution intensity between urban and rural areas (urban minus rural). Filled circles represent individual urban and rural areas, with circle sizes scaled to urban population.

As shown in Fig. 2.8a–c, cumulative heat intensities during compound heat and $PM_{2.5}$ pollution events were highest in the Northeast, Ohio Valley, and West. Overall, 98.3% of urban areas had greater cumulative heat intensities compared to their rural surroundings. Regionally, the highest cumulative heat intensities were observed in the Northeast, reaching on average 161.1°C in urban areas (Table A3). In contrast, the lowest values were found in the Southwest, where urban areas averaged only 57.5°C. The largest urban–rural relative differences in cumulative heat intensity (> 150%) were predominantly observed in the Southwest and West (Fig. 2.8c). However, some isolated locations in the Southeast and South, such as El Paso, TX, also exhibited large urban–rural relative differences.

During compound heat and $PM_{2.5}$ pollution episodes, 97.3% of CONUS urban areas experienced greater cumulative pollution intensities than their surrounding rural areas. The highest cumulative $PM_{2.5}$ pollution intensities for both urban and rural areas were observed in the Northeast, Northwest, and West (Fig. 2.8d–f). Different from cumulative heat intensities during compound events, Northwest exhibited the greatest cumulative $PM_{2.5}$ pollution intensities, reaching on average 1107.0 μg m^{-3} across urban areas. In comparison, the lowest values were recorded in the Southwest: on average 189.4 μg m^{-3} in urban areas and 124.1 μg m^{-3} in rural areas (Table A3). Urban–rural disparities in cumulative pollution intensity varied substantially in space. The largest relative differences (> 200%) were mainly concentrated in the Southeast, Southwest, and West and Southwest, with additional isolated cases in the Northwest and South (Fig. 2.8f).

2.5 Comparison and attribution of single and compound extremes

Analysis of heat wave characteristics across the CONUS reveals that heat waves in urban areas, defined by daily minimum air temperature in this study, were generally more frequent, longer lasting, and more intense than in rural areas (Figs. 2.3–2.4). These findings are consistent with previous observations and numerical simulations at regional and global scales: heat waves can amplify nighttime urban heat islands and escalate urban–rural temperature differences (D. Li & Bou-Zeid, 2013; Liao et al., 2018; L. Zhao et al., 2018). This synergistic effect mainly results from the heat retention of construction materials, the lack of surface moisture, and anthropogenic heat emissions (Barriopedro et al., 2023). Heat waves occurred most frequent in inland urban areas of the West and Southwest where the urban–rural relative differences were also the greatest (Fig. 2.3a and c). In comparison, coastal cities in the West (i.e., California) experienced less frequent heat waves, likely influenced by the nearby ocean. Heat waves lasted the longest in urban areas across the southern U.S., where the largest urban–rural differences in duration were found. Interestingly, in the eastern U.S., urban areas exhibited both longer and shorter heat wave durations than their rural surroundings (Fig. 2.3f). This disparity is because some urban areas experienced more frequent but shorter individual heat waves when minimum air temperature in rural areas fell below the heat wave threshold.

Despite shorter average durations in some cities, nearly all urban areas experienced higher cumulative heat intensity than rural areas (Fig. 2.4c). The consistent spatial patterns between nighttime UHI intensity (Fig. 2.4f) and urban–rural heat wave differences indicates that the urban–rural contrast is primarily driven by the nighttime UHI effect. However, the extent to which the nighttime UHI influenced this contrast varied by region and was modulated by climatic conditions (Liao et al., 2018). Notably, several cities in Florida (e.g., Miami) had

substantially more severe heat wave conditions than their rural surroundings, despite relatively low UHI intensity. In addition, larger cities, characterized by higher population here, tended to exhibit greater urban–rural differences in heat wave frequency and cumulative intensity, as well as higher nighttime UHI intensity, compared to their surrounding smaller cities. This pattern highlights the potentially amplified influence of large urban areas on local and even regional climatic conditions (Manoli et al., 2019; Oke et al., 2017; Ramamurthy & Bou-Zeid, 2017; B. Zhou et al., 2013).

$PM_{2.5}$ pollution episodes were also more frequent, longer lasting, and more intense in urban areas than in rural areas, largely due to higher urban emissions (e.g., Fig. A1g in the Appendix). In fact, over 91% of urban areas were more polluted than their rural surroundings in terms of warm-season $PM_{2.5}$ concentrations. In particular, $PM_{2.5}$ pollution episodes were the most frequent, persistent, and intense in both urban and rural areas across the eastern U.S., excluding Florida, and in Southern California (Figs. 2.5–2.6). Several cities in Southern California (e.g., Los Angeles) exhibited the most substantial urban–rural relative differences in the frequency, duration, and cumulative intensity of $PM_{2.5}$ pollution episodes, which is in alignment with findings from previous shorter-period studies (Chakraborty et al., 2022; Eiguren-Fernandez et al., 2004; Meng et al., 2018). These substantial differences are due to higher urban emissions from traffic, industrial activities, as well as wildfires (Chow et al., 2006; B. Yang et al., 2024). In addition, the topography of Southern California, where many cities are surrounded by mountains, traps air pollution and allows it to accumulate and persist over extended periods (C. Wang et al., 2017). Fig. A1f illustrates this pattern in Los Angeles and surrounding cities.

The spatial patterns of urban–rural differences in $PM_{2.5}$ pollution episodes were relatively more heterogeneous than those observed for heat waves (Figs. 2.5–2.6, cf. Figs. 2.3–2.4). In

many urban areas, the frequency, duration, and cumulative pollution intensity were lower than in rural areas, especially for episode duration (Fig. 2.5f). Some cities even recorded lower warm-season mean $PM_{2.5}$ concentrations than nearby rural areas. This is partly explained by the transport of urban pollutant emissions toward downwind rural areas for some cities (e.g., Fig. A1h), which can lead to higher rural concentration and the formation of secondary $PM_{2.5}$ (X.-M. Hu et al., 2008; Kim et al., 2016). Additionally, rural emissions from biomass burning and agricultural dust (Lei et al., 2016; X. Li et al., 2020) can contribute to elevated $PM_{2.5}$ levels, as evidenced by higher $PM_{2.5}$ concentrations over agricultural lands south of Phoenix (Fig. A1e). Urban–rural contrasts in $PM_{2.5}$ pollution episodes can also diminish due to synoptic weather conditions, unique regional emission patterns, and geographical controls. For example, stagnant weather in the eastern U.S. can result in similar $PM_{2.5}$ levels across urban and rural areas. Secondary $PM_{2.5}$ formation from emissions associated with industrial activities and coal-fired power plants in the eastern U.S., agricultural ammonia emissions in the Midwest, and biogenic emissions in the Southeast can further reduce urban–rural differences (Bauer et al., 2016; McDuffie et al., 2021; Skyllakou et al., 2021; Wyer et al., 2022). In California's Central Valley, the shared topographical constraints can limit the ventilation of pollutants, leading to similar $PM_{2.5}$ levels between urban and rural areas, despite high warm-season mean concentrations (Fig. 2.6d–f).

Compound heat and $PM_{2.5}$ pollution episodes were more frequent and more intense, in terms of both heat and pollution, in ~98% of CONUS urban areas compared to their rural counterparts (Figs. 2.7c, 2.8c, and 2.8f). However, only slightly more than half of urban areas experienced longer lasting compound events than nearby rural areas (Fig. 2.7f). Regionally, the eastern U.S. (excluding Florida) and California had the most frequent and longer lasting

compound events. Cumulative heat and pollution intensities for both urban and rural areas showed similar spatial patterns, with the greatest intensities occurring in California and most states across the eastern U.S. (Fig. 2.8). The largest urban–rural relative differences in cumulative heat and pollution intensities were observed in the West and Southwest, along with a few outliers on the East Coast, such as Miami, FL. These outlier cities in the eastern U.S. typically had low frequency, duration, and cumulative intensities. The high relative difference actually reflects the ratio of two low values, with urban intensities slightly higher than rural ones. In general, the spatial patterns of compound event characteristics for both urban and rural areas more closely resembled those of $PM_{2.5}$ pollution episodes than those of heat waves (Figs. 2.7–2.8, cf. Figs. 2.3–2.6). This suggests that the spatial distributions of compound events were primarily driven by $PM_{2.5}$ pollution episodes, despite their relatively shorter duration compared to that of either heat waves or $PM_{2.5}$ pollution events. Consequently, regions with high $PM_{2.5}$ frequency, duration, and cumulative intensity also tended to experience more frequent, prolonged, and intense compound heat and $PM_{2.5}$ pollution events. These regions should be prioritized in the implementation of heat and pollution mitigation strategies.

2.6 Post-2016 reversal in $PM_{2.5}$ and its impact on compound events

The study period (2000–2022) encompasses a unique transition in national air quality trends, marked by an initial decrease in warm-season $PM_{2.5}$ concentrations, followed by a reversal starting around 2016. As shown in Fig. A2 in the Appendix, both urban and rural areas experienced statistically significant decreasing trends in mean $PM_{2.5}$ levels prior to ~2016 ($p < 0.01$), and statistically significant increase thereafter ($p < 0.02$). As pointed out in a recent study (Burke et al., 2023), this post-2016 rebound in $PM_{2.5}$ levels was primarily attributed to the

escalating influence of wildfire activities. Wildfires, particularly in the western U.S., have grown in both size and intensity, collectively due to climate change, accumulated fuel loads, and increased human-related ignitions (Balch et al., 2017; Boisramé et al., 2022; Juang et al., 2022; Westerling, 2016). Burke et al. (2023) estimated that these changes have offset approximately one-quarter of the multi-decadal improvements in air quality across many CONUS states. These shifts in pollution levels likely altered the characteristics and frequency of extreme pollution events, particularly during the warm season.

A thorough comparison of event characteristics between the entire 23-year study period and the earlier years (2000–2016) further confirms this shift. During the earlier period (2000–2016), the characteristics of heat waves, including urban–rural contrasts, remained relatively stable, with limited change in frequency and cumulative heat intensity compared to the entire 23-year period (Figs. A3–A4 and Table A4 in the Appendix). In contrast, $PM_{2.5}$ pollution episodes and compound heat and pollution events exhibited notably higher frequency, duration, and cumulative intensities across many climate regions in the western U.S. (Figs. A5–A8 and Tables A3–A4). For example, in states such as Oregon and Washington, urban–rural differences in frequency and cumulative intensity, which were clearly evident during 2000–2016, were substantially diminished when considering the full 23-year period. This weakened urban–rural contrast results from the dominance of widespread wildfire smoke, which largely obscures the urban pollution signal. A similar pattern was observed for compound events as well, with wildfire-driven pollution increasingly changing the frequency and cumulative intensity across the western U.S.

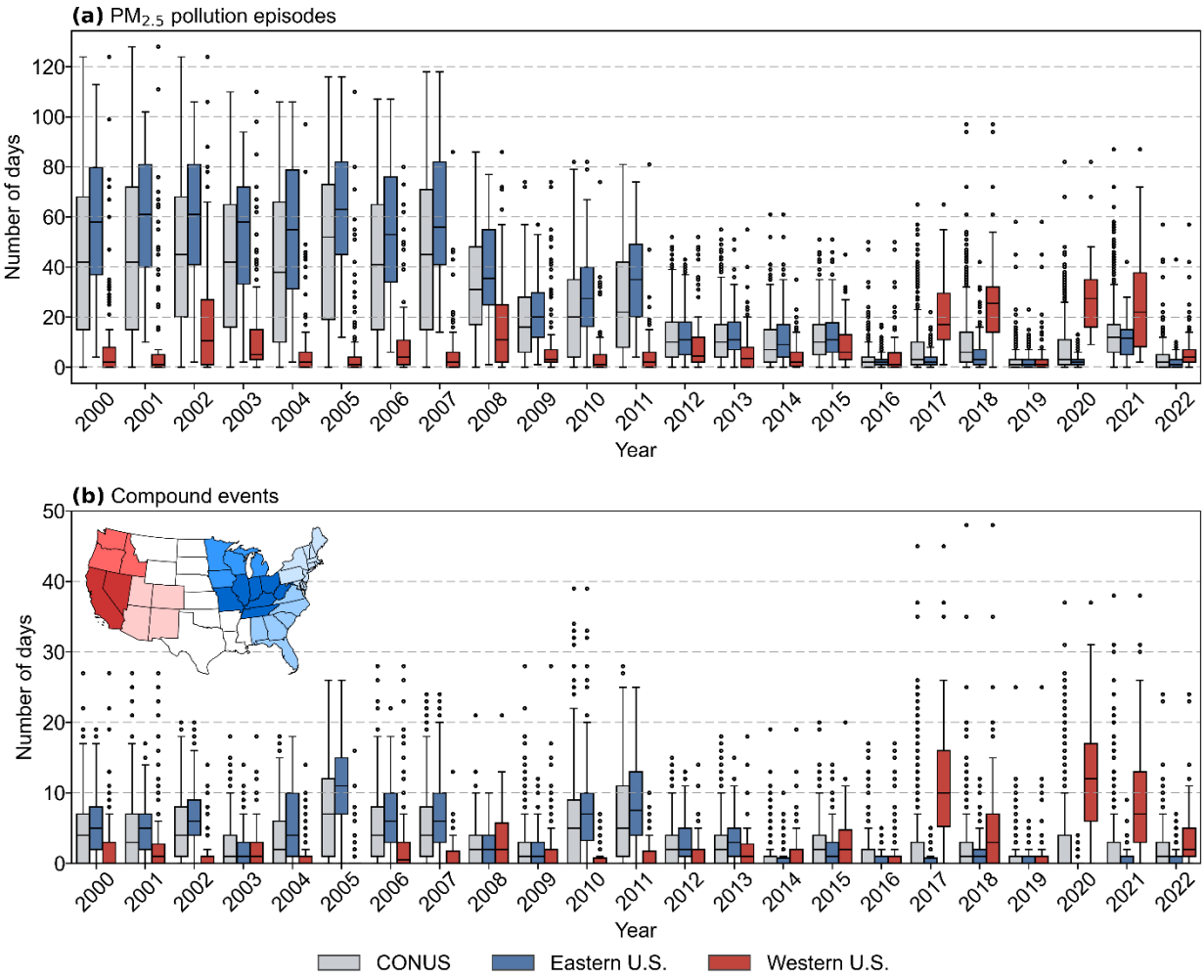


Figure 2.9. Annual frequency of (a) $PM_{2.5}$ pollution episodes and (b) compound events, measured as the number of event days in urban areas across the CONUS, eastern U.S. (Northeast, Upper Midwest, Ohio Valley, and Southeast), and western U.S. (Southwest, Northwest, and West). Each box shows the interquartile range (IQR), with the horizontal line indicating the median, whiskers extending to 1.5 × IQR, and points beyond the whiskers representing outliers. The inset in (b) shows the climate regions used to define the eastern and western U.S. (blue and red, respectively).

The annual analysis of event days further reveals regional contrasts across the CONUS (Fig. 2.9). Nationally, the number of $PM_{2.5}$ pollution days and compound event days declined

until around 2016, followed by a plateau in subsequent years. This trend was also evident in the eastern U.S. However, the western U.S. experienced a substantial post-2016 increase in both $PM_{2.5}$ pollution and compound event days, albeit with some year-to-year variability. Notably, several recent years (e.g., 2020 and 2021) even surpassed the levels observed during 2000–2016. These findings imply the growing challenge of managing urban air quality, as the rising influence of long-range wildfire smoke can increasingly undermine the effectiveness of local emission control efforts. Current regulatory frameworks may fall short under such conditions, highlighting the urgent need for integrated strategies that combine urban emission control with regional-scale fuel and land management to protect both environmental quality and public health.

2.7 Limitations and uncertainties

This study has several limitations that should be acknowledged. First, our analysis is indirectly based on observational datasets, and thus inevitably inherits uncertainties from the input datasets of the machine learning models, despite their extensive validation (e.g., Di et al., 2019; Wei et al., 2023). In addition, while our threshold-based approach captures major pollution events, it does not fully reflect the potential health risks associated with lower-level $PM_{2.5}$ pollution exposure, as even concentrations below WHO guidelines have been shown to pose risks to public health (McDuffie et al., 2021). This necessitates caution when interpreting the health implications of our findings. Furthermore, the use of daily $PM_{2.5}$ levels limits our ability to examine the diurnal variability of exposure, particularly for heat stress and pollution peaks that may occur at specific hours of the day as influenced by emission patterns and weather conditions. Future work incorporating hourly or sub-daily data, when available, would offer a more detailed understanding of potential exposure risks. Lastly, our data-driven approach does

not explicitly evaluate physical mechanisms or causal drivers. However, it serves as a critical first step by identifying spatial patterns and high-risk regions that warrant further investigation into underlying processes and the development of targeted mitigation strategies.

Chapter 3

Integrated observational and modeling analysis of urban methane emissions: A landfill case study

This chapter presents a multiscale characterization of CH_4 emissions from a municipal solid waste landfill in Oklahoma City using concurrent mobile and satellite observations collected on December 13th, 2025, in combination with high-resolution WRF-Chem simulations. Mobile transect measurements conducted around the landfill perimeter were used to determine near-surface CH_4 distributions from early morning to late afternoon. In addition, satellite-derived CH_4 column data provided independent emission estimates and offered a spatially continuous view of the CH_4 plume at a broader scale. WRF-Chem simulations were used alongside mobile observations to inversely estimate the landfill CH_4 emission rate, by calculating the ratio of observed to simulated cross-plume CH_4 enhancements and applying it to the prescribed emission rate. A comparative analysis of mobile, satellite, and simulated CH_4 was then used to evaluate the consistency of emission estimates across observational and modeling approaches. This study aims to improve confidence in landfill CH_4 emission estimates and demonstrate the value of integrating concurrent, multiscale observations with high-resolution simulations.

3.1 Methodology

3.1.1 Study area and measurement overview

The Republic Services Southeast Landfill (35.3996°N, –97.4638°W) is an active municipal solid waste facility located in the southeastern Oklahoma City metropolitan area (Fig. 3.1). The landfill accepts MSW and is equipped with an active landfill gas (LFG) collection

system that converts captured gas to renewable natural gas (RNG) for energy use (Republic Services, 2018). Despite the gas collection system, there are fugitive CH_4 emissions from uncollected or poorly captured landfill gas, particularly from active tipping areas and imperfectly sealed cover sections. Their cover system uses two feet of compacted clay, a synthetic liner, topsoil, and vegetation. Mobile and satellite CH_4 measurements were conducted at the landfill site on December 13th, 2025, when skies were clear and winds were generally out of the north to northeast, advecting the landfill CH_4 plume to the south and southwest of the facility. December 13th, 2025 was also selected in part because winter conditions favor elevated fugitive CH_4 emissions at landfill sites, as low soil temperatures suppress the activity of methane-oxidizing bacteria in the cover layer, reducing the amount of CH_4 oxidized before reaching the surface (Börjesson & Svensson, 1997; Chanton & Liptay, 2000).



Figure 3.1. Satellite view of Republic Services Southeast Landfill in Oklahoma City.

3.1.2 Mobile CH_4 measurements and data processing

Near-surface CH_4 concentrations were collected using a vehicle-mounted LI-COR 7810 trace gas analyzer, paired with a GR-9029 Real-Time Kinematic Global Navigation Satellite System GPS receiver for precise location tracking. The LI-COR 7810 is a cavity ring-down spectroscopy instrument that provides continuous, high-frequency measurements of CH_4 concentrations in parts-per-billion (ppb). This instrument has a CH_4 measurement range of 0–100 ppm, a response time of 2 seconds, a precision of 0.25 ppb with 5-second averaging, and a maximum drift of less than 1 ppb per 24-hr period (LI-COR, 2026). Together, the two instruments recorded CH_4 concentration, geographic coordinates, and timestamps throughout the measurement period. The mobile measurement strategy included sampling the broader perimeter around the landfill to collect background CH_4 concentrations (Fig. 3.2a) and transects along east-west roadways (specifically Interstate 240) to sample the CH_4 plume advected southward by the predominately northerly winds on December 13th, 2025 (Fig. 3.2b). Driving perpendicular to the wind direction along these transects is best for capturing the cross-sectional CH_4 distribution needed for estimating emission rates.

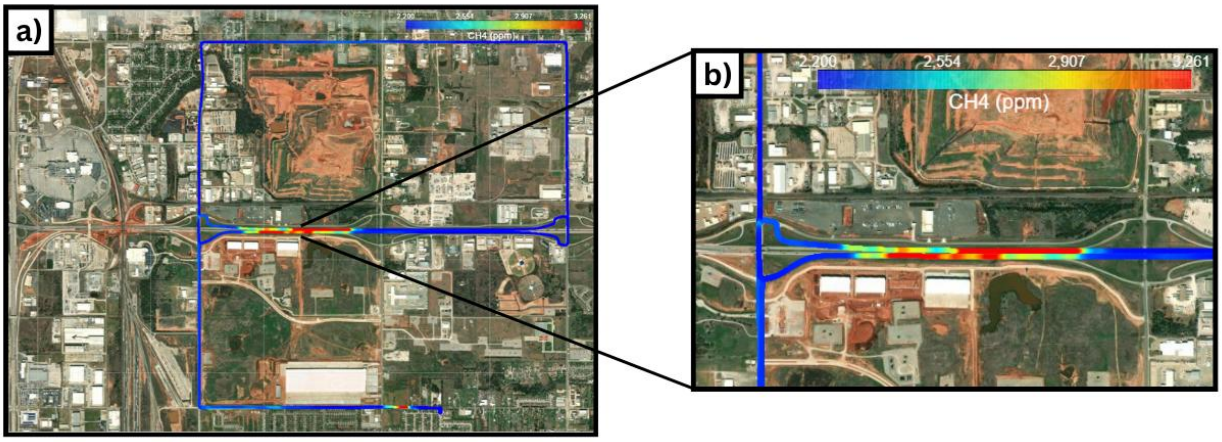


Figure 3.2. Mobile measurement route around Republic Services Southeast Landfill in Oklahoma City, including (a) larger perimeter and (b) the transect along Interstate 240.

The LI-COR and GPS data were first combined by matching their timestamps, creating a dataset that links CH_4 concentrations to location along the measurement route (Fig. 3.3). Fill values were removed during quality control, and the dataset isolated the relevant measurement window for December 13th, 2025. Background CH_4 levels were estimated using measurements collected away from the landfill and CH_4 enhancements were calculated as the difference between observed values within the CH_4 plume and background values. The data were then mapped to visually examine how CH_4 concentrations vary across the plume. Finally, the processed mobile observations were utilized with WRF-Chem simulations to estimate landfill CH_4 emission rates.

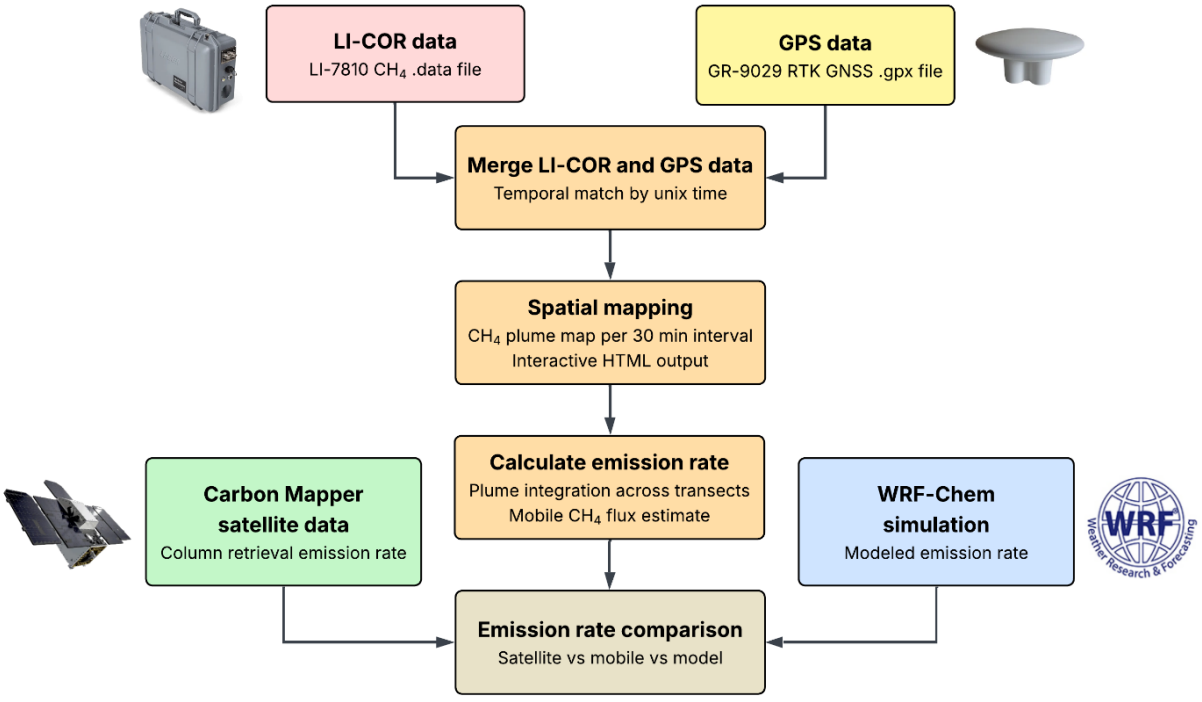


Figure 3.3. Flowchart of mobile CH_4 measurement data post-processing steps and multi-source emission rate comparison for the Oklahoma City landfill.

3.1.3 Satellite CH_4 observations and emission rate estimation

Satellite CH_4 observations were obtained from Carbon Mapper's Tanager-1 satellite, a hyperspectral imaging spectrometer operated by Planet Labs. Tanager-1 captures radiance across a broad spectral range (400–2500 nanometers) and retrieves column-averaged CH_4 concentrations in units of parts-per-million times meters (ppm·m) at a ground sampling distance of approximately 30–43 m, depending on look angle (Carbon Mapper, 2025). The satellite overpass over the Oklahoma City landfill occurred at 18:10:12 UTC (12:10:12 CST) on December 13th, 2025, providing a near-concurrent snapshot of the CH_4 plume during the mobile measurement. The retrieved column enhancement product serves as the basis for plume detection and emission rate quantification.

Emission rates from the Tanager-1 observations were estimated using Carbon Mapper's Integrated Mass Enhancement (IME) approach, which calculates the total excess mass of CH_4 within a plume above a dynamically determined concentration threshold (Carbon Mapper, 2024). This threshold is estimated for each plume based on the background noise in the immediate vicinity of the plume origin, using an optimized percentile and spatial crop pair applied to the retrieved concentration map. The IME is then combined with the plume fetch length and a 10-m wind speed to calculate an emission rate in units of kilograms of CH_4 per hour. Wind speed data was from the High-Resolution Rapid Refresh (HRRR) reanalysis product rather than observations, which introduces some uncertainties. The plume mask used for the IME calculation was created by grouping nearby pixels above the concentration threshold around the plume origin, however, Carbon Mapper also provides a visualization plume which captures more pixels to show the full visual aspect of a plume for human eyes. This visualization plume uses a

separate dynamic thresholding approach based on progressively cropped windows around the plume origin with pixel confidence scoring to capture more low-concentration pixels (Carbon Mapper, 2024).

3.1.4 WRF-Chem model configuration and scaling

WRF-Chem simulations were configured with four nested domains, centered over the Oklahoma City landfill site (Fig. 3.4). The outermost domain (d01) had a horizontal grid spacing of 12 km, followed by 800 m (d02), then 160 m (d03), and 32 m in the innermost domain (d04), which encompasses the landfill and its immediate surroundings at large-eddy simulation scale. The 12-hour simulation for December 13th, 2025, used the greenhouse gas passive tracer option to simulate CH_4 transport without chemical reactions (Table 3.1). A similar WRF-GHG LES configuration with 32 m grid spacing has been previously evaluated and shown to successfully simulate CH_4 plume enhancements and their diurnal variability under evolving boundary layer conditions comparable to those observed on December 13th, 2025, providing confidence in the model configuration used here (X.-M. Hu et al., 2025).

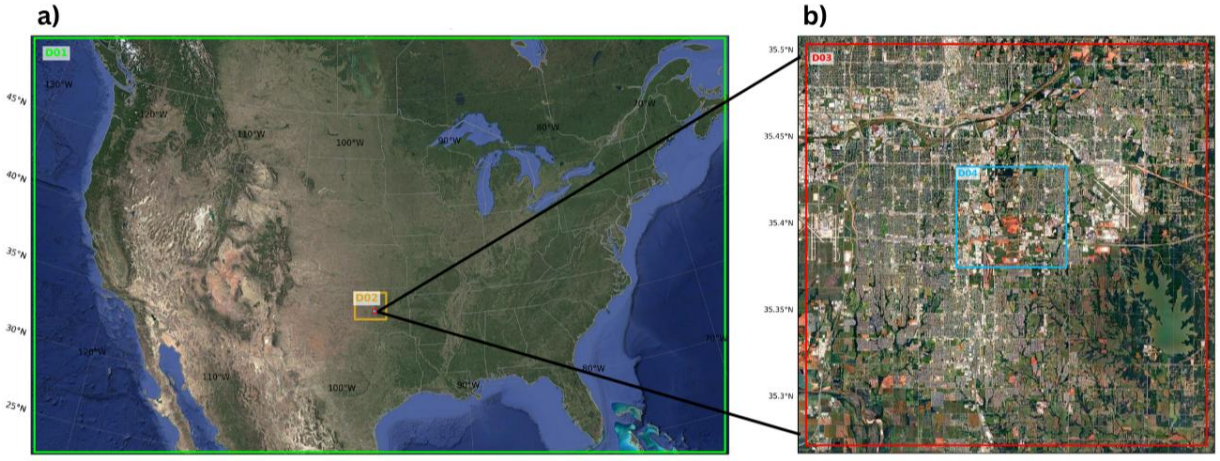


Figure 3.4. WRF-Chem nested domain configuration for Oklahoma City landfill site simulations: (a) outer domains D01 (green) and D02 (yellow), and (b) inner domains D03 (red) and D04 (blue).

Table 3.1. WRF-Chem physics and chemistry parameterization schemes used in the December 13th, 2025 simulation.

Scheme Type	Scheme Name
Microphysics	Morrison 2-moment
Longwave radiation	Rapid Radiative Transfer Model (RRTM)
Shortwave radiation	Dudhia
Surface layer	Revised MM5 Monin-Obukhov
Land surface	Noah land surface model
Planetary boundary layer	Mellor-Yamada-Janjić (MYJ)
PBL/SGS turbulence	Disabled (LES mode); Smagorinsky first-order closure for SGS mixing
Cumulus convection	Grell-Freitas ensemble
Chemistry	WRF-GHG greenhouse gas passive tracer

To inversely estimate the landfill CH_4 emission rate, simulated near-surface CH_4 concentrations from the innermost domain (d04) were extracted and compared to the mobile observations along the plume transects. A scaling factor (R) was calculated as the ratio of observed to simulated cross-plume CH_4 enhancements at the same location and time $R = \Delta CH_4obs / \Delta CH_4sim$ (X.-M. Hu et al., 2025; Ye et al., 2020). The real emission rate is then estimated by multiplying the modeled emission rate by this factor $Q_{real} = Q_{sim} \times R$. This approach uses the mobile measurements to improve the model and produce an emission estimate that can be compared with the satellite-based estimate.

3.1.5 Key CH_4 variable definitions

To evaluate consistency across the observational and modeling methods, their derived emission rate estimates were directly compared and their differences were analyzed. Before presenting the results, it is helpful to define three key quantities used in this chapter. CH_4 concentration refers to the total amount of methane measured in the atmosphere, reported in ppb for mobile measurements or in column unit ppm·m for satellite data. CH_4 enhancement is the excess concentration above background level, representing the landfill's contribution to the measured CH_4. As previously mentioned, the background is estimated using measurements collected away from the landfill, and enhancements are calculated by subtracting this background from the total concentration. CH_4 emission rate is the amount of methane released from the landfill per unit time, reported in kg CH_4 hr^{-1}. Differences in emission estimates reflect both the different types of data each approach provides and the assumptions used in each method, which will be discussed in the following section.

3.2 Mobile measurements of methane plumes

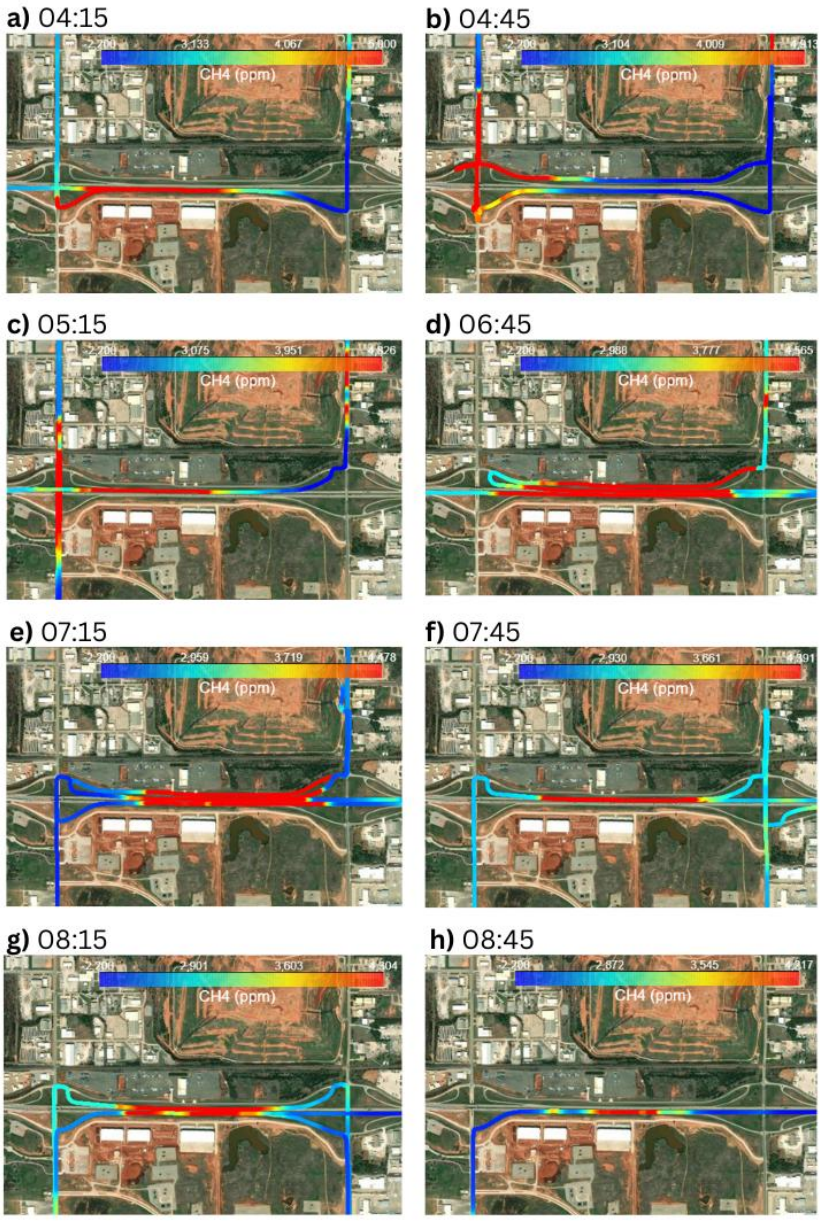


Figure 3.5. Mobile CH_4 concentrations (ppm) recorded along the Interstate 240 transect south of the Oklahoma City landfill site during early morning measurement intervals on December 13th, 2025, including: (a) 04:15, (b) 04:45, (c) 05:15, (d) 06:45, (e) 07:15, (f) 07:45, (g) 08:15, and (h) 08:45 (CST).

Mobile measurements during the early morning hours (roughly 04:15–08:45 CST) revealed elevated CH_4 concentrations along the Interstate 240 transect downwind of the landfill (Fig. 3.5). The highest concentrations, exceeding 4.8 ppm in several subplots, were observed in the earliest measurement intervals (04:15–05:15 CST), with a narrower plume appearing southwest of the landfill (Fig. 3.5a–c). This is consistent with the shallow, stable nocturnal boundary layer that typically prevails in the early morning hours, which suppresses vertical mixing and allows CH_4 to accumulate near the surface (X.-M. Hu et al., 2025; Lapworth, 2006). As the morning progressed into the 07:45–08:45 CST period, peak concentrations began to decrease modestly (Fig. 3.5f–h). However, elevated CH_4 measurements around 4.3 ppm persisted along the transect, suggesting the boundary layer had not yet grown sufficiently to substantially diminish the landfill plume. In fact, the plume appeared wider at times and shifted to be more south–southwest of the landfill with the highest values concentrated near the center of the transect.

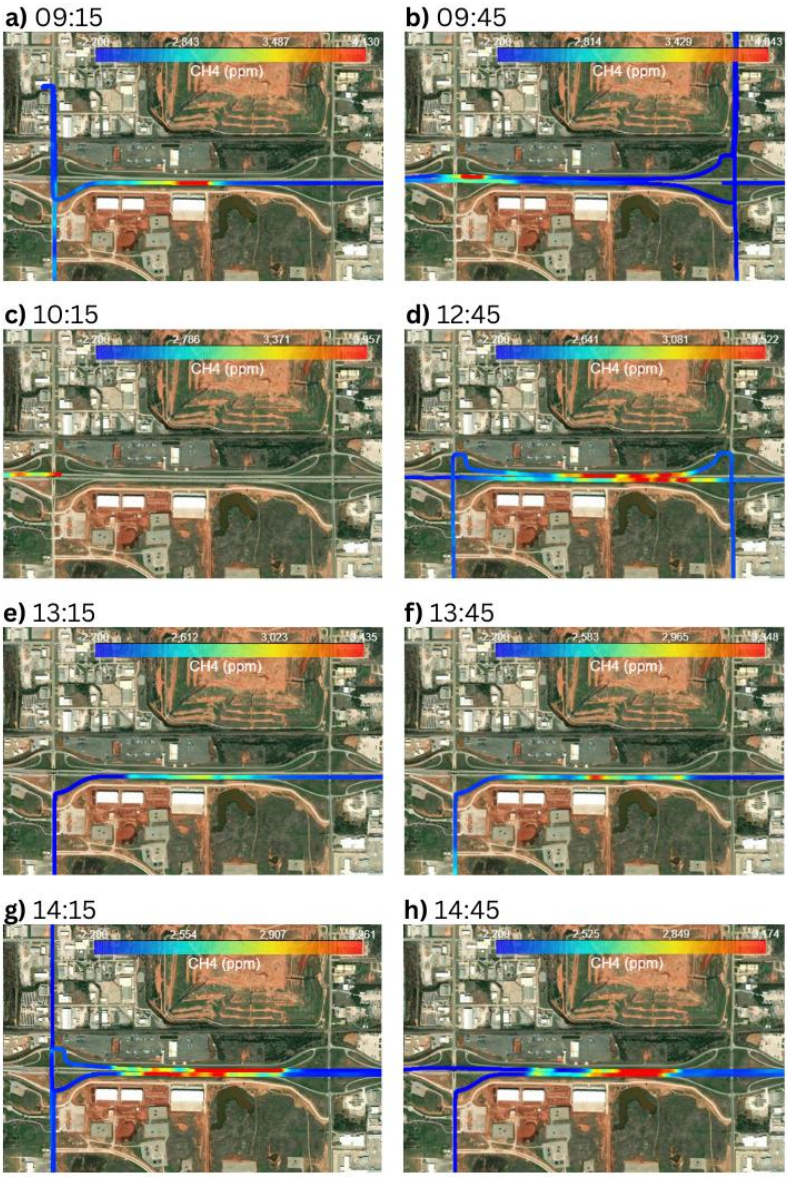


Figure 3.6. Mobile CH_4 concentrations (ppm) recorded along the Interstate 240 transect south of the Oklahoma City landfill site during late morning to afternoon measurement intervals on December 13th, 2025, including: (a) 09:15, (b) 09:45, (c) 10:15, (d) 12:45, (e) 13:15, (f) 13:45, (g) 14:15, and (h) 14:45 (CST).

During the late morning and afternoon hours (around 09:15–14:45 CST), CH_4 enhancements along the Interstate 240 transect were noticeably reduced compared to the early morning period (Fig. 3.6). Peak concentrations dropped to roughly 3.1–3.5 ppm across most

subplots, with a more broad and weaker plume signal. This change can be attributed to the growth of the boundary layer and surface heating, which increased vertical mixing and dispersed the landfill plume (Darbieu et al., 2015; Grimsdell & Angevine, 2002). Some variability is present across the afternoon subplots, such as the 12:45 and 14:15 CST intervals, which showed locally elevated concentrations along portions of the transect (Fig. 3.6l and o). This is likely reflecting fluctuations in emission strength or shifting wind directions that temporarily redirected the plume. Overall, the contrast between the early morning and afternoon results highlights the strong influence of boundary layer dynamics on near-surface CH_4 concentrations.

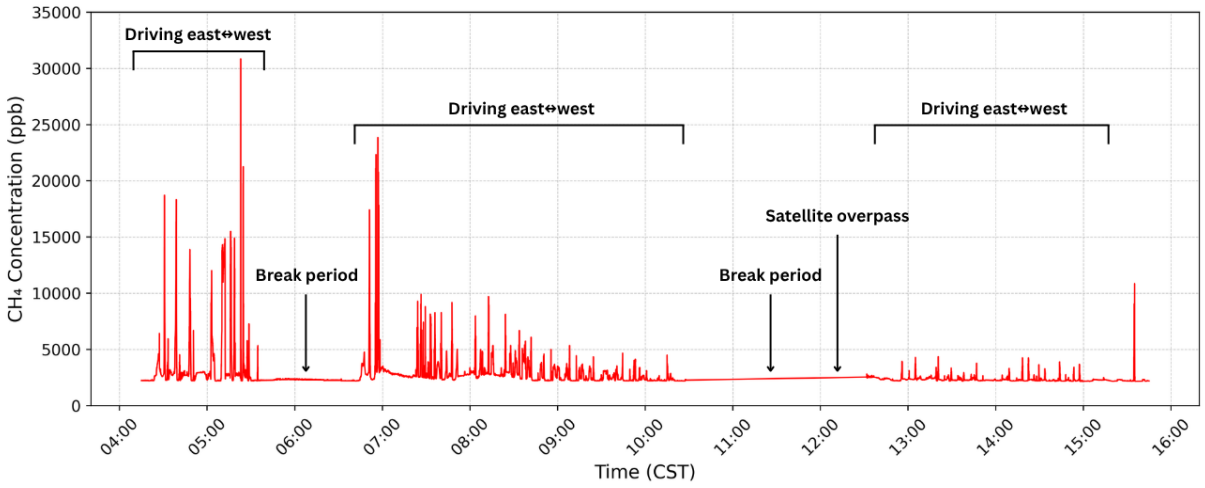


Figure 3.7. Time series of near-surface CH_4 concentrations (ppb) from mobile measurements around the Oklahoma City landfill site on December 13th, 2025, derived from LI-COR 7810 and GPS data in local time (CST).

The time series of mobile CH_4 concentrations throughout the measurement day revealed a clear morning-to-afternoon transition driven largely by boundary layer dynamics (Fig. 3.7). The highest concentrations of the day occurred during the first active measurement period (roughly 04:15–05:30 CST), where peaks exceeding 15,000–30,000 ppb were observed. These peaks occurred when the vehicle crossed the landfill plume along the east-west transect under a shallow

and stable boundary layer. A second measurement block began around 06:45 CST following a break period, with an initial peak exceeding 20,000 ppb before concentrations declined steadily through the morning hours as the boundary layer grew. By the third active measurement period (approximately 13:00–15:00 CST) peak concentrations were substantially lower, generally remaining below 5,000 ppb due to the well-mixed afternoon boundary layer. Between each plume crossing, concentrations dropped back toward background levels of roughly 2,000–2,500 ppb, which was close to the global average atmospheric CH_4 concentration of approximately 1,900 ppb (Lan et al., 2021; Skeie et al., 2023). The two annotated break periods (when the mobile measurement team rested) showed consistent near-background concentrations, confirming that the sharp peaks occurred due to driving through the landfill plume. Overall, the time series illustrated that the landfill was a persistent CH_4 source throughout the day, but that concentrations were greatly impacted by the evolution of the boundary layer.

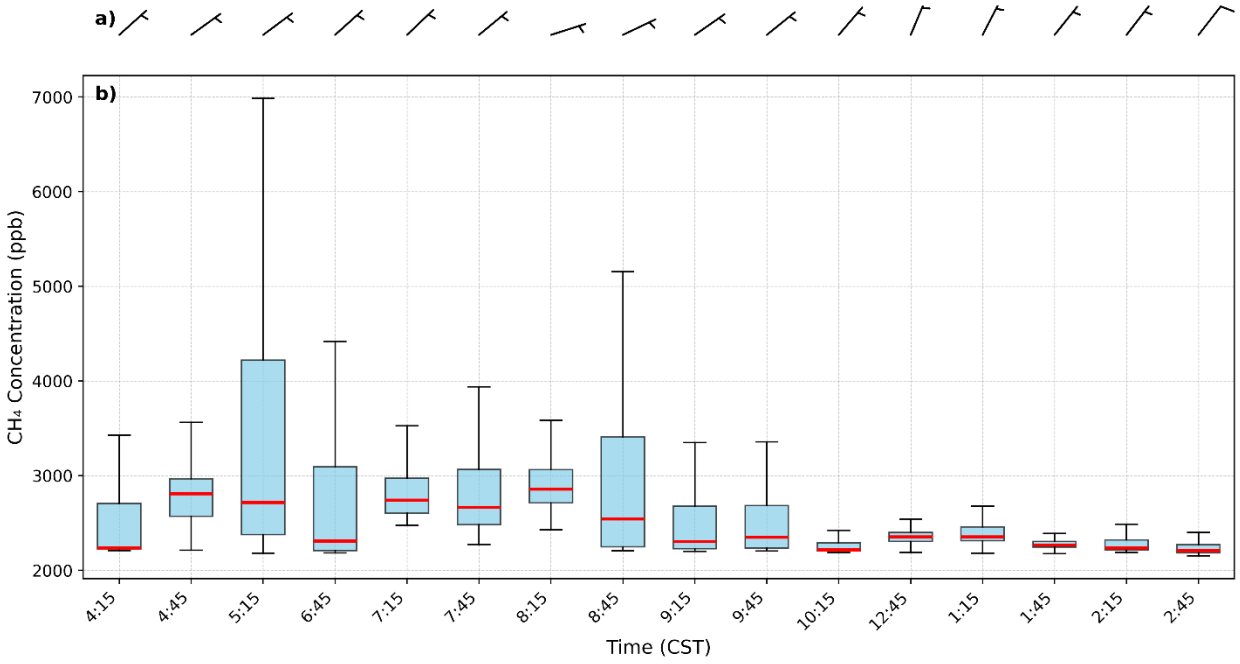


Figure 3.8. Distribution of (b) mobile CH_4 concentrations (ppb) and (a) WRF-Chem simulated mean surface winds (where half-barb = 2.5 m s^{-1}, full = 5 m s^{-1}, flag = 25 m s^{-1}) at the Oklahoma City landfill site during active 30-minute measurement intervals on December 13th, 2025.

Figure 3.8 depicts the distribution of mobile CH_4 concentrations across each active 30-m measurement interval alongside WRF-Chem simulated mean surface winds. The widest interquartile ranges and highest upper whiskers mainly occurred in the early morning, specifically at 05:15 and 08:45 CST (Fig. 3.8). These large variations in CH_4 concentrations were due to the vehicle repeatedly crossing in and out of the concentrated landfill plume. The median concentrations during the early morning intervals were significantly higher than the background, with some intervals showing medians near 2,800 ppb. From 10:15 CST onward, both the medians and spreads decreased substantially as most boxplots only ranged between roughly 2,200–2,500 ppb. Again, this transition aligned with the well-mixed boundary layer timing that reduced the contrast between plume and background concentrations. Surface winds from WRF-Chem were northeasterly throughout the morning, veering slightly more northerly in the afternoon. Wind speeds remained light and only modestly increased heading into the afternoon hours. The consistent winds explain why the plume was mainly advected southward and southwestward across the Interstate 240 transect (Pérez et al., 2021). This suggests that morning and afternoon CH_4 concentration differences were primarily driven by boundary layer depth rather than changes in wind direction or landfill emission strength.

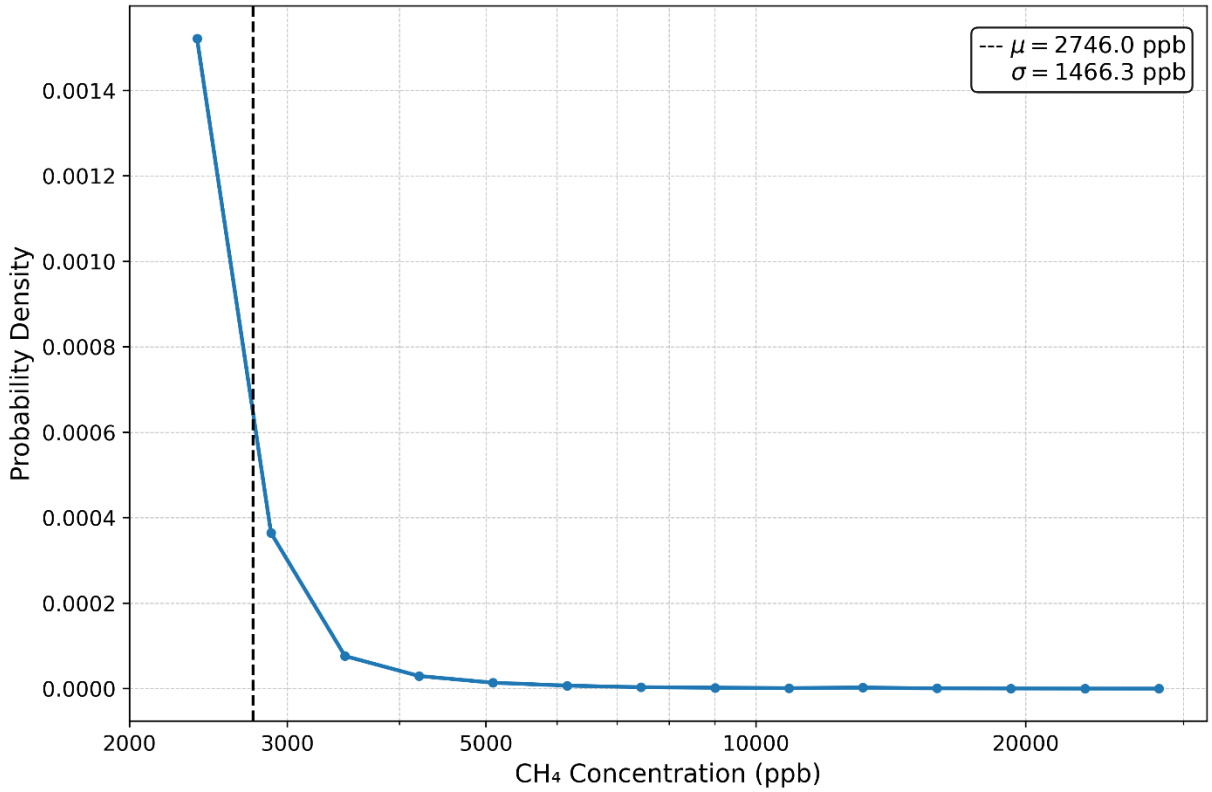


Figure 3.9. Probability density distribution of near-surface CH_4 concentrations (ppb) from mobile measurements on December 13th, 2025, at the Oklahoma City landfill site.

The probability density distribution of all mobile CH_4 measurements is strongly right-skewed, with the vast majority of observations occurring at relatively low concentrations and probability density dropping sharply as concentrations increase (Fig. 3.9). The mean value of 2746 ppb lies to the right of the peak, indicating the influence of intermittent plume encounters during transect crossings on the overall distribution. The long tail extending toward 30,000 ppb reflects infrequent but significant enhancements associated with entering the landfill plume. These findings are consistent with the sporadic nature of mobile landfill CH_4 measurements documented in previous studies (Kumar et al., 2024; Mønster et al., 2019). This skewed distribution is typical of near-source trace gas measurements, where background conditions dominate and brief high concentrations greatly impact emission rate estimates.

3.3 Satellite observations of methane emissions

The Tanager-1 satellite captured a clear CH_4 plume over the Republic Services Southeast Landfill during its overpass at 18:10:12 UTC (12:10:12 CST) on December 13th, 2025 (Fig. 3.10). The highest column enhancements of 1,500–2,000 ppm·m were concentrated directly over and immediately south of the landfill, consistent with the generally northerly winds transporting the plume southward during this time. The broader visualization plume extended well south of the landfill and reached beyond Interstate 240, spanning roughly 0.02 degrees of latitude (approximately 2 km).

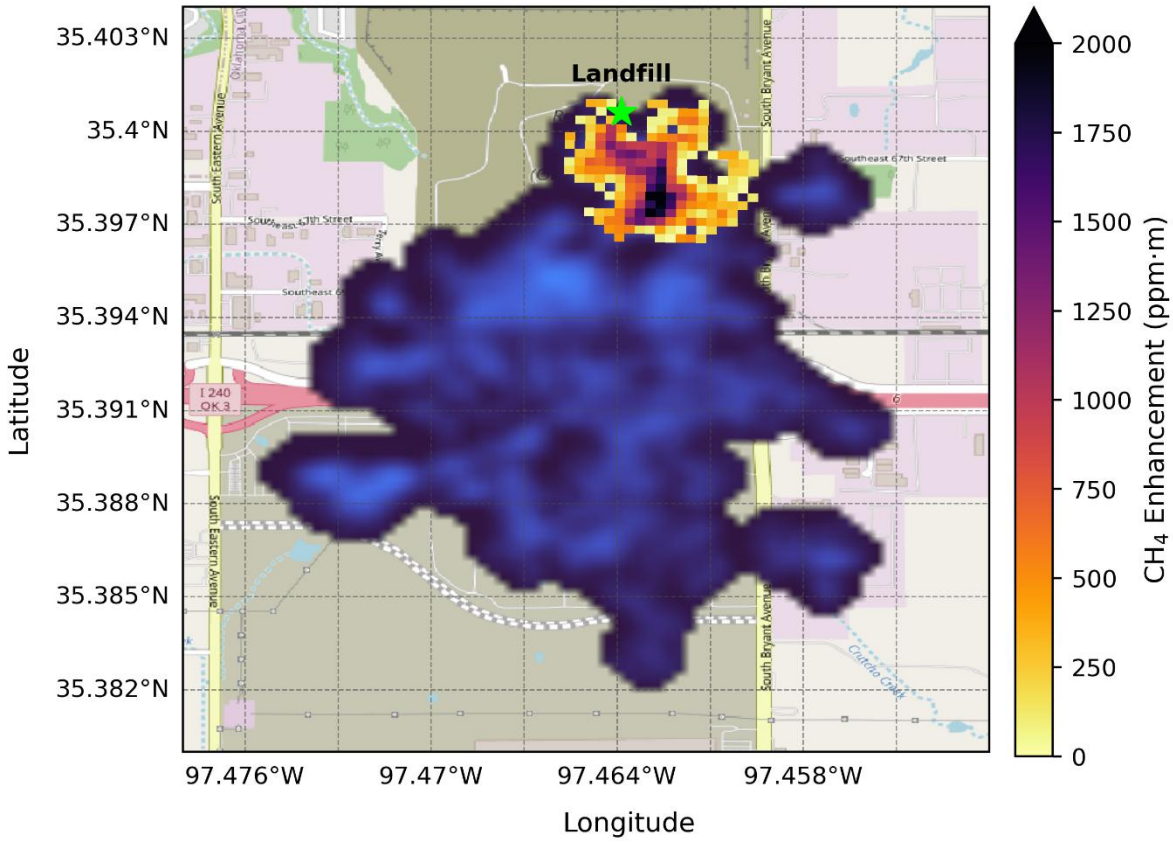


Figure 3.10. Tanager-1 satellite-retrieved column CH_4 enhancement (ppm·m) over the Oklahoma City landfill site during the Carbon Mapper overpass at 18:10:12 UTC on December 13th, 2025. This includes the visualization plume (blue-purple shading) and Integrated Mass Enhancement plume mask (yellow-purple shading).

The IME plume mask (shown in yellow to purple) shows the core of the CH_4 emission source and represents the pixels Carbon Mapper used to quantify the emission rate. The mask is tightly constrained to the landfill site, reflecting the automated segmentation algorithm that groups together nearby pixels with concentrations above a dynamic threshold within 2,500 m of the plume origin (Carbon Mapper, 2024). The highest enhancements offset slightly to the south of the landfill center were due to the northerly flow, which was also demonstrated by the mobile measurements. The broader visualization plume beyond the IME mask boundary reflected lower CH_4 enhancements that fell below the dynamic threshold but were still detectable above the background concentration. This plume extended across the Interstate 240 transect, consistent with the mobile measurement findings. This illustrates the high sensitivity and 30 m resolution of the Tanager-1 satellite (Carbon Mapper, 2025; Jacob et al., 2022).

Table 3.2. Carbon Mapper Tanager-1 satellite overpass metadata for the detected CH_4 plume at the Oklahoma City landfill site on December 13th, 2025.

Date/Time	Plume Latitude	Plume Longitude	IPCC Sector	Plume Bounds	Emission	Emission Uncertainty	Wind Speed	Wind Direction
2025-12-13 18:10:12 UTC	35.399	-97.463	Solid Waste (6A)	[-97.485, 35.376, -97.446, 35.407]	928.07	359.00	2.24 ± 0.80	25.99 ± 5.55

The metadata table reported a CH_4 emission rate of 928.07 kg CH_4 hr^{-1} with an uncertainty of 359.00 kg CH_4 hr^{-1} for this landfill overpass (Table 3.2). The wind speed used in

the IME calculation was 2.24 ± 0.80 m s^{-1} from a direction of 25.99 ± 5.55°, sourced from the HRRR reanalysis product, consistent with the northerly to northeasterly winds observed throughout December 13. The reported uncertainty reflects the combined contributions of wind speed uncertainty and retrieval noise, which are the dominant sources of error in IME-based emission quantification (Carbon Mapper, 2024).

3.4 Simulated methane enhancements

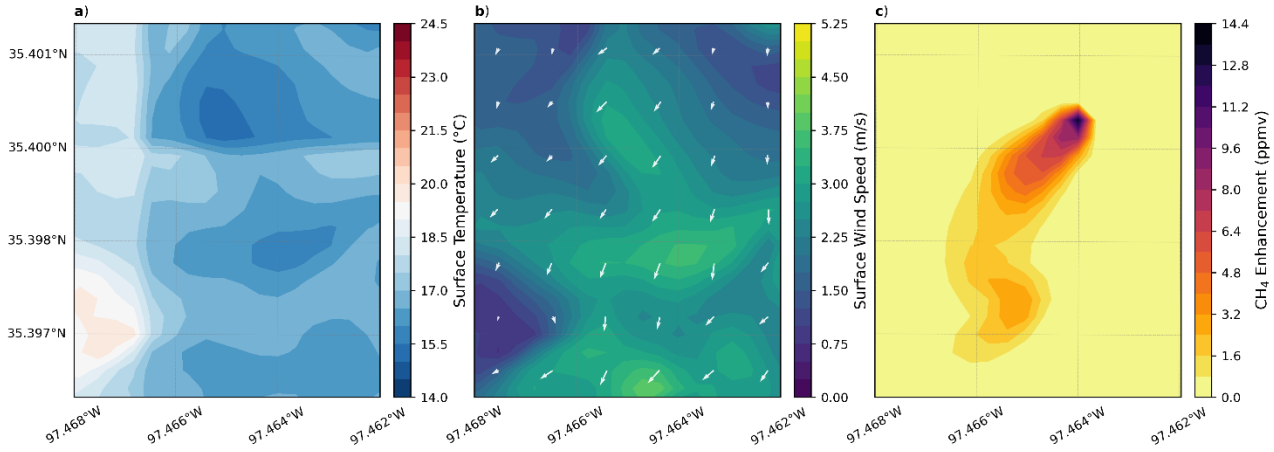


Figure 3.11. WRF-Chem simulated (a) surface temperature (°C), (b) surface wind speed and direction (m s^{-1}), and (c) CH_4 enhancement (ppmv) at 19:00 UTC around the Oklahoma City landfill site on December 13th, 2025.

Figure 3.11 demonstrates the WRF-Chem simulated temperatures, wind field, and unscaled CH_4 enhancement around the landfill at 19:00 UTC (13:00 CST). Surface temperatures (Fig. 3.11a) are generally cool across the domain, ranging from roughly 15 to 24°C, with slightly warmer patches southwest of the landfill. This is likely due to differences in surface albedo and thermal properties between the landfill cover and surrounding area. The simulated wind field (Fig. 3.11b) shows light surface winds of around 1–3 m s^{-1} with a northerly to northeasterly direction, consistent with the observed winds throughout December 13th and supporting

southward plume transport away from the landfill. The unscaled CH_4 enhancement plume (Fig. 3.11c) originates from the landfill and extends southwestward, with peak enhancements reaching approximately 12–14 ppmv at the site and immediately downwind before dispersing with distance. This enhancement is calculated by subtracting the background CH_4 from the total anthropogenic CH_4 values, where the background is derived from the lateral boundary conditions of the model. The plume exhibits a slight curvature toward the southwest, which aligns with the wind vectors variability. These simulated patterns show overall good agreement with the mobile observations.

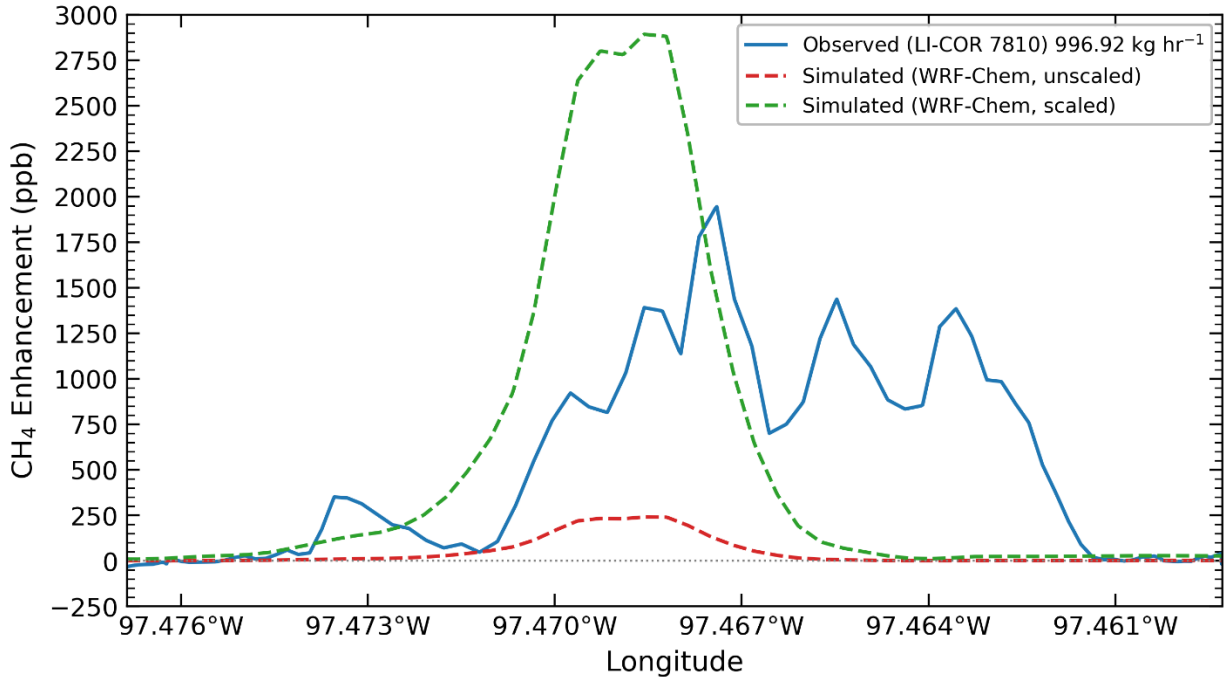


Figure 3.12. Observed vs simulated CH_4 enhancement (ppb) at 19:00 UTC around the Oklahoma City landfill site on December 13th, 2025.

Figure 3.12 compares the observed and simulated cross-plume CH_4 enhancements along the Interstate 240 transect at 19:00 UTC. The observed profile (blue line) shows a broad enhancement spanning from roughly 97.473°W to 97.461°W, with multiple peaks reaching up to

nearly 2,000 ppb and a mobile-derived emission rate of 996.92 kg CH_4 hr^{-1} (Fig. 3.12). The unscaled WRF-Chem simulation profile (red dashed line) captures the general location of the plume, peaking near 97.468°W. However, it underestimates the magnitude of enhancements, with a maximum of only around 250 ppb. This underestimation is consistent with findings from other WRF studies, where discrepancies between simulated and observed CH_4 enhancements are attributed to biases in prescribed emission inventories rather than errors in the model's representation of transport and dispersion (Callewaert et al., 2023, 2025). Despite the magnitude difference, the good spatial alignment between the two profiles suggests WRF-Chem reproduced the plume location and general shape reasonably well given the northerly wind conditions on this day. Also shown is the scaled WRF-Chem CH_4 enhancement profile (green dashed line), which exceeds the observed peak and reflects the structural differences in plume shape where WRF-Chem produces a narrow, concentration enhancement instead of the broader and more dispersed observed profile, likely due to difficulties capturing turbulent mixing at this model resolution.

To inversely estimate the landfill CH_4 emission rate, a scaling ratio was derived from the observed and simulated cross-plume profiles shown in Figure 3.12. The ratio $R = \Delta CH_4obs / \Delta CH_4sim$ was calculated by comparing the peak observed and simulated enhancements along the Interstate 240 transect, yielding R = 9.962. Multiplying this ratio by the prescribed WRF-Chem emission rate of 100 kg CH_4 hr^{-1} produces an emission rate of 996.92 kg CH_4 hr^{-1}. This approach follows the ratio method used in other studies, which uses the model's representation of atmospheric transport and dispersion to estimate the real emission rate from the observed CH_4 (X.-M. Hu et al., 2025; Ye et al., 2020).

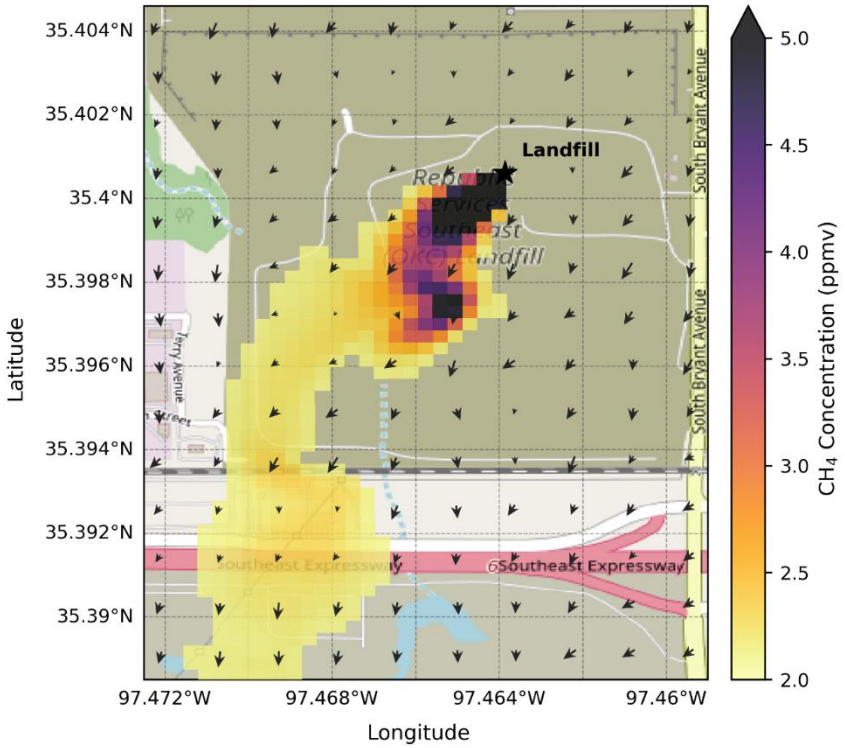


Figure 3.13. Observation to simulation scaling of WRF-Chem near-surface CH_4 concentration (ppmv) with surface wind vectors at 19:00 UTC around the Oklahoma City landfill site on December 13th, 2025. Note that background concentrations below 2 ppmv are shown as transparent for visualization purposes.

The scaled WRF-Chem CH_4 concentration field (Fig. 3.13) shows a well-defined plume originating at the landfill and extending southwestward, with peak near-surface concentrations reaching approximately 4.5–5.0 ppmv immediately downwind of the source. The plume disperses rapidly with distance, with concentrations approaching background values of around 2 ppmv within roughly 0.5–1 km southwest of the landfill. Surface wind vectors confirm consistent northerly to northeasterly flow across the domain, directing the plume toward Interstate 240 in good agreement with the mobile observations. The spatial compactness of the CH_4 plume reflects the light wind conditions on December 13th, which limited dispersion and concentrated the emission signal close to the landfill.

3.5 Integrating observations and simulations for methane emission estimation

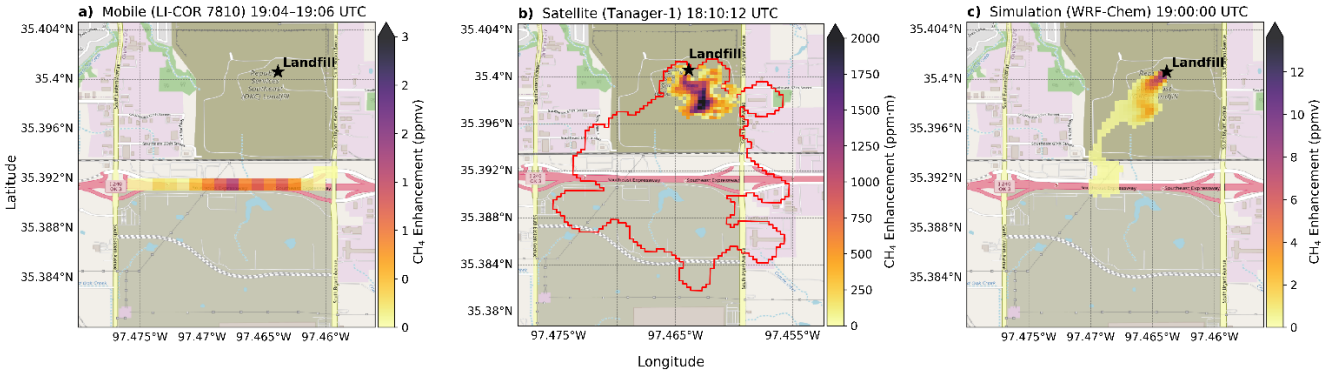


Figure 3.14. Spatial distribution of CH_4 enhancements around the Oklahoma City landfill site on December 13th, 2025, as captured by (a) LI-COR 7810 mobile measurements from 19:04–19:06 UTC, (b) Tanager-1 satellite overpass at 18:10:12 UTC, and (c) WRF-Chem model simulation at 19:00:00 UTC.

Figure 3.14 places all three CH_4 enhancement estimates side by side, allowing a direct spatial comparison despite the differences in measurement time and units. All three panels consistently show the landfill as the dominant CH_4 source, with enhancements extending generally southward across Interstate 240. The mobile panel (Fig. 3.14a) captures a narrow band of enhancements along the transect with peak values around 2.5–3 ppmv during the 19:04–19:06 UTC window. The satellite panel (Fig. 3.14b) shows the IME plume tightly clustered over the landfill with column enhancements up to roughly 2,000 ppm·m, and the broader red-outlined visualization plume reaching well beyond Interstate 240 at the overpass time of 18:10:12 UTC. The WRF-Chem panel (Fig. 3.14c) depicts a southwestward plume orientation, with the highest CH_4 enhancements of approximately 12–14 ppmv located just downwind of the landfill before dispersing toward the transect.

Despite these broad spatial agreements, there are notable differences between the three approaches that are not just due to the timing offset. The mobile measurements show detailed, fine-scale changes in CH_4 along a single east–west transect, capturing spatial variability that fixed stations cannot resolve (Mønster et al., 2019). The satellite measures CH_4 over the full atmospheric column, meaning its ppm·m units are not directly comparable to near-surface ppmv values, and its 30 m resolution still smooths smaller-scale features (Jacob et al., 2022; Palmer et al., 2021). WRF-Chem reproduces the general plume location well, but shows a smoother CH_4 enhancement pattern than the mobile data due to the averaging effect of turbulent mixing parameterizations at LES scales noted in similar studies (X.-M. Hu et al., 2025). In summary, these approaches provide complementary views of the same CH_4 plume, with the mobile data capturing fine-scale near-surface variability, the satellite depicts broader spatial patterns above the surface, and WRF-Chem provides continuous spatial and temporal coverage that connects the two (Cusworth et al., 2020).

Table 3.3: Summary of key measurement characteristics from mobile, satellite, and simulated approaches at the Oklahoma City landfill site on December 13th, 2025.

	Mobile	**Satellite**	**Simulation**
Instrument/ Platform	LI-COR 7810	Tanager-1	WRF-Chem
Observation time (UTC)	19:04–19:06	18:10:12	19:00:00
Wind source	WRF-Chem	HRRR	WRF-Chem
Wind speed (m s^{-1})	~2–3	2.24±0.8	~2–3
Emission rate method	Obs/sim scaling ratio, R	IME	Q_{sim}×R
Emission rate (kg CH_4 hr^{-1})	996.92	928.07	996.92 (used mobile data to derive R)

The mobile-derived and satellite-derived emission rate estimates show reasonable agreement, differing by only roughly 7% with values of 996.92 and 928.07 kg CH_4 hr^{-1} respectively (Table 3.3). The slight differences are likely due to the fact that both estimates rely on independent measurements, different CH_4 quantities (near-surface concentration versus column-integrated enhancement), and different wind sources. The mobile estimate used WRF-Chem simulated winds of approximately 2–3 m s^{-1}, while the satellite IME method used HRRR-derived winds of 2.24 ± 0.80 m s^{-1}. The similar wind speeds likely contributes to the close agreement in emission rates since wind speed is one of the dominant sources of uncertainty in both the IME and scaling ratio approaches (Carbon Mapper, 2024; Mønster et al., 2019). The roughly 7% difference could also reflect the timing offset between the mobile transect (19:04–19:06 UTC) and the satellite overpass (18:10:12 UTC), during which wind conditions or emission strength may have varied slightly. Overall, the agreement between the different approaches suggests that both methods provide reliable estimates of landfill CH_4 emissions, and is consistent with previous studies showing consistency between mobile and satellite estimates when wind conditions are well known (Cusworth et al., 2020; Jacob et al., 2022).

Chapter 4

Conclusions

4.1 Key findings on urban compound heat and $PM_{2.5}$ pollution episodes

Chapter 2 provides a comprehensive assessment of heat waves, $PM_{2.5}$ pollution episodes, and compound heat and $PM_{2.5}$ pollution events across CONUS urban and rural areas from 2000 to 2022 (23 years) using reconstructed, long-term, high-resolution datasets. In particular, heat waves were defined based on daily minimum near-surface air temperature (rather than remotely sensed land surface temperature commonly used in long-term studies). Results show that urban environments generally experienced more frequent, longer lasting, and more intense heat waves than rural surroundings, primarily due to the persistent nighttime urban heat island effect. Similarly, $PM_{2.5}$ pollution episodes were more frequent, prolonged, and intense in most urban areas, largely driven by higher pollution emissions from transportation, industry, and other urban sources. Compound heat and $PM_{2.5}$ pollution episodes were more frequent and intense in ~98% of CONUS urban areas, and more than half of them experienced longer durations than their rural counterparts. On average, urban areas experienced 1.4°C greater cumulative heat intensity and 6.0 μg m^{-3} higher cumulative $PM_{2.5}$ pollution intensity per year than their rural surroundings. Furthermore, the spatial patterns of compound events aligned closely with those of $PM_{2.5}$ pollution episodes, suggesting that air pollution played a dominant role in their occurrence. Notably, the number of $PM_{2.5}$ pollution and compound event days declined through ~2016 but increased in the western U.S. in recent years, primarily due to rising wildfire emissions. It is worth noting that while the equal-area rural buffer approach is widely used in urban climate research to ensure spatial comparability across cities of varying sizes, the rural boundaries are

defined solely by matching the area of each urban shapefile rather than by any physical, meteorological, or pollution-based criterion. Additionally, the reliability of $PM_{2.5}$ estimates toward the end of the study period may be reduced, as ground-based monitoring data used to train and validate the machine learning models becomes less available after 2019, which should be considered when interpreting recent trends in $PM_{2.5}$ pollution and compound events.

4.2 Key findings on urban methane emissions and observational constraints

Chapter 3 presents a multiscale characterization of CH_4 emissions from the Republic Services Southeast Landfill in Oklahoma City using concurrent mobile and satellite observations collected on December 13th, 2025, alongside WRF-Chem simulations. Mobile measurements revealed a pronounced morning-to-afternoon transition in near-surface CH_4 concentrations, with early morning peaks exceeding 30,000 ppb under a shallow stable boundary layer that substantially decreased in the afternoon as the boundary layer grew and vertical mixing increased. The landfill was a persistent CH_4 source throughout the day, with its plume extending south-southwestward toward Interstate 240 under light northeasterly winds. The Tanager-1 satellite captured a well-defined CH_4 plume at 18:10:12 UTC with peak column enhancements of 1,500–2,000 ppm·m over the landfill, resulting in a satellite-derived emission rate of 928.07 ± 359.00 kg CH_4 hr^{-1}. WRF-Chem reproduced the plume location and southwestward transport direction well, and the ratio of observed to simulated cross-plume CH_4 enhancements was used to inversely estimate a landfill emission rate of 996.92 kg CH_4 hr^{-1}. Despite differences in measurement approach, spatial coverage, and wind data sources, the close agreement (only roughly 7% difference) between mobile and satellite estimates shows the benefit of combining

multiscale observations with high-resolution simulations to better estimate landfill CH_4 emissions.

4.3 Implications and future work

The findings of the compound heat and $PM_{2.5}$ pollution episode analysis underscores the pressing need to address urban heat and particulate matter pollution issues simultaneously to reduce human exposure, especially in cities and regions with the most severe impacts. The urban and regional hotspots for extreme heat and $PM_{2.5}$ pollution identified in this study can help prioritize future physics-based numerical simulations to disentangle key contributors and interactions between these environmental stressors. Investigating the meteorological and anthropogenic drivers of the observed urban–rural differences and evaluating the effectiveness of various mitigation strategies will help inform targeted interventions and investments. Future mitigation efforts should also focus on cities where these stressors pose the greatest risks, to improve urban resilience, public health, and environmental sustainability in an increasingly warming and urbanizing world.

The results from the landfill emission case study highlight the value of integrating concurrent mobile measurements, satellite observations, and process-based modeling to estimate landfill CH_4 emissions. The ratio of observed to simulated CH_4 enhancements along the mobile transect yielded a scaling factor of 9.962, which was applied to the prescribed emission rate to estimate the actual landfill emission rate. Building on this work, our ongoing concurrent measurement campaigns (see Figure A9 in Appendix) demonstrate that emission rate estimates derived from the scaled WRF-Chem results remain consistent with satellite observations, which provides increasing confidence in the methodology. Our continued mobile measurements also

create an opportunity to investigate seasonal variability in emissions and to better understand the influence of temperature, moisture, and operational factors on CH_4 production. Future work should extend these mobile measurements across a wider range of meteorological conditions, including different wind regimes and boundary layer conditions, to further reduce uncertainty scaling approaches. Expanding the observational network through more frequent satellite overpasses and additional ground-based sensors would also enhance the ability to capture temporal variability in emissions. At the same time, improving model representations of landfill processes and refining prescribed emission inputs will be critical for reducing uncertainty in inversely estimated emission rates. More broadly, the multiscale approach demonstrated here could be applied to other types of waste sites in different climates to improve emission estimates and support more effective CH_4 mitigation efforts.

From a policy perspective, these findings highlight the need for integrated strategies that address both urban air pollution exposure and underlying emission sources. At the large scale, the spatial patterns of compound heat and $PM_{2.5}$ events across CONUS cities show the need for national and regional policy frameworks that account for the co-occurrence of these hazards rather than extreme heat or $PM_{2.5}$ episodes alone. Policies that aim to reduce $PM_{2.5}$ pollution from transportation and wildfire management will have the greatest co-benefits for reducing compound event frequency, particularly across the western U.S. where wildfires occur most often. Within-cities, the landfill CH_4 results demonstrate the importance of site-level emission monitoring and reporting. Current facility self-reporting to the EPA Greenhouse Gas Reporting Program may substantially underestimate actual emissions at landfill sites. Requiring more frequent and independent verification of landfill emissions through mobile or satellite-based measurements could improve the accuracy of national inventories and help identify facilities

where gas collection systems are underperforming. Taken together, both chapters suggest that effective urban air quality policy needs to operate at multiple scales, combining broad regulations with targeted, site-specific interventions informed by observations.

Overall, this thesis illustrates that urban air quality is a multiscale problem that cannot be fully understood from a single perspective. Chapter 2 demonstrates that urban areas can intensify the health risks of compound heat and $PM_{2.5}$ pollution events at large scales, while Chapter 3 shows that urban areas also contain high emission sources like landfills that affect both local air quality and global greenhouse gas levels. Reducing urban air quality risks therefore requires both managing large-scale environmental stressors and accurately quantifying local emission sources. By integrating observations and models across scales, this work contributes to a more comprehensive understanding of urban air quality and provides a foundation for developing more effective, data-informed mitigation and adaptation strategies in a changing climate.

References

Analitis, A., Michelozzi, P., D'Ippoliti, D., de'Donato, F., Menne, B., Matthies, F., Atkinson, R. W., Iñiguez, C., Basagaña, X., Schneider, A., Lefranc, A., Paldy, A., Bisanti, L., & Katsouyanni, K. (2014). Effects of heat waves on mortality: Effect modification and confounding by air pollutants. *Epidemiology*, *25*(1), 15–22. https://doi.org/10.1097/EDE.0b013e31828ac01b

Anderson, G. B., & Bell, M. L. (2011). Heat waves in the United States: Mortality risk during heat waves and effect modification by heat wave characteristics in 43 US communities. *Environmental Health Perspectives*, *119*(2), 210–218. https://doi.org/10.1289/ehp.1002313

Balch, J. K., Bradley, B. A., Abatzoglou, J. T., Nagy, R. C., Fusco, E. J., & Mahood, A. L. (2017). Human-started wildfires expand the fire niche across the United States. *Proceedings of the National Academy of Sciences of the United States of America*, *114*(11), 2946–2951. https://doi.org/10.1073/pnas.1617394114

Barriopedro, D., García-Herrera, R., Ordóñez, C., Miralles, D. G., & Salcedo-Sanz, S. (2023). Heat waves: Physical understanding and scientific challenges. *Reviews of Geophysics*, *61*(2), e2022RG000780. https://doi.org/10.1029/2022RG000780

Bauer, S. E., Tsigaridis, K., & Miller, R. (2016). Significant atmospheric aerosol pollution caused by world food cultivation. *Geophysical Research Letters*, *43*(10), 5394–5400. https://doi.org/10.1002/2016GL068354

Bell, M. L., Dominici, F., Ebisu, K., Zeger, S. L., & Samet, J. M. (2007). Spatial and temporal variation in $PM_{2.5}$ chemical composition in the United States for health effects studies. *Environmental Health Perspectives*, 989–995. https://doi.org/10.1289/ehp.9621

Boisramé, G. F. S., Brown, T. J., & Bachelet, D. M. (2022). Trends in western USA fire fuels using historical data and modeling. *Fire Ecology*, *18*, 8. https://doi.org/10.1186/s42408-022-00129-4

Börjesson, G., & Svensson, B. H. (1997). Seasonal and Diurnal Methane Emissions From a Landfill and Their Regulation By Methane Oxidation. *Waste Management & Research*, *15*(1), 33–54. https://doi.org/10.1177/0734242X9701500104

Buchwitz, M., de Beek, R., Burrows, J. P., Bovensmann, H., Warneke, T., Notholt, J., Meirink, J. F., Goede, A. P. H., Bergamaschi, P., Körner, S., Heimann, M., & Schulz, A. (2005). Atmospheric methane and carbon dioxide from SCIAMACHY satellite data: Initial comparison with chemistry and transport models. *Atmospheric Chemistry and Physics*, *5*(4), 941–962. https://doi.org/10.5194/acp-5-941-2005

Burke, M., Childs, M. L., de la Cuesta, B., Qiu, M., Li, J., Gould, C. F., Heft-Neal, S., & Wara, M. (2023). The contribution of wildfire to $PM_{2.5}$ trends in the USA. *Nature*, *622*(7984), 761–766. https://doi.org/10.1038/s41586-023-06522-6

Callewaert, S., Zhou, M., Langerock, B., Wang, P., Wang, T., Mahieu, E., & De Mazière, M. (2023). A WRF-Chem study on the variability of CO_2, CH_4 and CO concentrations at Xianghe, China supported by ground-based observations and TROPOMI. *EGUsphere*, 1–37. https://doi.org/10.5194/egusphere-2023-2103

Callewaert, S., Zhou, M., Langerock, B., Wang, P., Wang, T., Mahieu, E., & De Mazière, M. (2025). A WRF-Chem study of the greenhouse gas column and in situ surface concentrations observed in Xianghe, China – Part 1: Methane (CH_4). *Atmospheric Chemistry and Physics*, *25*(16), 9519–9544. https://doi.org/10.5194/acp-25-9519-2025

Cambaliza, M. O. L., Bogner, J. E., Green, R. B., Shepson, P. B., Harvey, T. A., Spokas, K. A., Stirm, B. H., & Corcoran, M. (2017). Field measurements and modeling to resolve m2 to km2 CH4 emissions for a complex urban source: An Indiana landfill study. *Elementa: Science of the Anthropocene*, *5*, 36. https://doi.org/10.1525/elementa.145

Cannon, A. J., Sobie, S. R., & Murdock, T. Q. (2015). Bias correction of GCM precipitation by quantile mapping: How well do methods preserve changes in quantiles and extremes? *Journal of Climate*, *28*(17), 6938–6959. https://doi.org/10.1175/JCLI-D-14-00754.1

Carbon Mapper. (2024). *Methane and Carbon Dioxide Emission Quantification for Satellites* [Algorithm Theoretical Basis Document]. Carbon Mapper. https://assets.carbonmapper.org/documents/L3_L4%20Algorithm%20Theoretical%20Basis%20Document_formatted_10-24-24.pdf

Carbon Mapper. (2025, February 14). *Product Guide: Data Definition & Specification*. Carbon Mapper. https://carbonmapper.org/articles/product-guide

Chakraborty, J., Collins, T. W., Grineski, S. E., & Aun, J. J. (2022). Air pollution exposure disparities in US public housing developments. *Scientific Reports*, *12*, 9887. https://doi.org/10.1038/s41598-022-13942-3

Chanton, J., & Liptay, K. (2000). Seasonal variation in methane oxidation in a landfill cover soil as determined by an in situ stable isotope technique. *Global Biogeochemical Cycles*, *14*(1), 51–60. https://doi.org/10.1029/1999GB900087

Chen, K., Boomsma, J., & Holmes, H. A. (2023). A multiscale analysis of heatwaves and urban heat islands in the western U.S. during the summer of 2021. *Scientific Reports*, *13*, 9570. https://doi.org/10.1038/s41598-023-35621-7

Cheval, S., Amihăesei, V.-A., Chitu, Z., Dumitrescu, A., Falcescu, V., Irașoc, A., Micu, D. M., Mihulet, E., Ontel, I., Paraschiv, M.-G., & Tudose, N. C. (2024). A systematic review of urban heat island and heat waves research (1991–2022). *Climate Risk Management*, *44*, 100603. https://doi.org/10.1016/j.crm.2024.100603

Chow, J. C., Chen, L.-W. A., Watson, J. G., Lowenthal, D. H., Magliano, K. A., Turkiewicz, K., & Lehrman, D. E. (2006). $PM_{2.5}$ chemical composition and spatiotemporal variability during the California Regional PM_{10}/$PM_{2.5}$ Air Quality Study (CRPAQS). *Journal of Geophysical Research: Atmospheres*, *111*(D10), D10S04. https://doi.org/10.1029/2005JD006457

Clinton, N., & Gong, P. (2013). MODIS detected surface urban heat islands and sinks: Global locations and controls. *Remote Sensing of Environment*, *134*, 294–304. https://doi.org/10.1016/j.rse.2013.03.008

Colmer, J., Hardman, I., Shimshack, J., & Voorheis, J. (2020). Disparities in $PM_{2.5}$ air pollution in the United States. *Science*, *369*(6503), 575–578. https://doi.org/10.1126/science.aaz9353

Cusworth, D. H., Duren, R. M., Ayasse, A. K., Jiorle, R., Howell, K., Aubrey, A., Green, R. O., Eastwood, M. L., Chapman, J. W., Thorpe, A. K., Heckler, J., Asner, G. P., Smith, M. L., Thoma, E., Krause, M. J., Heins, D., & Thorneloe, S. (2024). Quantifying methane emissions from United States landfills. *Science*, *383*(6690), 1499–1504. https://doi.org/10.1126/science.adi7735

Cusworth, D. H., Duren, R. M., Yadav, V., Thorpe, A. K., Verhulst, K., Sander, S., Hopkins, F., Rafiq, T., & Miller, C. E. (2020). Synthesis of Methane Observations Across Scales:

Strategies for Deploying a Multitiered Observing Network. *Geophysical Research Letters*, *47*(7), e2020GL087869. https://doi.org/10.1029/2020GL087869

Darbieu, C., Lohou, F., Lothon, M., Vilà-Guerau de Arellano, J., Couvreux, F., Durand, P., Pino, D., Patton, E. G., Nilsson, E., Blay-Carreras, E., & Gioli, B. (2015). Turbulence vertical structure of the boundary layer during the afternoon transition. *Atmospheric Chemistry and Physics*, *15*(17), 10071–10086. https://doi.org/10.5194/acp-15-10071-2015

Deng, B., Zhu, L., Zhang, Y., Tang, Z., Shen, J., Zhang, Y., Zheng, H., & Zhang, Y. (2024). Short-term exposure to $PM_{2.5}$ constituents, extreme temperature events and stroke mortality. *Science of The Total Environment*, *954*, 176506. https://doi.org/10.1016/j.scitotenv.2024.176506

Di, Q., Amini, H., Shi, L., Kloog, I., Silvern, R., Kelly, J., Sabath, M. B., Choirat, C., Koutrakis, P., Lyapustin, A., Wang, Y., Mickley, L. J., & Schwartz, J. (2019). An ensemble-based model of $PM_{2.5}$ concentration across the contiguous United States with high spatiotemporal resolution. *Environment International*, *130*, 104909. https://doi.org/10.1016/j.envint.2019.104909

Duan, K., Sun, G., Zhang, Y., Yahya, K., Wang, K., Madden, J. M., Caldwell, P. V., Cohen, E. C., & McNulty, S. G. (2017). Impact of air pollution induced climate change on water availability and ecosystem productivity in the conterminous United States. *Climatic Change*, *140*(2), 259–272. https://doi.org/10.1007/s10584-016-1850-7

Ebi, K. L., Capon, A., Berry, P., Broderick, C., Dear, R. de, Havenith, G., Honda, Y., Kovats, R. S., Ma, W., Malik, A., Morris, N. B., Nybo, L., Seneviratne, S. I., Vanos, J., & Jay, O. (2021). Hot weather and heat extremes: Health risks. *The Lancet*, *398*(10301), 698–708. https://doi.org/10.1016/S0140-6736(21)01208-3

Eiguren-Fernandez, A., Miguel ,Antonio H., Froines ,John R., Thurairatnam ,Suresh, & and Avol, E. L. (2004). Seasonal and spatial variation of polycyclic aromatic hydrocarbons in vapor-phase and $PM_{2.5}$ in Southern California urban and rural communities. *Aerosol Science and Technology*, *38*(5), 447–455. https://doi.org/10.1080/02786820490449511

Erickson, L. E. (2017). Reducing greenhouse gas emissions and improving air quality: Two global challenges. *Environmental Progress & Sustainable Energy*, *36*(4), 982–988. https://doi.org/10.1002/ep.12665

Fang, Y., Naik, V., Horowitz, L. W., & Mauzerall, D. L. (2013). Air pollution and associated human mortality: The role of air pollutant emissions, climate change and methane concentration increases from the preindustrial period to present. *Atmospheric Chemistry and Physics*, *13*(3), 1377–1394. https://doi.org/10.5194/acp-13-1377-2013

Feng, S., Gao, D., Liao, F., Zhou, F., & Wang, X. (2016). The health effects of ambient $PM_{2.5}$ and potential mechanisms. *Ecotoxicology and Environmental Safety*, *128*, 67–74. https://doi.org/10.1016/j.ecoenv.2016.01.030

Feron, S., Cordero, R. R., Damiani, A., Oyola, P., Ansari, T., Pedemonte, J. C., Wang, C., Ouyang, Z., & Gallo, V. (2023). Compound climate-pollution extremes in Santiago de Chile. *Scientific Reports*, *13*, 6726. https://doi.org/10.1038/s41598-023-33890-w

Filonchyk, M., Peterson, M. P., Zhang, L., Hurynovich, V., & He, Y. (2024). Greenhouse gases emissions and global climate change: Examining the influence of CO2, CH4, and N2O. *Science of The Total Environment*, *935*, 173359. https://doi.org/10.1016/j.scitotenv.2024.173359

Geng, X., Zhang, D., Li, C., Yuan, Y., Yu, Z., & Wang, X. (2023). Impacts of climatic zones on urban heat island: Spatiotemporal variations, trends, and drivers in China from 2001–

2020. *Sustainable Cities and Society*, *89*, 104303. https://doi.org/10.1016/j.scs.2022.104303

Grimsdell, A. W., & Angevine, W. M. (2002). Observations of the Afternoon Transition of the Convective Boundary Layer. *Journal of Applied Meteorology and Climatology*, *41*(1), 3–11. https://doi.org/10.1175/1520-0450(2002)041%3C0003:OOTATO%3E2.0.CO;2

Guerreiro, S. B., Dawson, R. J., Kilsby, C., Lewis, E., & Ford, A. (2018). Future heat-waves, droughts and floods in 571 European cities. *Environmental Research Letters*, *13*(3), 034009. https://doi.org/10.1088/1748-9326/aaaad3

Guo, J., Xia, F., Zhang, Y., Liu, H., Li, J., Lou, M., He, J., Yan, Y., Wang, F., Min, M., & Zhai, P. (2017). Impact of diurnal variability and meteorological factors on the $PM_{2.5}$—AOD relationship: Implications for $PM_{2.5}$ remote sensing. *Environmental Pollution*, *221*, 94–104. https://doi.org/10.1016/j.envpol.2016.11.043

Habeeb, D., Vargo, J., & Stone, B. (2015). Rising heat wave trends in large US cities. *Natural Hazards*, *76*(3), 1651–1665. https://doi.org/10.1007/s11069-014-1563-z

Han, L., Yu, C. W., & Cao, S.-J. (2024). Synergistic control of air pollution and heat waves in the urban built environment: Challenges and opportunities. *Indoor and Built Environment*, *33*(3), 417–421. https://doi.org/10.1177/1420326X231176362

He, K., Huo, H., & Zhang, Q. (2002). Urban air pollution in China: Current status, characteristics, and progress. *Annual Review of Environment and Resources*, *27*(Volume 27, 2002), 397–431. https://doi.org/10.1146/annurev.energy.27.122001.083421

Heilig, G. K. (1994). The greenhouse gas methane (CH4): Sources and sinks, the impact of population growth, possible interventions. *Population and Environment*, *16*(2), 109–137. https://doi.org/10.1007/BF02208779

Hong, C., Zhang, Q., Zhang, Y., Tang, Y., Tong, D., & He, K. (2017). Multi-year downscaling application of two-way coupled WRF v3.4 and CMAQ v5.0.2 over east Asia for regional climate and air quality modeling: Model evaluation and aerosol direct effects. *Geoscientific Model Development*, *10*(6), 2447–2470. https://doi.org/10.5194/gmd-10-2447-2017

Hu, L., Andrews, A. E., Montzka, S. A., Miller, S. M., Bruhwiler, L., Oh, Y., Sweeney, C., Miller, J. B., McKain, K., Ibarra Espinosa, S., Davis, K., Miles, N., Mountain, M., Lan, X., Crotwell, A., Madronich, M., Mefford, T., Michel, S., & Houwelling, S. (2025). An Unexpected Seasonal Cycle in U.S. Oil and Gas Methane Emissions. *Environmental Science & Technology*, *59*(20), 9968–9979. https://doi.org/10.1021/acs.est.4c14090

Hu, X.-M., Honeycutt, W. T., Wang, C., Weng, B., Zhou, B., & Xue, M. (2025). Observation and Simulation of Methane Plumes During the Morning Boundary Layer Transition. *Journal of Geophysical Research: Atmospheres*, *130*(7), e2024JD042317. https://doi.org/10.1029/2024JD042317

Hu, X.-M., Li, X., Zhou, B., & Xue, M. (2024). Air Pollution Meteorology. In *Reference Module in Earth Systems and Environmental Sciences*. Elsevier. https://doi.org/10.1016/B978-0-323-96026-7.00021-7

Hu, X.-M., & Xue, M. (2016). Influence of synoptic sea-breeze fronts on the urban heat island intensity in Dallas–Fort Worth, Texas. *Monthly Weather Review*, *144*(4), 1487–1507. https://doi.org/10.1175/MWR-D-15-0201.1

Hu, X.-M., Zhang, Y., Jacobson, M. Z., & Chan, C. K. (2008). Coupling and evaluating gas/particle mass transfer treatments for aerosol simulation and forecast. *Journal of Geophysical Research*, *113*, D11208. https://doi.org/10.1029/2007JD009588

IPCC. (2023). *Climate Change 2023: Synthesis Report* (No. AR6; Contribution of Working Groups I, II and III to the Sixth Assessment Report of the Intergovernmental Panel on Climate Change). Intergovernmental Panel on Climate Change. https://doi.org/10.59327/IPCC/AR6-9789291691647

Jackson, R. B., Irvin, J. A., Ramachandran, N., Wang, C., Ouyang, Z., Tulloch, P. A., Liu, F. Y., & Ng, A. Y. (2026). MEthane Tracking Emissions Reference (METER): A global database of methane-emitting infrastructure. *Earth System Science Data Discussions*, 1–54. https://doi.org/10.5194/essd-2026-124

Jacob, D. J., Turner, A. J., Maasakkers, J. D., Sheng, J., Sun, K., Liu, X., Chance, K., Aben, I., McKeever, J., & Frankenberg, C. (2016). Satellite observations of atmospheric methane and their value for quantifying methane emissions. *Atmospheric Chemistry and Physics*, *16*(22), 14371–14396. https://doi.org/10.5194/acp-16-14371-2016

Jacob, D. J., Varon, D. J., Cusworth, D. H., Dennison, P. E., Frankenberg, C., Gautam, R., Guanter, L., Kelley, J., McKeever, J., Ott, L. E., Poulter, B., Qu, Z., Thorpe, A. K., Worden, J. R., & Duren, R. M. (2022). Quantifying methane emissions from the global scale down to point sources using satellite observations of atmospheric methane. *Atmospheric Chemistry and Physics*, *22*(14), 9617–9646. https://doi.org/10.5194/acp-22-9617-2022

Ji, S., Zhou, Q., Jiang, Y., He, C., Chen, Y., Wu, C., & Liu, B. (2020). The interactive effects between particulate matter and heat waves on circulatory mortality in Fuzhou, China. *International Journal of Environmental Research and Public Health*, *17*(16), 5979. https://doi.org/10.3390/ijerph17165979

Jiang, S., Lee, X., Wang, J., & Wang, K. (2019). Amplified urban heat islands during heat wave periods. *Journal of Geophysical Research: Atmospheres*, *124*(14), 7797–7812. https://doi.org/10.1029/2018JD030230

Juang, C. S., Williams, A. P., Abatzoglou, J. T., Balch, J. K., Hurteau, M. D., & Moritz, M. A. (2022). Rapid growth of large Forest fires drives the exponential response of annual forest-fire area to aridity in the western United States. *Geophysical Research Letters*, *49*(5), e2021GL097131. https://doi.org/10.1029/2021GL097131

Karakurt, I., Aydin, G., & Aydiner, K. (2012). Sources and mitigation of methane emissions by sectors: A critical review. *Renewable Energy*, *39*(1), 40–48. https://doi.org/10.1016/j.renene.2011.09.006

Kim, B. M., Seo, J., Kim, J. Y., Lee, J. Y., & Kim, Y. (2016). Transported vs. Local contributions from secondary and biomass burning sources to $PM_{2.5}$. *Atmospheric Environment*, *144*, 24–36. https://doi.org/10.1016/j.atmosenv.2016.08.072

Kirschke, S., Bousquet, P., Ciais, P., Saunois, M., Canadell, J. G., Dlugokencky, E. J., Bergamaschi, P., Bergmann, D., Blake, D. R., Bruhwiler, L., Cameron-Smith, P., Castaldi, S., Chevallier, F., Feng, L., Fraser, A., Heimann, M., Hodson, E. L., Houweling, S., Josse, B., … Zeng, G. (2013). Three decades of global methane sources and sinks. *Nature Geoscience*, *6*(10), 813–823. https://doi.org/10.1038/ngeo1955

Kovats, R. S., & Hajat, S. (2008). Heat stress and public health: A critical review. *Annual Review of Public Health*, *29*, 41–55. https://doi.org/10.1146/annurev.publhealth.29.020907.090843

Kumar, P., Caldow, C., Broquet, G., Shah, A., Laurent, O., Yver-Kwok, C., Ars, S., Defratyka, S., Gichuki, S. W., Lienhardt, L., Lozano, M., Paris, J.-D., Vogel, F., Bouchet, C., Allegrini,

E., Kelly, R., Juery, C., & Ciais, P. (2024). Detection and long-term quantification of methane emissions from an active landfill. *Atmospheric Measurement Techniques*, *17*(4), 1229–1250. https://doi.org/10.5194/amt-17-1229-2024

Lan, X., Nisbet, E. G., Dlugokencky, E. J., & Michel, S. E. (2021). What do we know about the global methane budget? Results from four decades of atmospheric CH4 observations and the way forward. *Philosophical Transactions of the Royal Society A: Mathematical, Physical and Engineering Sciences*, *379*(2210), 20200440. https://doi.org/10.1098/rsta.2020.0440

Lapworth, A. (2006). The Morning Transition of the Nocturnal Boundary Layer. *Boundary-Layer Meteorology*, *119*(3), 501–526. https://doi.org/10.1007/s10546-005-9046-0

Leffel, J., Wang, C., Hu, X.-M., Feron, S., & Henry, S. (2025). Cities as hotspots of compound heat and fine particulate matter pollution: A 23-year urban–rural comparison across the United States. *Environmental Research*, *285*, 122508. https://doi.org/10.1016/j.envres.2025.122508

Lei, H., Wang, J. X. L., Tong, D. Q., & Lee, P. (2016). Merged dust climatology in Phoenix, Arizona based on satellite and station data. *Climate Dynamics*, *47*(9), 2785–2799. https://doi.org/10.1007/s00382-016-2997-7

Li, D., & Bou-Zeid, E. (2013). Synergistic interactions between urban heat islands and heat waves: The impact in cities is larger than the sum of its parts. *Journal of Applied Meteorology and Climatology*, *52*(9), 2051–2064. https://doi.org/10.1175/JAMC-D-13-02.1

Li, X., Zhang, C., Liu, P., Liu, J., Zhang, Y., Liu, C., & Mu, Y. (2020). Significant influence of the intensive agricultural activities on atmospheric $PM_{2.5}$ during autumn harvest seasons

in a rural area of the North China Plain. *Atmospheric Environment*, *241*, 117844. https://doi.org/10.1016/j.atmosenv.2020.117844

Li, X., Zhou, Y., Asrar, G. R., & Zhu, Z. (2018). Developing a 1 km resolution daily air temperature dataset for urban and surrounding areas in the conterminous United States. *Remote Sensing of Environment*, *215*, 74–84. https://doi.org/10.1016/j.rse.2018.05.034

Liang, C.-S., Duan, F.-K., He, K.-B., & Ma, Y.-L. (2016). Review on recent progress in observations, source identifications and countermeasures of PM2.5. *Environment International*, *86*, 150–170. https://doi.org/10.1016/j.envint.2015.10.016

Liao, W., Liu, X., Li, D., Luo, M., Wang, D., Wang, S., Baldwin, J., Lin, L., Li, X., Feng, K., Hubacek, K., & Yang, X. (2018). Stronger contributions of urbanization to heat wave trends in wet climates. *Geophysical Research Letters*, *45*(20), 11310–11317. https://doi.org/10.1029/2018GL079679

LI-COR. (2026). *LI-7810 Trace Gas Analyzer Real-time Methane Measurements*. LI-COR Environmental. https://www.licor.com/products/trace-gas/LI-7810

Lim, C.-H., Ryu, J., Choi, Y., Jeon, S. W., & Lee, W.-K. (2020). Understanding global PM2.5 concentrations and their drivers in recent decades (1998–2016). *Environment International*, *144*, 106011. https://doi.org/10.1016/j.envint.2020.106011

Liu, J., Varghese, B. M., Hansen, A., Zhang, Y., Driscoll, T., Morgan, G., Dear, K., Gourley, M., Capon, A., & Bi, P. (2022). Heat exposure and cardiovascular health outcomes: A systematic review and meta-analysis. *The Lancet Planetary Health*, *6*(6), e484–e495. https://doi.org/10.1016/S2542-5196(22)00117-6

Liu, S., Shu, L., Zhu, L., Song, Y., Sun, W., Chen, Y., Wang, D., Pu, D., Li, X., Sun, S., Li, J., Zuo, X., Fu, W., Yang, X., & Fu, T.-M. (2024). Underappreciated emission spikes from

power plants during heatwaves observed from space: Case studies in India and China. *Earth's Future*, *12*(2), e2023EF003937. https://doi.org/10.1029/2023EF003937

Ma, Y., Zang, E., Liu, Y., Wei, J., Lu, Y., Krumholz, H. M., Bell, M. L., & Chen, K. (2024). Long-term exposure to wildland fire smoke $PM_{2.5}$ and mortality in the contiguous United States. *Proceedings of the National Academy of Sciences of the United States of America*, *121*(40), e2403960121. https://doi.org/10.1073/pnas.2403960121

Manoli, G., Fatichi, S., Schläpfer, M., Yu, K., Crowther, T. W., Meili, N., Burlando, P., Katul, G. G., & Bou-Zeid, E. (2019). Magnitude of urban heat islands largely explained by climate and population. *Nature*, *573*(7772), 55–60. https://doi.org/10.1038/s41586-019-1512-9

Mar, K. A., Unger, C., Walderdorff, L., & Butler, T. (2022). Beyond CO2 equivalence: The impacts of methane on climate, ecosystems, and health. *Environmental Science & Policy*, *134*, 127–136. https://doi.org/10.1016/j.envsci.2022.03.027

Mathew, T. A., Pillai, D., Sukumaran, J., Deshpande, M. V., Buchwitz, M., Schneising, O., Thilakan, V., Ravi, A., Kanakkassery, S. B., Vinod, A. J., Sijikumar, S., Girach, I. A., & Babu, S. S. (2026). Leveraging TROPOMI observations and WRF-GHG modeling towards improving methane emission assessments in India. *Atmospheric Chemistry and Physics*, *26*(6), 4453–4477. https://doi.org/10.5194/acp-26-4453-2026

McBain, M. C., Warland, J. S., McBride, R. A., & Wagner-Riddle, C. (2005). Micrometeorological measurements of N2O and CH4 emissions from a municipal solid waste landfill. *Waste Management & Research*, *23*(5), 409–419. https://doi.org/10.1177/0734242X05057253

McDuffie, E. E., Martin, R. V., Spadaro, J. V., Burnett, R., Smith, S. J., O'Rourke, P., Hammer, M. S., van Donkelaar, A., Bindle, L., Shah, V., Jaeglé, L., Luo, G., Yu, F., Adeniran, J. A.,

Lin, J., & Brauer, M. (2021). Source sector and fuel contributions to ambient $PM_{2.5}$ and attributable mortality across multiple spatial scales. *Nature Communications*, *12*, 3594. https://doi.org/10.1038/s41467-021-23853-y

Meehl, G. A., & Tebaldi, C. (2004). More intense, more frequent, and longer lasting heat waves in the 21st century. *Science*, *305*(5686), 994–997. https://doi.org/10.1126/science.1098704

Meng, X., Garay, M. J., Diner, D. J., Kalashnikova, O. V., Xu, J., & Liu, Y. (2018). Estimating $PM_{2.5}$ speciation concentrations using prototype 4.4 km-resolution MISR aerosol properties over Southern California. *Atmospheric Environment*, *181*, 70–81. https://doi.org/10.1016/j.atmosenv.2018.03.019

Mønster, J., Kjeldsen, P., & Scheutz, C. (2019). Methodologies for measuring fugitive methane emissions from landfills – A review. *Waste Management*, *87*, 835–859. https://doi.org/10.1016/j.wasman.2018.12.047

Mosher, B. W., Czepiel, P. M., Harriss, R. C., Shorter, J. H., Kolb, C. E., McManus, J. B., Allwine, E., & Lamb, B. K. (1999). Methane Emissions at Nine Landfill Sites in the Northeastern United States. *Environmental Science & Technology*, *33*(12), 2088–2094. https://doi.org/10.1021/es981044z

Naserikia, M., Hart, M. A., Nazarian, N., Bechtel, B., Lipson, M., & Nice, K. A. (2023). Land surface and air temperature dynamics: The role of urban form and seasonality. *Science of The Total Environment*, *905*, 167306. https://doi.org/10.1016/j.scitotenv.2023.167306

Nesser, H., Jacob, D. J., Maasakkers, J. D., Lorente, A., Chen, Z., Lu, X., Shen, L., Qu, Z., Sulprizio, M. P., Winter, M., Ma, S., Bloom, A. A., Worden, J. R., Stavins, R. N., & Randles, C. A. (2024). High-resolution US methane emissions inferred from an inversion

of 2019 TROPOMI satellite data: Contributions from individual states, urban areas, and landfills. *Atmospheric Chemistry and Physics*, *24*(8), 5069–5091. https://doi.org/10.5194/acp-24-5069-2024

Oke, T. R., Mills, G., Christen, A., & Voogt, J. A. (2017). *Urban Climates*. Cambridge University Press. https://doi.org/10.1017/9781139016476

Palmer, P. I., Feng, L., Lunt, M. F., Parker, R. J., Bösch, H., Lan, X., Lorente, A., & Borsdorff, T. (2021). The added value of satellite observations of methane forunderstanding the contemporary methane budget. *Philosophical Transactions of the Royal Society A: Mathematical, Physical and Engineering Sciences*, *379*(2210), 20210106. https://doi.org/10.1098/rsta.2021.0106

Park, K., Jin, H.-G., & Baik, J.-J. (2023). Do heat waves worsen air quality? A 21-year observational study in Seoul, South Korea. *Science of The Total Environment*, *884*, 163798. https://doi.org/10.1016/j.scitotenv.2023.163798

Patra, P. K., Houweling, S., Krol, M., Bousquet, P., Belikov, D., Bergmann, D., Bian, H., Cameron-Smith, P., Chipperfield, M. P., Corbin, K., Fortems-Cheiney, A., Fraser, A., Gloor, E., Hess, P., Ito, A., Kawa, S. R., Law, R. M., Loh, Z., Maksyutov, S., … Wilson, C. (2011). TransCom model simulations of CH_4 and related species: Linking transport, surface flux and chemical loss with CH_4 variability in the troposphere and lower stratosphere. *Atmospheric Chemistry and Physics*, *11*(24), 12813–12837. https://doi.org/10.5194/acp-11-12813-2011

Peng, S., Piao, S., Ciais, P., Friedlingstein, P., Ottle, C., Bréon, F.-M., Nan, H., Zhou, L., & Myneni, R. B. (2012). Surface urban heat island across 419 global big cities. *Environmental Science & Technology*, *46*(2), 696–703. https://doi.org/10.1021/es2030438

Pérez, I. A., García, M. de los Á., Sánchez, M. L., & Pardo, N. (2021). Influence of Wind Speed on CO2 and CH4 Concentrations at a Rural Site. *International Journal of Environmental Research and Public Health*, *18*(16), 8397. https://doi.org/10.3390/ijerph18168397

Perkins, S. E., & Alexander, L. V. (2013). On the measurement of heat waves. *Journal of Climate*, *26*(13), 4500–4517. https://doi.org/10.1175/JCLI-D-12-00383.1

Perkins, S. E., Alexander, L. V., & Nairn, J. R. (2012). Increasing frequency, intensity and duration of observed global heatwaves and warm spells. *Geophysical Research Letters*, *39*(20), L20714. https://doi.org/10.1029/2012GL053361

Perkins-Kirkpatrick, S. E., & Gibson, P. B. (2017). Changes in regional heatwave characteristics as a function of increasing global temperature. *Scientific Reports*, *7*, 12256. https://doi.org/10.1038/s41598-017-12520-2

Perkins-Kirkpatrick, S. E., & Lewis, S. C. (2020). Increasing trends in regional heatwaves. *Nature Communications*, *11*, Article 1. https://doi.org/10.1038/s41467-020-16970-7

Phelan, P. E., Kaloush, K., Miner, M., Golden, J., Phelan, B., Silva, H., & Taylor, R. A. (2015). Urban heat island: Mechanisms, implications, and possible remedies. *Annual Review of Environment and Resources*, *40*, 285–307. https://doi.org/10.1146/annurev-environ-102014-021155

Ramamurthy, P., & Bou-Zeid, E. (2017). Heatwaves and urban heat islands: A comparative analysis of multiple cities. *Journal of Geophysical Research: Atmospheres*, *122*(1), 168–178. https://doi.org/10.1002/2016JD025357

Republic Services. (2018). *Republic Services®, Aria Energy and BP Celebrate the Activation of a Major Renewable Energy Project*. Republic Services News Releases.

https://media.republicservices.com/2018-09-24-Republic-Services-Aria-Energy-and-BP-Celebrate-the-Activation-of-a-Major-Renewable-Energy-Project

Saunois, M., Martinez, A., Poulter, B., Zhang, Z., Raymond, P. A., Regnier, P., Canadell, J. G., Jackson, R. B., Patra, P. K., Bousquet, P., Ciais, P., Dlugokencky, E. J., Lan, X., Allen, G. H., Bastviken, D., Beerling, D. J., Belikov, D. A., Blake, D. R., Castaldi, S., … Zhuang, Q. (2025). Global Methane Budget 2000–2020. *Earth System Science Data*, *17*(5), 1873–1958. https://doi.org/10.5194/essd-17-1873-2025

Saunois, M., Stavert, A. R., Poulter, B., Bousquet, P., Canadell, J. G., Jackson, R. B., Raymond, P. A., Dlugokencky, E. J., Houweling, S., Patra, P. K., Ciais, P., Arora, V. K., Bastviken, D., Bergamaschi, P., Blake, D. R., Brailsford, G., Bruhwiler, L., Carlson, K. M., Carrol, M., … Zhuang, Q. (2020). The Global Methane Budget 2000–2017. *Earth System Science Data*, *12*(3), 1561–1623. https://doi.org/10.5194/essd-12-1561-2020

Scarpelli, T. R., Cusworth, D. H., Duren, R. M., Kim, J., Heckler, J., Asner, G. P., Thoma, E., Krause, M. J., Heins, D., & Thorneloe, S. (2024). Investigating Major Sources of Methane Emissions at US Landfills. *Environmental Science & Technology*, *58*(49), 21545–21556. https://doi.org/10.1021/acs.est.4c07572

Schwarz, N., Lautenbach, S., & Seppelt, R. (2011). Exploring indicators for quantifying surface urban heat islands of European cities with MODIS land surface temperatures. *Remote Sensing of Environment*, *115*(12), 3175–3186. https://doi.org/10.1016/j.rse.2011.07.003

Sicard, P., Agathokleous, E., Anenberg, S. C., De Marco, A., Paoletti, E., & Calatayud, V. (2023). Trends in urban air pollution over the last two decades: A global perspective. *Science of The Total Environment*, *858*, 160064. https://doi.org/10.1016/j.scitotenv.2022.160064

Simpson, C. H., Brousse, O., & Heaviside, C. (2024). Estimated mortality attributable to the urban heat island during the record-breaking 2022 heatwave in London. *Environmental Research Letters*, *19*(9), 094047. https://doi.org/10.1088/1748-9326/ad6c65

Skeie, R. B., Hodnebrog, Ø., & Myhre, G. (2023). Trends in atmospheric methane concentrations since 1990 were driven and modified by anthropogenic emissions. *Communications Earth & Environment*, *4*(1), 317. https://doi.org/10.1038/s43247-023-00969-1

Skyllakou, K., Rivera, P. G., Dinkelacker, B., Karnezi, E., Kioutsioukis, I., Hernandez, C., Adams, P. J., & Pandis, S. N. (2021). Changes in $PM_{2.5}$ concentrations and their sources in the US from 1990 to 2010. *Atmospheric Chemistry and Physics*, *21*(22), 17115–17132. https://doi.org/10.5194/acp-21-17115-2021

Smith, T. T., Zaitchik, B. F., & Gohlke, J. M. (2013). Heat waves in the United States: Definitions, patterns and trends. *Climatic Change*, *118*(3), 811–825. https://doi.org/10.1007/s10584-012-0659-2

Tan, J., Zheng, Y., Tang, X., Guo, C., Li, L., Song, G., Zhen, X., Yuan, D., Kalkstein, A. J., Li, F., & Chen, H. (2010). The urban heat island and its impact on heat waves and human health in Shanghai. *International Journal of Biometeorology*, *54*(1), 75–84. https://doi.org/10.1007/s00484-009-0256-x

Themelis, N. J., & Ulloa, P. A. (2007). Methane generation in landfills. *Renewable Energy*, *32*(7), 1243–1257. https://doi.org/10.1016/j.renene.2006.04.020

Thompson, L., Wang, C., He, C., Lin, T.-S., Liu, C., & Dudhia, J. (2025). Assessment of convection-permitting hydroclimate modeling in urban areas across the contiguous United States. *Urban Climate*, *61*, 102375. https://doi.org/10.1016/j.uclim.2025.102375

Thornton, P. E., Shrestha, R., Thornton, M., Kao, S.-C., Wei, Y., & Wilson, B. E. (2021). Gridded daily weather data for North America with comprehensive uncertainty quantification. *Scientific Data*, *8*, 190. https://doi.org/10.1038/s41597-021-00973-0

Tong, H., Cheng, T., Li, X., Zhu, H., Ye, X., Fan, D., & Tang, T. (2025). Reduction of methane emissions through improved landfill management. *Nature Climate Change*, *15*(8), 866–872. https://doi.org/10.1038/s41558-025-02391-1

United Nations. (2015). *Transforming Our World: The 2030 Agenda for Sustainable Development* (A/RES/70/1). United Nations Department of Economic and Social Affairs. https://sdgs.un.org/publications/transforming-our-world-2030-agenda-sustainable-development-17981

United States Census Bureau. (2022). *2022 TIGER/Line® Shapefiles*. https://www.census.gov/cgi-bin/geo/shapefiles/index.php?year=2022&layergroup=Urban+Areas

U.S. EPA. (2024a). *Inventory of U.S. Greenhouse Gas Emissions and Sinks: 1990-2022* (Nos. 430-R-24–004). U.S. Environmental Protection Agency. https://www.epa.gov/ghgemissions/inventory-us-greenhouse-gas-emissions-and-sinks-1990-2022

U.S. EPA. (2024b, February 7). *NAAQS Table* [Other Policies and Guidance]. https://www.epa.gov/criteria-air-pollutants/naaqs-table

Wang, C., Hu, X.-M., Feron, S., Leffel, J., & Cordero, R. R. (2025). Compound heat and ozone pollution in the urban environment. *Urban Climate*, *62*, 102511. https://doi.org/10.1016/j.uclim.2025.102511

Wang, C., Song, J., Shi, D., Reyna, J. L., Horsey, H., Feron, S., Zhou, Y., Ouyang, Z., Li, Y., & Jackson, R. B. (2023). Impacts of climate change, population growth, and power sector decarbonization on urban building energy use. *Nature Communications*, *14*, 6434. https://doi.org/10.1038/s41467-023-41458-5

Wang, C., Wang, C. Y., Myint, S. W., & Wang, Z.-H. (2017). Landscape determinants of spatio-temporal patterns of aerosol optical depth in the two most polluted metropolitans in the United States. *Science of The Total Environment*, *609*, 1556–1565. https://doi.org/10.1016/j.scitotenv.2017.07.273

Wang, C., Wang, Z.-H., & Li, Q. (2020). Emergence of urban clustering among U.S. cities under environmental stressors. *Sustainable Cities and Society*, *63*, 102481. https://doi.org/10.1016/j.scs.2020.102481

Wang, C., Wang, Z.-H., & Sun, L. (2020). Early-warning signals for critical temperature transitions. *Geophysical Research Letters*, *47*(14), e2020GL088503. https://doi.org/10.1029/2020GL088503

Wang, L., Li, M., Wang, Q., Li, Y., Xin, J., Tang, X., Du, W., Song, T., Li, T., Sun, Y., Gao, W., Hu, B., & Wang, Y. (2022). Air stagnation in China: Spatiotemporal variability and differing impact on $PM_{2.5}$ and O_3 during 2013–2018. *Science of The Total Environment*, *819*, 152778. https://doi.org/10.1016/j.scitotenv.2021.152778

Wang, X., Jacob, D. J., Nesser, H., Balasus, N., Estrada, L. A., Sulprizio, M. P., Cusworth, D. H., Scarpelli, T. R., Chen, Z., East, J. D., & Varon, D. J. (2026). Quantifying urban and landfill methane emissions in the United States using TROPOMI satellite data. *Science Advances*, *12*(13), eadz9308. https://doi.org/10.1126/sciadv.adz9308

Wang, Y., Fang, M., Lou, Z., He, H., Guo, Y., Pi, X., Wang, Y., Yin, K., & Fei, X. (2024). Methane emissions from landfills differentially underestimated worldwide. *Nature Sustainability*, *7*(4), 496–507. https://doi.org/10.1038/s41893-024-01307-9

Wei, J., Li, Z., Lyapustin, A., Wang, J., Dubovik, O., Schwartz, J., Sun, L., Li, C., Liu, S., & Zhu, T. (2023). First close insight into global daily gapless 1 km $PM_{2.5}$ pollution, variability, and health impact. *Nature Communications*, *14*, 8349. https://doi.org/10.1038/s41467-023-43862-3

West, J. J., Fiore, A. M., Horowitz, L. W., & Mauzerall, D. L. (2006). Global health benefits of mitigating ozone pollution with methane emission controls. *Proceedings of the National Academy of Sciences*, *103*(11), 3988–3993. https://doi.org/10.1073/pnas.0600201103

West, J. J., Smith, S. J., Silva, R. A., Naik, V., Zhang, Y., Adelman, Z., Fry, M. M., Anenberg, S., Horowitz, L. W., & Lamarque, J.-F. (2013). Co-benefits of mitigating global greenhouse gas emissions for future air quality and human health. *Nature Climate Change*, *3*(10), 885–889. https://doi.org/10.1038/nclimate2009

Westerling, A. L. (2016). Increasing western US forest wildfire activity: Sensitivity to changes in the timing of spring. *Philosophical Transactions of the Royal Society B: Biological Sciences*, *371*(1696), 20150178. https://doi.org/10.1098/rstb.2015.0178

Whiting, E., Plant, G., Kort, E. A., Aben, I., Biener, K. J., Leguijt, G., & Maasakkers, J. D. (2026). Space-based observation of global increase in urban methane emissions from 2019–2023. *Proceedings of the National Academy of Sciences*, *123*(16), e2504211123. https://doi.org/10.1073/pnas.2504211123

WHO. (2021). *WHO global air quality guidelines: Particulate matter ($PM_{2.5}$ and PM_{10}), ozone, nitrogen dioxide, sulfur dioxide and carbon monoxide*. World Health Organization. https://iris.who.int/handle/10665/345329

Wyer, K. E., Kelleghan, D. B., Blanes-Vidal, V., Schauberger, G., & Curran, T. P. (2022). Ammonia emissions from agriculture and their contribution to fine particulate matter: A review of implications for human health. *Journal of Environmental Management*, *323*, 116285. https://doi.org/10.1016/j.jenvman.2022.116285

Xie, Y., Lin, M., & Horowitz, L. W. (2020). Summer $PM_{2.5}$ pollution extremes caused by wildfires over the western United States during 2017–2018. *Geophysical Research Letters*, *47*(16), e2020GL089429. https://doi.org/10.1029/2020GL089429

Yang, B., Zhu, Q., Wang, W., Zhu, Q., Zhang, D., Jin, Z., Prasad, P., Sowlat, M., Pakbin, P., Ahangar, F., Hasheminassab, S., & Liu, Y. (2024). Impact of warehouse expansion on ambient $PM_{2.5}$ and elemental carbon levels in Southern California's disadvantaged communities: A two-decade analysis. *GeoHealth*, *8*(9), e2024GH001091. https://doi.org/10.1029/2024GH001091

Yang, D., Ye, C., Wang, X., Lu, D., Xu, J., & Yang, H. (2018). Global distribution and evolvement of urbanization and $PM_{2.5}$ (1998–2015). *Atmospheric Environment*, *182*, 171–178. https://doi.org/10.1016/j.atmosenv.2018.03.053

Yang, J., & Bou-Zeid, E. (2019). Designing sensor networks to resolve spatio-temporal urban temperature variations: Fixed, mobile or hybrid? *Environmental Research Letters*, *14*(7), 074022. https://doi.org/10.1088/1748-9326/ab25f8

Yang, X., Wang, Z.-H., Wang, C., & Lai, Y.-C. (2024). Megacities are causal pacemakers of extreme heatwaves. *Npj Urban Sustainability*, *4*, 8. https://doi.org/10.1038/s42949-024-00148-x

Ye, X., Lauvaux, T., Kort, E. A., Oda, T., Feng, S., Lin, J. C., Yang, E. G., & Wu, D. (2020). Constraining Fossil Fuel CO2 Emissions From Urban Area Using OCO-2 Observations of Total Column CO2. *Journal of Geophysical Research: Atmospheres*, *125*(8), e2019JD030528. https://doi.org/10.1029/2019JD030528

Yitshak-Sade, M., Bobb, J. F., Schwartz, J. D., Kloog, I., & Zanobetti, A. (2018). The association between short and long-term exposure to $PM_{2.5}$ and temperature and hospital admissions in New England and the synergistic effect of the short-term exposures. *Science of The Total Environment*, *639*, 868–875. https://doi.org/10.1016/j.scitotenv.2018.05.181

Yusuf, R. O., Noor, Z. Z., Abba, A. H., Hassan, M. A. A., & Din, M. F. M. (2012). Methane emission by sectors: A comprehensive review of emission sources and mitigation methods. *Renewable and Sustainable Energy Reviews*, *16*(7), 5059–5070. https://doi.org/10.1016/j.rser.2012.04.008

Zhang, T., Zhou, Y., Zhao, K., Zhu, Z., Chen, G., Hu, J., & Wang, L. (2022). A global dataset of daily maximum and minimum near-surface air temperature at 1 km resolution over land (2003–2020). *Earth System Science Data*, *14*(12), 5637–5649. https://doi.org/10.5194/essd-14-5637-2022

Zhao, H., Themelis, N., Bourtsalas, A., & McGillis, W. (2019). *Methane Emissions from Landfills*. https://doi.org/10.13140/RG.2.2.17326.77120

Zhao, L., Oppenheimer, M., Zhu, Q., Baldwin, J. W., Ebi, K. L., Bou-Zeid, E., Guan, K., & Liu, X. (2018). Interactions between urban heat islands and heat waves. *Environmental Research Letters*, *13*(3), 034003. https://doi.org/10.1088/1748-9326/aa9f73

Zhou, B., Rybski, D., & Kropp, J. P. (2013). On the statistics of urban heat island intensity. *Geophysical Research Letters*, *40*(20), 5486–5491. https://doi.org/10.1002/2013GL057320

Zhou, L., Wang, Y., Wang, Q., Ding, Z., Jin, H., Zhang, T., & Zhu, B. (2023). The interactive effects of extreme temperatures and $PM_{2.5}$ pollution on mortalities in Jiangsu Province, China. *Scientific Reports*, *13*, 9479. https://doi.org/10.1038/s41598-023-36635-x

Zhou, Z., Wang, X., Yan, Y., Mijiddorj, L., Ding, Y., Beringer, T., Khiabani, P. M., Jentner, W. G., Hu, X.-M., Wang, C., Carroll, B. M., Xue, M., Ebert, D., Li, B., & Weng, B. (2026). AIMNET: An IoT-Empowered Digital Twin for Continuous Gas Emission Monitoring and Early Hazard Detection. *IEEE Internet of Things Magazine*, 1–8. https://doi.org/10.1109/MIOT.2025.3638271

Zscheischler, J., Martius, O., Westra, S., Bevacqua, E., Raymond, C., Horton, R. M., van den Hurk, B., AghaKouchak, A., Jézéquel, A., Mahecha, M. D., Maraun, D., Ramos, A. M., Ridder, N. N., Thiery, W., & Vignotto, E. (2020). A typology of compound weather and climate events. *Nature Reviews Earth & Environment*, *1*, 333–347. https://doi.org/10.1038/s43017-020-0060-z

Zscheischler, J., Westra, S., van den Hurk, B. J. J. M., Seneviratne, S. I., Ward, P. J., Pitman, A., AghaKouchak, A., Bresch, D. N., Leonard, M., Wahl, T., & Zhang, X. (2018). Future climate risk from compound events. *Nature Climate Change*, *8*, 469–477. https://doi.org/10.1038/s41558-018-0156-3

Appendix

Note A1. Climate regions in the CONUS

The nine climatically consistent regions across the CONUS, as identified by the National Centers for Environmental Information, National Oceanic and Atmospheric Administration (https://www.ncei.noaa.gov/access/monitoring/reference-maps/us-climate-regions), are:

- Northeast (NE): Connecticut, Delaware, Maine, Maryland, Massachusetts, New Hampshire, New Jersey, New York, Pennsylvania, Rhode Island, and Vermont
- Upper Midwest (UM): Iowa, Michigan, Minnesota, and Wisconsin
- Ohio Valley (OV): Illinois, Indiana, Kentucky, Missouri, Ohio, Tennessee, and West Virginia
- Southeast (SE): Alabama, Florida, Georgia, North Carolina, South Carolina, and Virginia
- Northern Rockies and Plains (NRP): Montana, Nebraska, North Dakota, South Dakota, and Wyoming
- South (SO): Arkansas, Kansas, Louisiana, Mississippi, Oklahoma, and Texas
- Southwest (SW): Arizona, Colorado, New Mexico, and Utah
- Northwest (NW): Idaho, Oregon, and Washington
- West (WE): California and Nevada

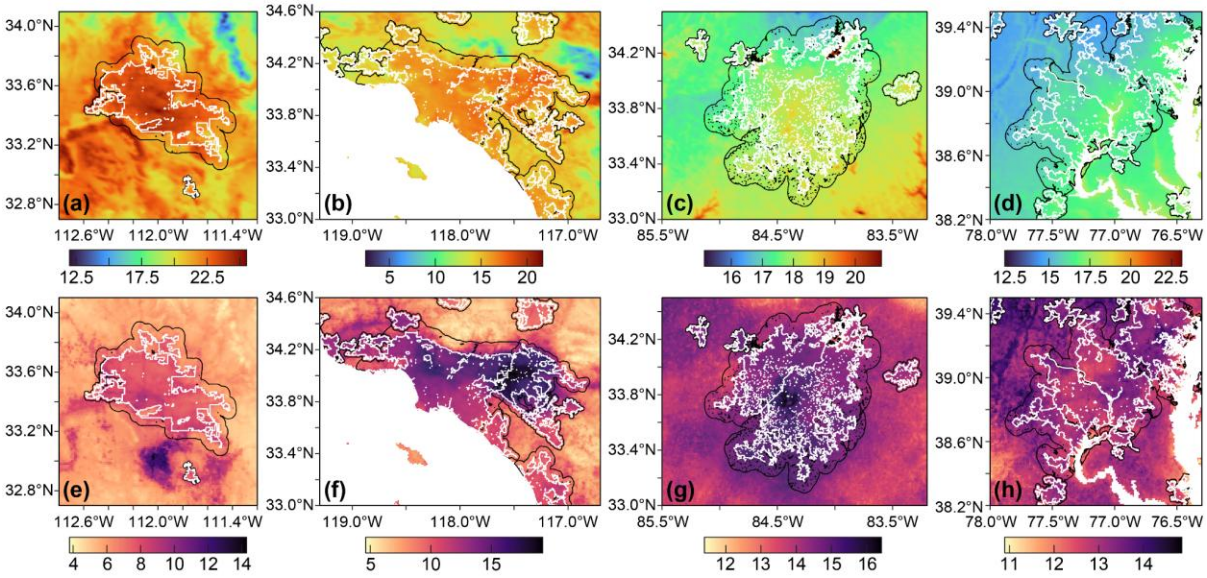


Figure A1. Spatial patterns of (a–d) daily minimum air temperature and (e–h) daily $PM_{2.5}$ concentration averaged over warm seasons for representative urban areas: (a and e) Phoenix–Mesa metropolitan area, (b and f) Los Angeles–Long Beach–Anaheim metropolitan area, (c and g) Atlanta metropolitan area, and (d and h) Washington, D.C. and Baltimore metropolitan areas. White and black boundaries represent urban and rural areas, respectively.

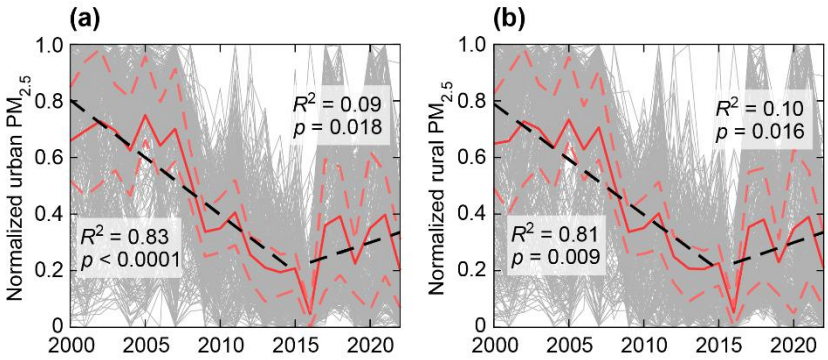


Figure A2. Long-term trends in warm-season mean $PM_{2.5}$ concentrations in (a) urban areas and (b) rural surroundings. Concentrations for each urban area are normalized by their maximum and minimum values to ease comparison (gray lines). Solid red lines are the annual mean of normalized concentrations across all areas, with dashed red lines representing the interquartile

range (25th–75th percentiles). Dashed black lines are linear fits to the annual means for 2000–2015 and 2016–2022, with corresponding R^2 and p-value (based on an F-test) shown in each subplot.

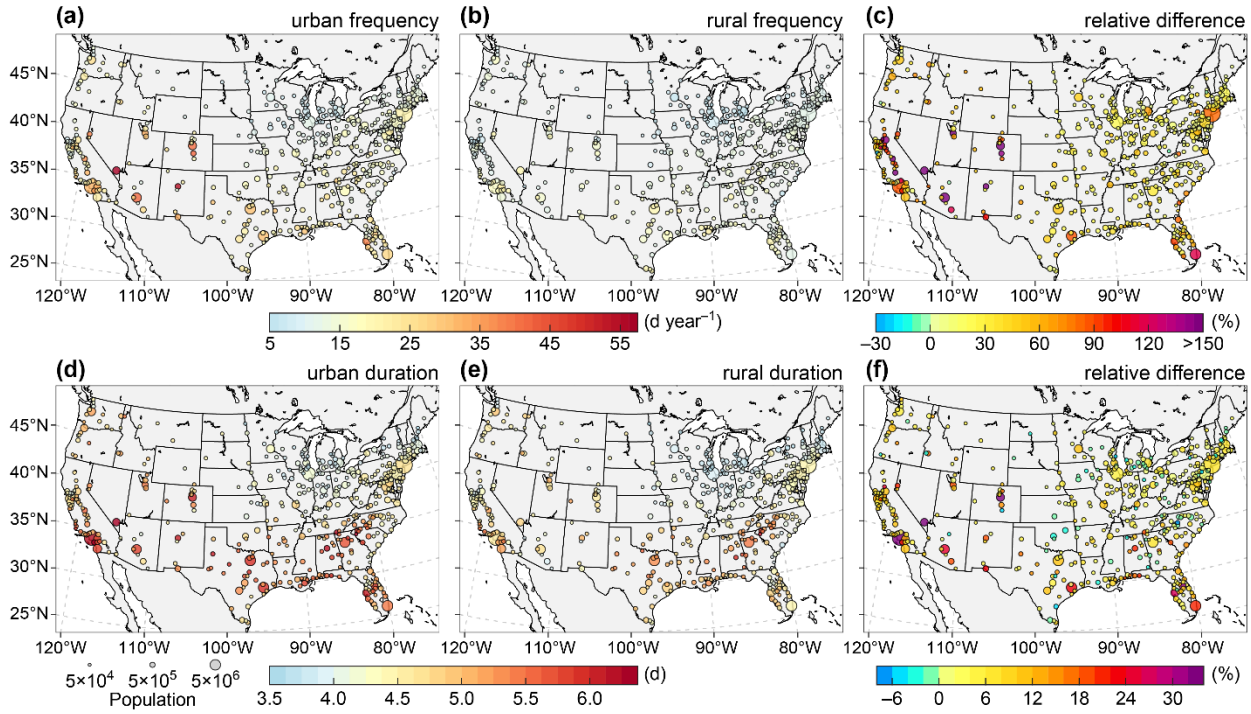


Figure A3. Frequency and duration of heat waves based on minimum temperatures in urban and surrounding rural areas during 2000–2016: (a) frequency in urban areas, (b) frequency in rural areas, (c) relative difference in frequency between urban and rural areas (urban minus rural), (d) duration in urban areas, (e) duration in rural areas, and (f) relative difference in duration between urban and rural areas (urban minus rural). Filled circles represent individual urban and rural areas, with circle sizes scaled to urban population. White circle in (f) indicates no urban–rural differences.

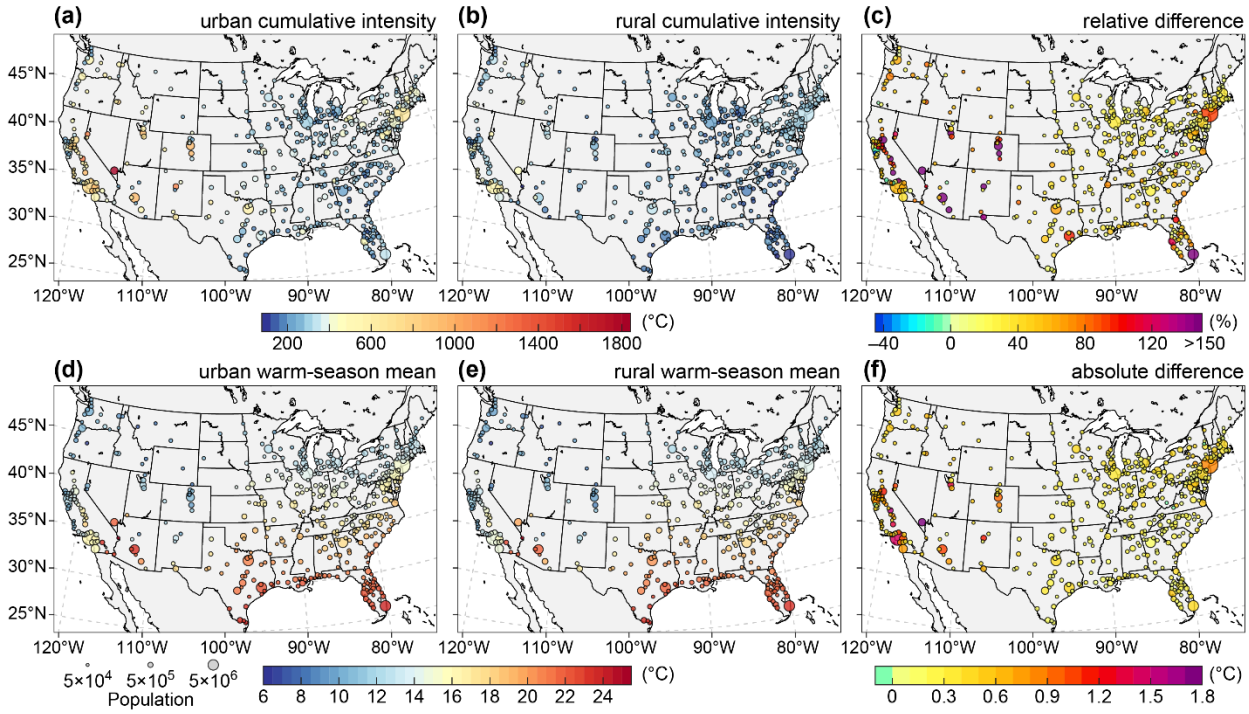


Figure A4. Cumulative intensity of heat waves based on minimum temperatures and warm-season mean minimum temperature in urban and surrounding rural areas during 2000–2016: (a) cumulative heat intensity in urban areas, (b) cumulative heat intensity in rural areas, (c) relative difference in cumulative heat intensity between urban and rural areas (urban minus rural), (d) warm-season mean minimum temperature in urban areas, (e) warm-season mean minimum temperature in rural areas, and (f) difference in warm-season mean minimum temperature between urban and rural areas (urban minus rural). Filled circles represent individual urban and rural areas, with circle sizes scaled to urban population.

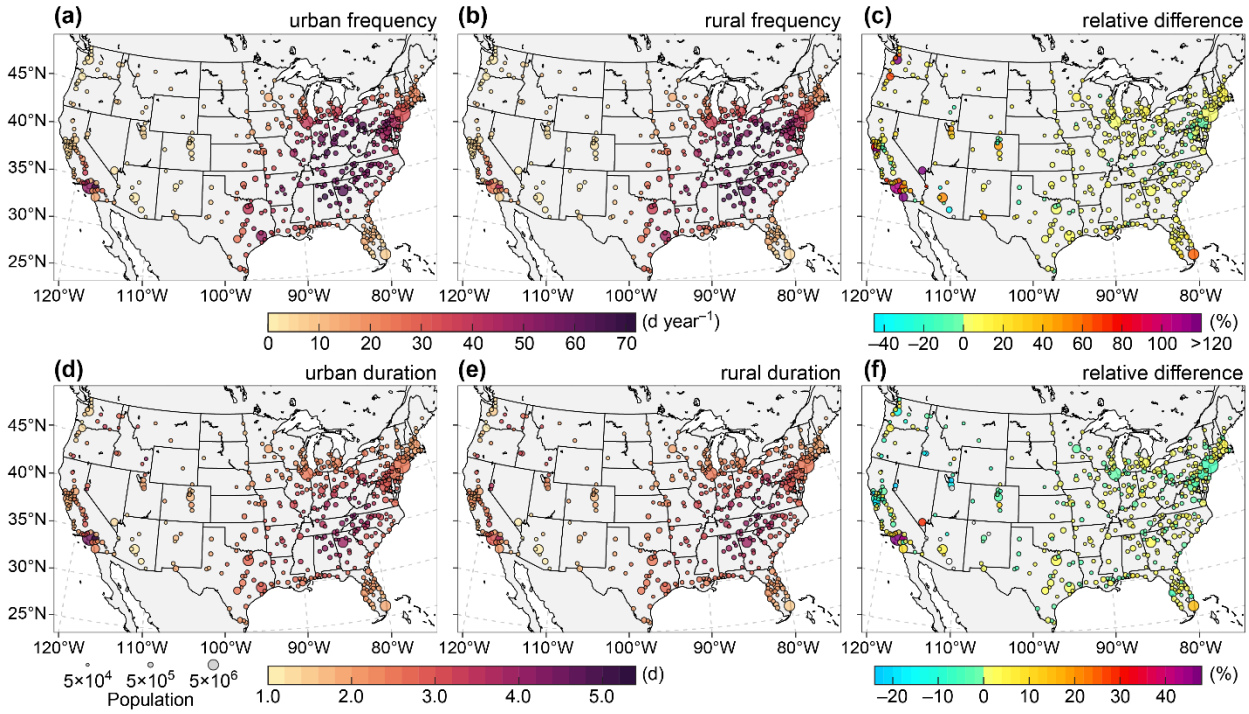


Figure A5. Frequency and duration of $PM_{2.5}$ pollution episodes in urban and surrounding rural areas during 2000–2016: (a) frequency in urban areas, (b) frequency in rural areas, (c) relative difference in frequency between urban and rural areas (urban minus rural), (d) duration in urban areas, (e) duration in rural areas, and (f) relative difference in duration between urban and rural areas (urban minus rural). Filled circles represent individual urban and rural areas, with circle sizes scaled to urban population. White circles in (c) and (f) indicate no urban–rural differences.

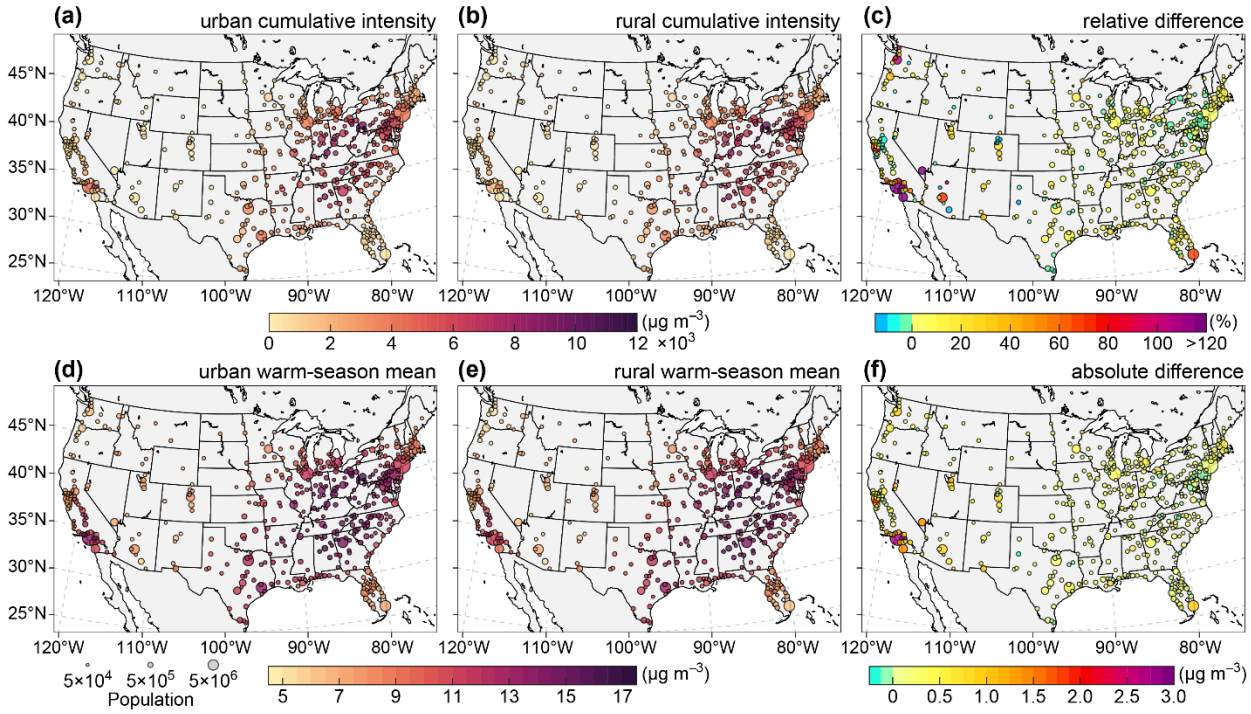


Figure A6. Cumulative intensity of $PM_{2.5}$ pollution episodes and warm-season mean $PM_{2.5}$ concentration in urban and surrounding rural areas during 2000–2016: (a) cumulative $PM_{2.5}$ pollution intensity in urban areas, (b) cumulative $PM_{2.5}$ pollution intensity in rural areas, (c) relative difference in cumulative $PM_{2.5}$ pollution intensity between urban and rural areas (urban minus rural), (d) warm-season mean $PM_{2.5}$ concentration in urban areas, (e) warm-season mean $PM_{2.5}$ concentration in rural areas, and (f) difference in warm-season mean $PM_{2.5}$ concentration between urban and rural areas (urban minus rural). Filled circles represent individual urban and rural areas, with circle sizes scaled to urban population.

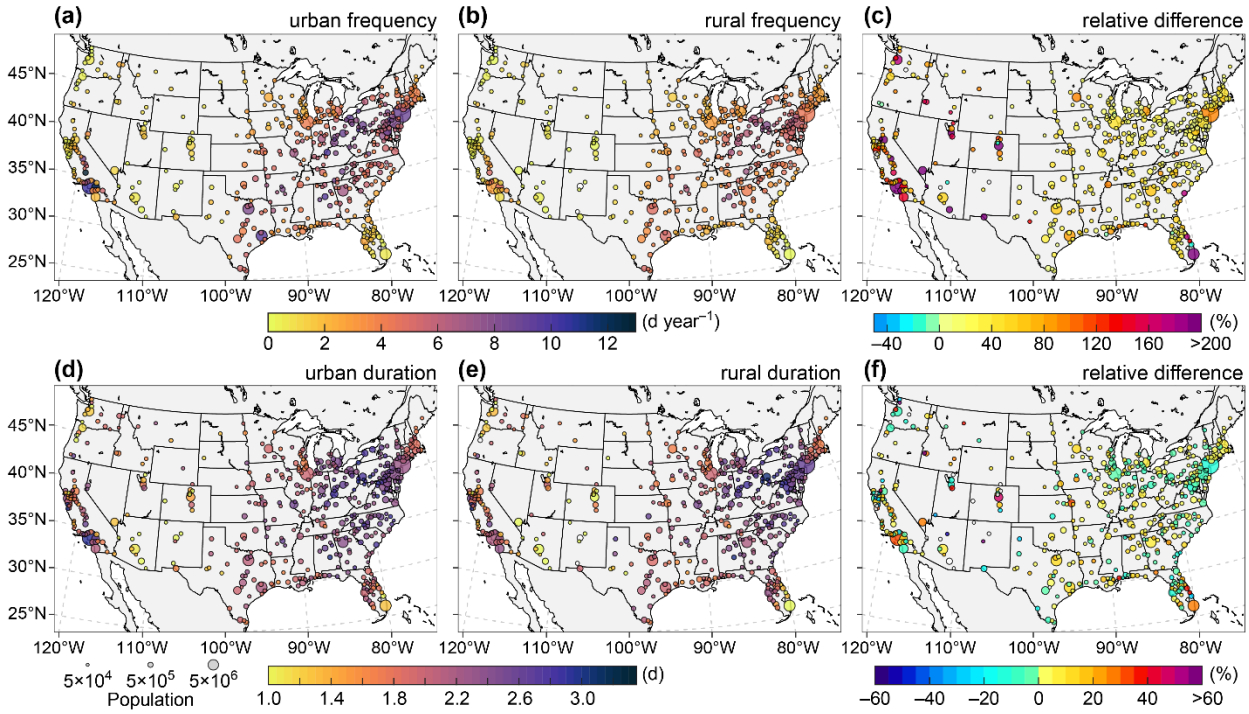


Figure A7. Frequency and duration of compound heat and $PM_{2.5}$ pollution episodes in urban and surrounding rural areas during 2000–2016: (a) frequency in urban areas, (b) frequency in rural areas, (c) relative difference in frequency between urban and rural areas (urban minus rural), (d) duration in urban areas, (e) duration in rural areas, and (f) relative difference in duration between urban and rural areas (urban minus rural). Filled circles represent individual urban and rural areas, with circle sizes scaled to urban population. White circles indicate zero values in urban and/or rural areas in (a), (b), (d), and (e) and no urban–rural differences in (c) and (f).

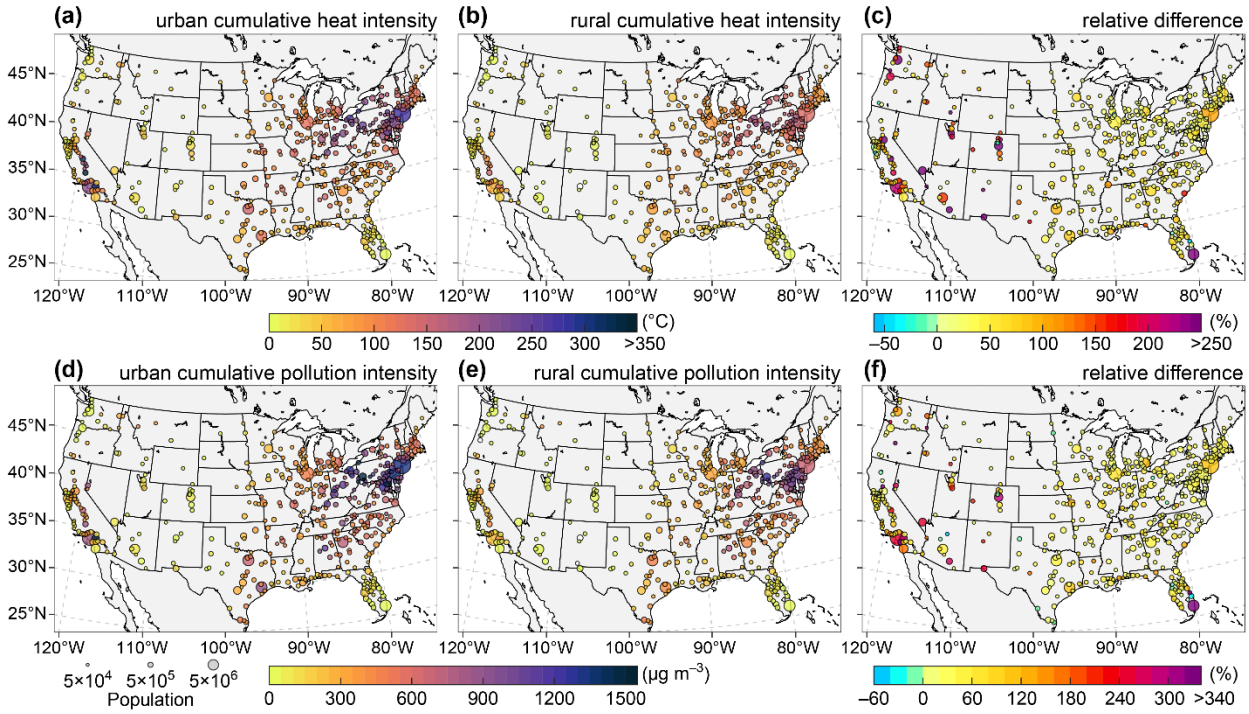


Figure A8. Cumulative intensity of compound heat and $PM_{2.5}$ pollution episodes in urban and surrounding rural areas during 2000–2016: (a) cumulative heat intensity in urban areas, (b) cumulative heat intensity in rural areas, (c) relative difference in cumulative heat intensity between urban and rural areas (urban minus rural), (d) cumulative $PM_{2.5}$ pollution intensity in urban area, (e) cumulative $PM_{2.5}$ pollution intensity in rural area, and (f) relative difference in cumulative $PM_{2.5}$ pollution intensity between urban and rural areas (urban minus rural). Filled circles represent individual urban and rural areas, with circle sizes scaled to urban population. White circles indicate zero values in urban and/or rural areas in (a), (b), (d), and (e).

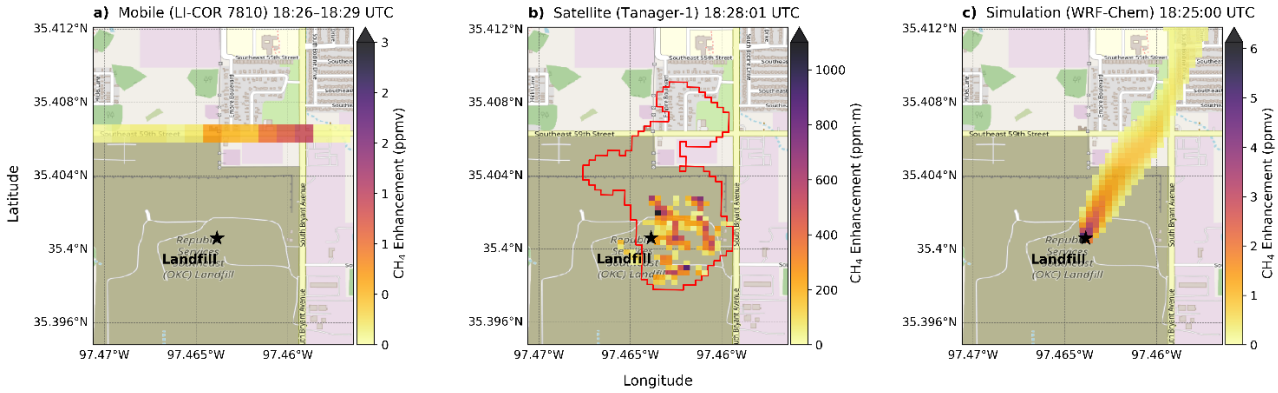


Figure A9. Spatial distribution of CH_4 enhancements around the Oklahoma City landfill site on April 16th, 2026, as captured by (a) LI-COR 7810 mobile measurements from 18:26–18:29 UTC, (b) Tanager-1 satellite overpass at 18:28:01 UTC, and (c) WRF-Chem model simulation at 18:25:00 UTC.

Table A1. Characteristics of heat waves based on minimum temperature in the CONUS and nine climate regions (see Note S1) during 2000–2022: Northeast (NE), Upper Midwest (UM), Ohio Valley (OV), Southeast (SE), Northern Rockies and Plains (NRP), South (SO), Southwest (SW), Northwest (NW), and West (WE).

	CONUS	NE	UM	OV	SE	NRP	SO	SW	NW	WE
Urban frequency (d yr^{-1})	19.18	15.42	9.77	15.65	21.78	12.37	22.75	26.31	19.27	25.31
Rural frequency (d yr^{-1})	14.51	12.84	8.35	12.83	16.94	9.43	18.03	15.84	13.99	16.27
Urban duration (d)	4.75	4.28	4.14	4.37	5.07	4.29	5.15	5.05	4.85	5.27
Rural duration (d)	4.52	4.17	4.10	4.23	4.80	4.13	4.88	4.64	4.55	4.81
Urban cumulative heat intensity (°C)	571.87	556.47	404.92	448.25	417.50	453.52	499.67	817.77	690.02	1052.97
Rural cumulative heat intensity (°C)	415.24	449.73	345.61	358.82	313.19	335.87	380.54	439.43	485.21	670.54

Table A2. Characteristics of $PM_{2.5}$ pollution episodes in the CONUS and nine climate regions during 2000–2022.

	CONUS	NE	UM	OV	SE	NRP	SO	SW	NW	WE
Urban frequency (d yr^{-1})	23.73	26.71	20.09	36.90	28.50	10.28	25.08	5.46	6.73	16.36
Rural frequency (d yr^{-1})	22.70	26.10	19.18	35.87	27.63	9.86	24.04	5.30	6.51	13.62
Urban duration (d)	2.67	2.45	2.16	3.05	2.94	2.48	2.48	2.23	3.11	2.68
Rural duration (d)	2.68	2.44	2.15	3.04	2.92	2.51	2.48	2.32	3.28	2.70
Urban cumulative intensity (μg m^{-3})	3468.94	4415.93	2587.90	5513.92	3735.33	1860.14	2527.03	745.42	3349.14	2703.40
Rural cumulative intensity (μg m^{-3})	3351.27	4339.16	2511.12	5390.03	3609.33	1795.81	2415.62	732.16	3301.84	2427.56

Table A3. Characteristics of compound heat and $PM_{2.5}$ pollution episodes in the CONUS and nine climate regions during 2000–2022.

	CONUS	NE	UM	OV	SE	NRP	SO	SW	NW	WE
Urban frequency (d yr^{-1})	3.48	4.18	2.35	4.47	3.09	1.70	3.74	1.52	2.24	4.44
Rural frequency (d yr^{-1})	2.59	3.39	1.90	3.45	2.30	1.27	2.82	0.98	1.70	2.73
Urban duration (d)	2.20	2.29	2.00	2.25	2.19	2.00	1.97	2.05	2.61	2.41
Rural duration (d)	2.18	2.29	1.98	2.20	2.15	1.93	1.94	2.05	2.67	2.40
Urban cumulative heat intensity (°C)	117.14	161.12	97.44	135.18	65.96	63.80	87.03	57.47	95.46	218.62
Rural cumulative heat intensity (°C)	85.31	128.03	79.13	102.27	47.10	43.50	65.17	34.21	67.70	139.70
Urban cumulative pollution intensity (μg m^{-3})	567.30	811.19	342.40	598.30	390.07	327.79	341.09	189.37	1106.96	915.60
Rural cumulative pollution intensity (μg m^{-3})	429.97	657.01	270.00	429.60	292.31	241.61	261.52	124.10	864.27	664.17

Table A4. Characteristics of heat waves based on minimum temperature in the CONUS and nine climate regions during 2000–2016.

	CONUS	NE	UM	OV	SE	NRP	SO	SW	NW	WE
Urban frequency (d yr^{-1})	16.80	13.86	8.58	14.60	18.18	12.05	20.33	23.63	16.96	21.12
Rural frequency (d yr^{-1})	12.45	11.50	7.21	11.88	13.86	9.12	15.77	13.44	12.12	12.81
Urban duration (d)	4.66	4.26	3.95	4.31	5.01	4.32	5.13	4.90	4.76	4.97
Rural duration (d)	4.43	4.15	3.89	4.17	4.74	4.16	4.86	4.51	4.49	4.57
Urban cumulative heat intensity (°C)	358.05	375.04	255.33	302.39	255.63	318.24	320.57	511.71	432.10	591.95
Rural cumulative heat intensity (°C)	255.41	303.65	214.89	239.85	188.60	231.57	238.58	258.47	299.09	355.19

Table A5. Characteristics of $PM_{2.5}$ pollution episodes in the CONUS and nine climate regions during 2000–2016.

	CONUS	NE	UM	OV	SE	NRP	SO	SW	NW	WE
Urban frequency (d yr^{-1})	29.24	35.02	25.16	48.12	37.43	8.34	31.30	2.62	3.42	14.79
Rural frequency (d yr^{-1})	28.15	34.39	24.22	47.04	36.43	7.85	30.26	2.29	3.10	12.00
Urban duration (d)	2.56	2.49	2.20	3.12	3.01	1.94	2.55	1.59	2.15	2.27
Rural duration (d)	2.55	2.48	2.19	3.10	2.98	1.95	2.53	1.63	2.21	2.23
Urban cumulative intensity (μg m^{-3})	3004.98	4358.12	2464.57	5411.10	3678.08	837.62	2389.47	195.15	508.84	1222.31
Rural cumulative intensity (μg m^{-3})	2902.74	4288.30	2403.56	5302.58	3561.14	780.04	2293.92	176.25	490.56	987.95

Table A6. Characteristics of compound heat and $PM_{2.5}$ pollution episodes in the CONUS and nine climate regions during 2000–2016.

	CONUS	NE	UM	OV	SE	NRP	SO	SW	NW	WE
Urban frequency (d yr^{-1})	3.83	5.45	2.96	5.74	3.94	1.55	4.21	0.59	0.84	2.90
Rural frequency (d yr^{-1})	2.86	4.44	2.41	4.42	2.96	1.17	3.11	0.30	0.53	1.49
Urban duration (d)	2.08	2.35	2.06	2.30	2.28	1.85	1.97	1.29	1.55	1.94
Rural duration (d)	2.02	2.35	2.04	2.24	2.22	1.72	1.93	1.19	1.35	1.86
Urban cumulative heat intensity (°C)	86.77	155.44	89.95	123.37	62.24	42.79	67.11	15.08	23.67	84.99
Rural cumulative heat intensity (°C)	63.28	124.08	73.64	92.82	44.88	29.16	48.69	6.51	13.39	44.41
Urban cumulative pollution intensity (μg m^{-3})	406.03	805.50	332.96	583.29	382.08	145.56	293.71	35.47	85.37	272.64
Rural cumulative pollution intensity (μg m^{-3})	303.78	653.61	264.31	417.61	287.78	115.08	221.06	18.18	50.91	155.46